Acoustic Radiation Force Impulse Imaging of Radiofrequency Ablation Lesions for

Cardiac Ablation Procedures

by

Stephanie Ann Eyerly

Department of Biomedical Engineering
Duke University

Date:_____

Approved:

_____
Patrick D. Wolf, Supervisor

_____
Tristram D. Bahnson

_____
Mark L. Palmeri

_____
Loren W. Nolte

_____
Gregg E. Trahey

Dissertation submitted in partial fulfillment of the requirements for the degree of
Doctor of Philosophy in the Department of Biomedical Engineering
in the Graduate School of Duke University

2013

ABSTRACT

Acoustic Radiation Force Impulse Imaging of Radiofrequency Ablation Lesions for

Cardiac Ablation Procedures

by

Stephanie Ann Eyerly

Department of Biomedical Engineering
Duke University

Date:_____
Approved:

_____
Patrick D. Wolf, Supervisor

_____
Tristram D. Bahnson

_____
Mark L. Palmeri

_____
Loren W. Nolte

_____
Gregg E. Trahey

An abstract of a dissertation submitted in partial fulfillment of the requirements for the degree of Doctor of Philosophy in the Department of Biomedical Engineering
in the Graduate School of Duke University

2013

Abstract

This dissertation investigates the use of intraprocedure acoustic radiation force impulse (ARFI) imaging for visualization of radiofrequency ablation (RFA) lesions during cardiac transcatheter ablation (TCA) procedures. Tens of thousands of TCA procedures are performed annually to treat atrial fibrillation (AF) and other cardiac arrhythmias. Despite the use of sophisticated electroanatomical mapping (EAM) techniques to validate the modification of the electrical substrate, post-procedure arrhythmia recurrence is common due to incomplete lesion delivery and electrical conduction through lesion line discontinuities. The clinical demand for an imaging modality that can visually confirm the presence and completeness of RFA lesion lines motivated this research.

ARFI imaging is an ultrasound-based technique that transmits radiation force impulses to locally displace tissue and uses the tissue deformation response to generate images of relative tissue stiffness. RF-induced heating causes irreversible tissue necrosis and contractile protein denaturation that increases the stiffness of the ablated region. Preliminary *in vitro* and *in vivo* feasibility studies determined RF ablated myocardium appears stiffer in ARFI images.

This thesis describes results for ARFI imaging of RFA lesions for three research milestones: 1) an *in vivo* experimental verification model, 2) a clinically translative animal study, and 3) a preliminary clinical feasibility trial in human patients. In all studies, 2-D ARFI images were acquired in normal sinus rhythm and during diastole to maximize the stiffness contrast between the ablated and unablated myocardium and to minimize the bulk cardiac motion during the acquisition time.

The first *in vivo* experiment confirmed there was a significant decrease in the measured ARFI-induced displacement at ablation sites during and after focal RFA; the displacements in the lesion border zone and the detected lesion area stabilized over the first several minutes post-ablation. The implications of these results for ARFI imaging methods and the clinical relevance of the findings are discussed.

The second and third research chapters of this thesis describe the system integration and implementation of a multi-modality intracardiac ARFI imaging-EAM system for intraprocedure lesion evaluation. EAM was used to guide the 2-D ARFI imaging plane to targeted ablation sites in the canine right atrium (RA); the presence of EAM lesions markers and conduction disturbances in the local activation time (LAT) maps were used to find the sensitivity and specificity of predicting the presence of RFA lesion with ARFI imaging. The contrast and contrast-to-noise ratio between RFA lesion and unablated myocardium were calculated for ARFI and conventional ICE images. The opportunities and potential developments for clinical translation are discussed.

The last research chapter in this thesis describes a feasibility study of intracardiac ARFI imaging of RFA lesions in clinical patients. ARFI images of clinically relevant ablation sites were acquired, and this pilot study determined ARFI-induced displacements in human myocardium decreased at targeted ablation sites after RF-delivery. The challenges and successes of this pilot study are discussed.

This work provides evidence that intraprocedure ARFI imaging is a promising technology for the visualization of RFA lesions during cardiac TCA procedures. The clinical significance of this research is discussed, as well as challenges and considerations for future iterations of this technology aiming for clinical translation.

Contents

List of Tables

List of Figures

List of Abbreviations

2-D	two-dimensional
3-D	three-dimensional
AF	atrial fibrillation
ARFI	acoustic radiation force impulse
AV	atrioventricular
CS	coronary sinus
CCC	cross-correlation coefficient
COM	communication unit (CARTO XP™ EP Navigation System)
CT	computed tomography
CXCC	complex correlation coefficient
DOF	depth of field
DUI	diagnostic user interface
EAM	electroanatomical mapping
ECG	electrocardiogram
EP	electrophysiology
Endo	endocardium
Epi	epicardium
FOV	field of view

ICE	intracardiac echocardiography
IQ	quadrature demodulated
IVC	inferior vena cava
LA	left atrium
LAT	local activation time
LoM	ligament of Marshall
LV	left ventricle
NPV	negative predictive value
NSR	normal sinus rhythm
PPV	positive predictive value
PRF	pulse repetition frequency
PUI	patient interface unit (CARTO XP™ EP Navigation System)
PV	pulmonary veins
PVI	pulmonary vein isolation
RA	right atrium
RF	radiofrequency
RFA	radiofrequency ablation
RFAC	radiofrequency ablation catheter
RFAL	radiofrequency ablation lesion
RFG	radiofrequency generator

ROC receiver operating characteristic

RQ registration qualifier

RV right ventricle

SA sinoatrial

SVC superior vena cava

TA tricuspid annulus

TCA transcatheter ablation

TTC triphenyltetrazolium chloride

List of Symbols

J	current density, units A/m^2
r	radius distance from source, units m
I_o	current source strength, units A
h	heat production per unit volume, units W/m^3
ρ_R	resistivity of tissue, units m/S
σ_t	conductance of tissue, units S/m at C°
T_t	temperature of tissue, units °C/s
t	time, units s
ρ_t	density of tissue, units kg/m^3
c_t	specific heat of tissue, units kJ/kg·°C
Q_m	volumetric heat transfer generated by metabolic processes, units W/m^3
Q_i,	volumetric heat transfer generated by RF current power dissipation, units W/m^3
Q_h	volumetric heat loss from blood profusion, units W/m^3
c_b	specific heat of blood, units kJ/kg·C°
W_b	blood profusion per unit volume, units kg/m^3·s
T_b	temperature of blood in the human body, units C°
Ω	thermal damage, unit-less
ΔE	activation energy, units J/mol

R	ideal gas constant, units J/mol·K
A	frequency factor, units 1/s
F	acoustic radiation force, units kg/s^2·cm^2
W_{absorb}	power absorbed by the tissue at a given spatial location, units W/100·cm^3
c	speed of sound in the tissue, units m/s
α	attenuation, absorption coefficient tissue, units dB/cm/MHz
I	temporal average intensity, units W/cm^2
μ_O	mean, outside lesion
μ_L	mean, inside lesion
σ_O^2	variance, outside lesion
σ_L^2	variance, inside lesion
d_{Final}	final displacement
$d_{Initial}$	initial displacement, (t = 0 s)
τ	stabilization time constant, units 1/s

Acknowledgments

I feel as though I began this project with some of the most arduous tasks already complete, like a jigsaw puzzle where the pieces were already turned right-side up and separated by edge pieces and color groupings. My responsibility became carefully assembling the pieces while having the privilege of witnessing the big picture appear.

To the past and present members of the Nightingale, Trahey, and Wolf labs: I cannot thank you enough for your insight and guidance. Specifically to Stephen Hsu, who had the tedious and frustrating task of teaching me everything I would need to know about ultrasound and computer programming and for essentially holding my hand through the assembly of the puzzle edge. To David Bradway and Doug Dumont, your good humor and willingness to help put the trickiest pieces together was never failing and tremendously appreciated. To Josh Doherty, Peter Hollender, and Stephen Rosenzweig, your sequencing and scanner trouble shooting expertise were instrumental in the completion of the puzzle. To Maryam Jahromi and Young Kim, your enthusiasm, ideas, and readiness to lend a hand were always welcome and helpful.

To members of the BME faculty and staff, specifically Ellen Dixon-Tulloch, Matt Brown, Kathy Barbour, Joyce Franklin, Susan Story-Hill, and Ned Danieley: your patience and instant forgiveness of my blunders kept my research and graduate career on track.

To all the members of my dissertation committee: our discussions and brainstorm sessions have evolved and shaped this research and dissertation into something I can be proud of.

I would like to extend special thanks to Dr. Tristram Bahnson and Dr. Gregg Trahey: your vision and passion for this research was always motivating and gave me a renewed sense of purpose after each meeting and discussion.

To my advisor Dr. Patrick Wolf: I cannot thank you enough for your guidance, patience, and support. Your reminders and encouragement to focus on building the big picture and to "tell the story" of the research has made me a better scientist and engineer.

To the friends who contributed their moral and emotional support inside the department and out: I could not have done it without you. In Durham I have made lifelong friends that have become family.

To my Dad, Mom, and sister Becca: what can I say I have the best family in the world. That goes for Dr. Stuart Webb, too. I feel lucky and am thankful every day that I have you all behind me.

Chapter 1: Introduction

Normal sinus rhythm (NSR) is the intrinsic electrical activation of the healthy human heart that coordinates the mechanical contraction of the four cardiac chambers. In NSR, each heart beat is initiated by the depolarization of the sinoatrial (SA) node, a specialized group of pacemaker cells located in the roof of the right atrium (RA). The SA node depolarization starts a conduction wavefront that spreads uniformly through the RA and along specialized conduction tracts to the atrioventricular (AV) node; the wavefront spreads synchronously into the left atrium (LA) through a specialized conduction tract known as Bachmann's bundle. The AV node delays the excitation wavefront while the atria contract, then proceeds to depolarize the right ventricle (RV) and left ventricle (LV) along the bundle of His and the Purkinje fiber network.

Cardiac arrhythmias are characterized by disturbances in the NSR of the heart; heart rhythm disturbances can cause abnormal heart rates and asynchronous cardiac contraction. Atrial fibrillation (AF) is a cardiac arrhythmia characterized by rapid and dyssynchronous beating of the atria. It is typically caused by multiple re-entering electrical wavefronts wandering chaotically through the atrial tissue. The disorganized atrial conduction pattern causes rapid and irregular ventricular beats, which significantly increase cardiac related morbidity and mortality over time.

AF is the most commonly diagnosed arrhythmia in clinical practice. Over 3 million people in the United States are diagnosed with AF annually, and diagnoses are expected to more than double over the next 40 years.[1-3]

Radiofrequency (RF) transcatheter cardiac ablation (TCA) is a curative treatment for AF.[4, 5] TCA aims to restore the normal rhythm of the heart by directly destroying or electrically isolating abnormally conducting myocardium with lines of radiofrequency ablation (RFA) lesions. To eliminate the arrhythmia RFA lesions must fully ablate the target ablation site and extend the full depth of the myocardium (transmurality), and RFA lesion lines must not contain conductive gaps between lesions that can propagate electrical wavefronts.[6-8]

The biophysics and pathophysiology of RFA lesion formation has been comprehensively studied, but the efficacy of predicting lesion size using delivery parameters such as RF duration, current, and impedance is unreliable because convective cooling at the ablation site and inconsistent electrode-endocardium contact in the beating heart significantly affects lesion formation.[9-16] Without a reliable method to assess lesion presence, size, and transmurality, post-TCA arrhythmia recurrence is common and a significant number of patients (10-30%) require additional ablation procedures.[4, 17-21] Furthermore, electrical reconnection across discontinuous lesion lines has been found in many patients with arrhythmia recurrence.[21] Ideally, direct visualization of the ablated region immediately following RF-delivery would provide

feedback of RFA lesion presence and transmurality as well as lesion line continuity during the initial clinical procedure.

Acoustic radiation force impulse (ARFI) imaging is an ultrasound-based elasticity imaging technique that creates two-dimensional (2-D) images of relative tissue stiffness.[22] ARFI imaging uses ultrasonic radiation force impulses to mechanically displace tissue and conventional ultrasound methods to monitor the tissue response. The axial tissue displacement magnitude (~10 μm) is calculated using correlation based time-delay or phase-shift estimator methods.[23, 24] The magnitude of the measured tissue displacement is inversely proportional to the tissue stiffness, and a 2-D image of the ARFI-induced tissue displacement characterizes relative tissue stiffness.[23, 25, 26]

RF-induced tissue heating causes irreversible denaturation and coagulation of intracellular and contractile proteins; changes in tissue viscoelasticity have been correlated with the thermal denaturation of myocardial proteins.[27-30] Preliminary work has shown ARFI imaging provides accurate visualization of RFA lesions *in vitro* based on the stiffness changes caused by RF ablation.[31, 32]

The central hypothesis of this research was: ARFI imaging can be used for intraprocedure visualization of acute RFA lesions during transcatheter ablation procedures. Evidence to support this hypothesis was investigated in four experimental aims. In the first aim, an experiment was performed to show that *in vivo* ARFI imaging could visualize relative tissue stiffness changes during and immediately after RFA, and

to show that ARFI determined lesion stiffness and detected lesion area were temporally and spatially stable over an acute monitoring period. The second aim addressed the problem of finding lesions in the beating heart using 2-D intracardiac ARFI imaging, which has a limited frame rate (< 1 Hz when diastolic-gated) and narrow field of view (FOV). An experiment was conducted to test the accuracy of identifying RFA lesion sites with an integrated ARFI imaging-electroanatomical mapping system. The third aim was used to verify the presence of conduction disturbances at RFA lesion sites identified with ARFI imaging during TCA. This experiment sought to confirm that ARFI imaging determined lesion assessment was consistent with EAM local activation time (LAT) mapping, which is the clinical gold-standard used to determine the presence of lesions. In the fourth aim, ARFI images were used to show local myocardial stiffness changes at targeted RF ablation sites in human patients. These studies were the 'first in human' experiments to demonstrate these changes. The discoveries and challenges encountered when translating this technology to pre-clinical and clinical models are addressed from a physiological, imaging implementation, and procedural method standpoint.

This thesis is organized as follows: chapter 2 provides background information about the mechanism and treatment of AF, including information about TCA and the biophysics and pathophysiology of RFA. The fundamental concepts behind ARFI imaging are also described in this chapter. Chapter 3 presents an experimental method

for ARFI imaging of RFA-induced myocardial stiffness changes during lesion formation and the acute stability of the measured ARFI-induced displacements in living myocardium. Chapter 4 describes the integration and testing of an intracardiac ARFI imaging-EAM system, as well as the accuracy of evaluating RFA lesions with this multi-modality system during TCA in an animal model. In chapter 5, the integrated ARFI imaging-EAM system was used to evaluate the accuracy of identifying electrical conduction disturbances in canine atria with intraprocedure ARFI imaging of RFA lesions. Chapter 6 presents and describes preliminary intracardiac ARFI images of clinically targeted RFA ablation sites in a pilot group of clinical ablation patients. Chapter 7 presents the final conclusions and clinical implications of this thesis and discusses future directions for this research.

Chapter 2: Background

2.1 Management and Treatment of Atrial Fibrillation

2.1.1 Mechanism and Prevalence of Atrial Fibrillation

Atrial fibrillation (AF) is characterized by rapid (>350 beats per minute) and irregular atrial conduction. An important component of AF initiation and persistence is functional re-entry involving multiple wavelets.[4, 33] Conduction re-entry occurs when a propagating wavelet re-excites an area that had previously been activated by another present wavelet, creating a sustained conduction rotor.[33] Two types of re-entry initiation mechanisms can cause AF: 1) focal electrical triggers, typically from the muscle tissue surrounding and adjacent to the pulmonary veins (PV) or 2) an atrial substrate susceptible to the development of conduction re-entry rotors.[4, 34-37]

For case 1, an electrical depolarization not initiated by the sinus node (ectopic beat) activates the atrium before the normal sinus beat. A re-entry rotor can occur when this "early" wavefront encounters partially or completely refractory myocardium.[4, 34] Cells capable of "abnormal automaticity" have been discovered in the myocardial tissue around the PV in the left atrium (LA), and spontaneous firing of these abnormal cells produce focal triggers that can initiate AF.[4, 38-41] Other potential AF foci can be found at

multiple sites in the atria, including the tissue at the Ligament of Marshall (LoM) and along the posterior left atrium (LA).[4, 42]

In case 2, the reentrant circuit is caused by the presence of two distinct conduction pathways in the myocardium: a path of normal propagation and a second path of "slow" conduction often caused by structural (scar or fibrosis) or functional block in the atrial substrate.[36] Conduction re-entry occurs when impulses traversing the area of slow conduction take long enough to propagate that the myocardium of the normal pathway has recovered; the slow activation wavefront can then re-enter previously the excited myocardium creating a conduction rotor.[4, 34-36, 43, 44]

AF is primarily proliferated and sustained by the following mechanisms: 1) rapid activation of the atrium due to functional re-entry that produces heterogeneous conduction delays and independent re-entry wavelets in other regions of the atrial and 2) chronic rapid atrial activation that causes alterations of the atrial refractory periods due to changes in the cellular excitability via calcium overload and transcriptional regulation. [4, 34, 35, 45, 46]

AF affects approximately 1% of the general population and increases to 8-10% in individuals over 80 years old.[1] Diagnoses of AF are increasing annually, and more than 3 million people in the United States are expected to be diagnosed in the next year alone.[1-3] Patients with AF often see decreased quality of life and may experience symptoms such as severe shortness of breath, chest pain, fainting, weakness, and/or

heart palpitations.[47] Patients with a history of AF also have an increased risk of heart failure and stroke.[42, 48, 49]

2.1.2 Treatment of Atrial Fibrillation

The first line therapy for AF is rhythm management with pharmaceuticals.[4] Unfortunately, a high number of patients (approximately 43%) see no positive response to initial drug therapy.[4, 50, 51] Anti-arrhythmic drugs may also become less effective over time and can cause harmful side effects.[50]

An alternative to drug related treatment of AF is catheter-based surgical intervention, or transcatheter cardiac ablation (TCA). TCA uses an intracardiac catheter-electrode to create focal or continuous lines of transmural lesions to 1) directly ablate abnormally automatic tissue, 2) electrically isolate tissue with abnormal automaticity, or 3) modify potential re-entry circuits by ablating areas of slow conduction. The successful isolation or elimination of these areas restores NSR in many patients. Approximately one-third of AF patients are candidates for TCA and tens of thousands of procedures are performed each year.[4, 18, 52]

As mentioned previously, the PV muscle sleeve and surrounding myocardium are frequent locations of arrhythmia genesis; therefore, the most common TCA technique for treating AF is LA pulmonary vein isolation (PVI). Circumferential PVI techniques aim to completely encircle and electrically isolate the PV with continuous lesion lines to prevent ectopic beats from conducting into the atria.[4, 38, 53, 54] Segmental

PVI is another approach where discrete electrical connections between the PV muscle and atrium are directly targeted to electrically isolate the PV without a complete circumferential ablation.[55] For patients with advanced AF or AF triggering mechanisms not associated with the PV, additional focal ablation is done at other sites thought to participate in the genesis of the AF. Arrhythmogenic substrate is found using local atrial electrograms (EG), and transseptal puncture (TSP) techniques are used to introduce the ablation and EG sensing catheters into the LA.[4, 41, 56]

The published success rates for TCA are typically between 60-90% for both paroxysmal (intermittent) and persistent AF; treatment is often less successful for patients with persistent AF or that show evidence of a diffuse atrial myopathy (measurable deterioration of the muscle tissue and function) than for patients with paroxysmal AF or no evidence of atrial myopathy.[4, 17, 57] Incomplete ablation (gaps in isolation lines, non-transmural lesions) with electrical reconnection or failure to target critical triggers or drivers of AF is the primary cause of the limited treatment success rate.[4, 21] Recurrence of the arrhythmia after unsuccessful procedures requires additional TCA procedures.[4, 17-21]

Overall, TCA procedures are effective, minimally invasive, and have low morbidity and mortality rates, but often require multiple procedures to stop the arrhythmia.[4, 52]

2.2 Radiofrequency Ablation

2.2.1 Biophysics of Radiofrequency Ablation

RF-induced tissue heating causes tissue thermocoagulation necrosis and is produced by applying an alternating current between the catheter tip electrode and a dispersive ground electrode adhered to the patient's skin.[43, 58-60] As the RF current passes through the resistive myocardium, heat is generated in the region surrounding the electrode where the current density is the highest. This local heating creates a permanent lesion of myocyte necrosis.

Assuming the electrode tip can be modeled as a spherical point source, the current density at the electrode tip can be described using a quasi-static approach: the current density (J, units A/m^2) a distance of radius r from the source is equal to the total current source strength I_o (units A) divided by the spherical surface area ($4\pi r^2$, units m^2). This relationship is presented in equation 1. The resistive heating of tissue from applied currents can be described with Joule's first law of heating, which states the heat production per unit volume (h, units W/m^3) is proportional to the current density squared times the tissue resistivity (ρ_R, units m/S; reciprocal of tissue conductance, σ_t = 0.50 S/m at 37C°). This relationship is shown in equation 2.

$$J = \frac{I_o}{4\pi r^2} \qquad (1)$$

$$h \propto \frac{\rho_R {I_o}^2}{16\pi^2 r^4} \qquad (2)$$

This relationship shows the direct resistive heating decreases significantly over a short distance (proportional to $1/r^4$). Therefore, only the ~2 mm of tissue nearest the electrode tip experiences direct heating, and larger lesion formation is the result of passive thermal conduction. RF-induced hyperthermia in the passively heated region of the lesion is governed by the bioheat transfer equation (equation 3).[43, 58, 61, 62]

$$\frac{\partial T_t}{\partial t} = \frac{1}{\rho_t c_t}[\nabla \cdot (k_t \nabla T) + Q_m + Q_i + Q_h] \qquad (3)$$

The first heat source term quantifies the heat transfer from passive thermal conduction, where the rate of change in local tissue temperature (units $^{\circ}$C/s) is equal to the heat transfer densities (units W/m^3) of the heat flow sources (RF) divided by the tissue density (units kg/m^3) and specific heat (units kJ/kg·$^{\circ}$C). Terms Q_m, Q_i, and Q_h represent the volumetric heat transfer generated by cellular metabolic processes, the RF current power dissipation, and the heat loss from blood profusion, respectively. Metabolic heat generation is considered negligible (Q_m = 0) compared to the electrical heating. Direct heating of the tissue due to current power dissipation is also considered negligible (Q_i = 0) because the tissue heating more than ~2 mm from the source is primarily due to passive heat conduction.[43, 63, 64] Heat losses from blood profusion (Q_h) can be quantified using equation 4 where c_b is the specific heat of the blood (units kJ/kg·C$^{\circ}$), W_b is blood profusion per unit volume (units kg/m^3·s), and T_b is the blood temperature in the human

body (C°).[59] The thermo-material constants for cardiac tissue and blood are assumed to be uniform and are presented in tables 1 and 2.[59, 61, 62, 65, 66]

$$Q_h = c_b W_b (T_b - T) \qquad (4)$$

Table 1: Thermal-material properties of cardiac tissue.

Material Property	Symbol	Value	Units
Density	ρ_t	1.06×10^{-3}	kg/m^3
Specific heat	c_t	3.7	kJ/kg·°C
Thermal Conductivity	k_t	0.59	W/m·°C
Conductance	σ_t	0.50	S/m at 37C°

Table 2: Thermal-profusion properties of blood.

Property	Symbol	Value	Units
Blood profusion	W_b	5	$kg/m^3 \cdot s$
Specific heat	c_b	3.6	kJ/kg·°C
Temperature	T_b	37	°C

While mathematical models can provide a basic understanding of the biophysics of RFA lesions formation, many variable factors such as catheter-tissue contact and convective flow at the endocardial surface also significantly affect lesion formation.[10, 12, 13, 67, 68]

2.2.2 Physiology of Radiofrequency Ablation Lesions

When myocardium is heated to temperatures greater than 48°C tissue desiccation and cellular protein denaturation and thermocoagulation occurs, resulting in the

eradication of local electrical conduction and mechanical contraction.[69, 70] The duration of the hyperthermia also affects the extent of myocyte necrosis. The amount of thermal damage incurred by myocytes as a function of temperature and time can be quantified by the time integral of the Arrhenius relationship (equation 5). In this relationship, Ω is a unitless quantifier of cellular thermal damage and is a function of temperature (T, °K), time (t, seconds), and the ideal gas constant (R = 8.315 J/mol·K), as well as material properties for cardiac tissue including the activation energy for irreversible damage (ΔE = 5.87x10^5 J/mol) and a kinetics frequency factor that accounts for morphological changes in the extracellular connective tissue causes by the thermal coagulation of the proteins (A = 2.39x10^{92} s^{-1}).[58, 61, 71]

$$\Omega = A \int_0^t e^{-\Delta E/RT} dt \qquad (5)$$

Irreversible injury to both myocyte organelles and contractile proteins occurs when Ω is greater than 1.[58, 71] At this critical value the survival probability of a single myocyte is 63%, or for a cellular volume where 63% of cells have become necrotic.[64, 71]

Changes in viscoelasticity have been correlated with the degree of protein coagulation during tissue heating, and the ablated region becomes stiffer as the extracellular (collagen and elastin fibrils) and contractile (actin and myosin in myofilaments) proteins irreversibly denature.[27, 28, 30, 72, 73] Irreversible loss of

electrophysiological function is seen in the directly heated lesion core and the passively heated zone of complete thermocoagulation (figure 1).

The myocardium surrounding the pathological lesion can be temporarily affected by the diffusive hyperthermia immediately following ablation.[69, 74, 75] In this region the effects of tissue heating are reversible and insufficient for complete electrical block ($\Omega \leq 0.5$). This "border" zone is characterized by reversibly injured or "stunned" myocytes that suffer a temporary loss of cellular excitability and immune-fluid infiltration (edema).[69, 74-76] Regions of viable myocytes without cellular excitability (less negative resting membrane potential, decrease in the maximum rate of potential change and action potential duration) have been reported to occur within 2 mm of the lesion edge.[75] These effects are transient (~30 to 60-min) and compromise the accuracy of electrophysiology (EP) recordings immediately post ablation.[74, 77, 78] Unrelated to the loss of conductivity, the injured myocytes in the border zone instigate an immune response that causes water and proteins to leak into in to the interstitial space through gaps in the endothelial cells linings of proximal vessels.[76] Magnetic resonance imaging (MRI) has shown edema fluid swelling at the RFA site stabilizes over the first 10-12 min post-ablation and not all edematous areas become chronic scar.[79-81] Histological analysis and cellular damage markers confirm edema is present for several days post procedure.[70, 76, 82] Local edema subsides around 4 weeks post ablation, and permanent fibrotic scar is

complete formed several months after the initial ablation.[70, 76] Figure 2 is a comprehensive timeline of the physiology of lesion RFA lesion development.

Major complications can be caused by excessive RF-delivery during TCA and are reported in approximately 6% of RFA treated patients.[4, 83, 84] For example, if the tissue is excessively heated (>100°C) fluid evaporation can cause an interstitial pressure buildup that results in a steam "pop or rupturing of the myocardium. Other serious morbidities caused by excessive RF-delivery include atrial esophageal fistulas, pulmonary vein stenosis, complete AV nodal block, and excessive damage to collateral tissue or coronary vessels.[83, 85, 86]

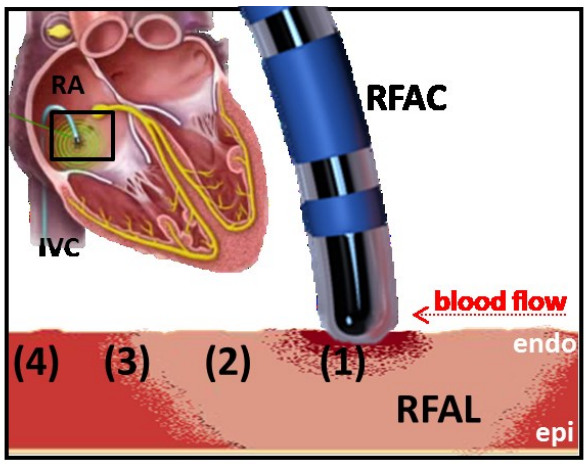

Figure 1: Anatomy of a radiofrequency ablation lesion (RFAL). The radiofrequency ablation catheter (RFAC) is introduced to the right atrium (RA) through the inferior vena cava (IVC). The electrode tip is brought in contact with the endocardial (endo) surface. As the RFAL forms, there are three distinct ablation zones: (1) thermocoagulated core caused by direct resistive heating, (2) irreversibly ablated zone caused by passive thermal heating, and (3) reversibly injured myocytes in hyperthermic "border zone" (~2 mm). Myocardium more than 8 mm from the edge of the lesion (4) is unaffected by the RFA. Adapted from: http://www.hrsonline.org/Patient-Resources/Treatment/Catheter-Ablation#axzz2cvB7gaUy

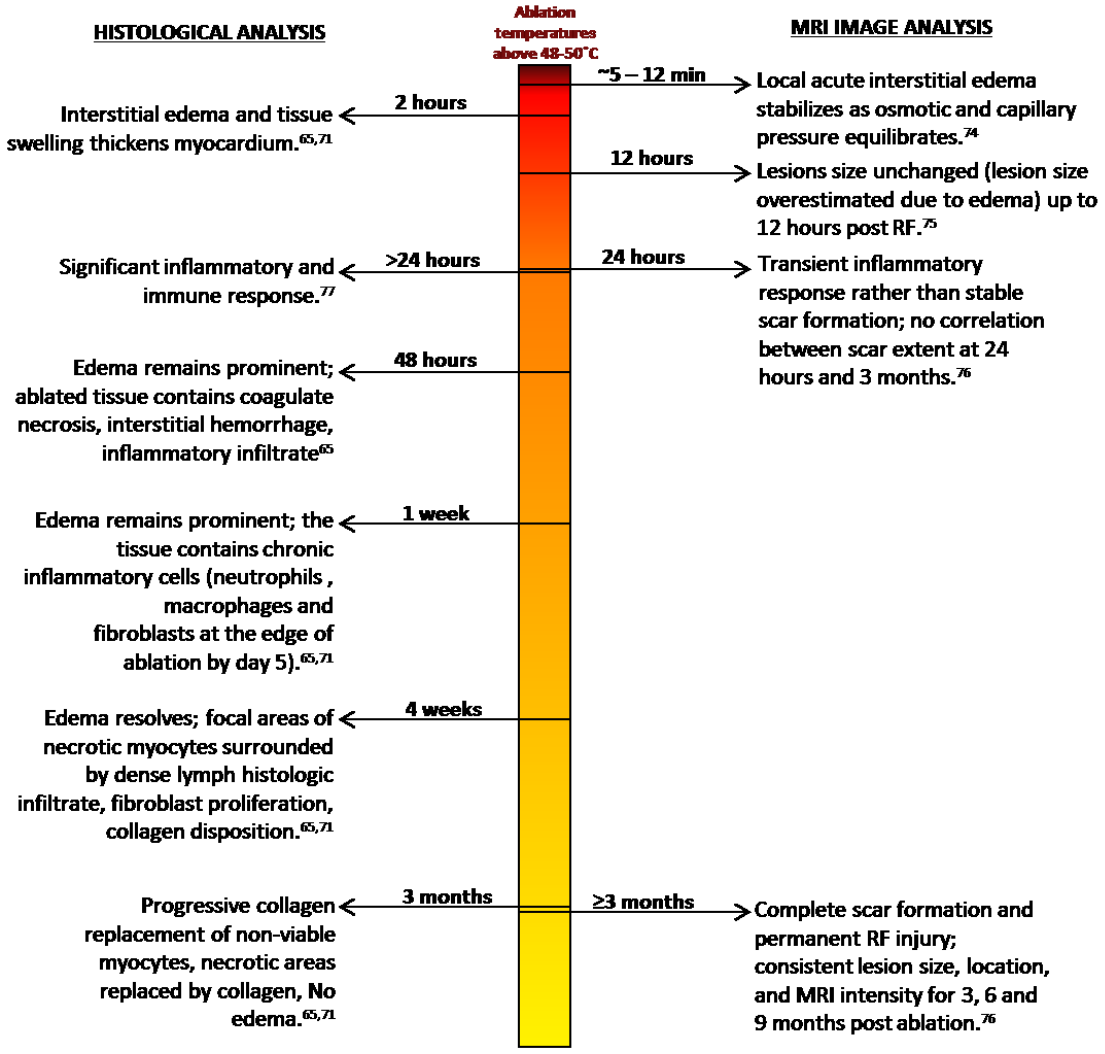

Figure 2: Timeline of edema and chronic RFA lesions development.

2.3 Imaging and Guidance in Cardiac Ablation Procedures

2.3.1 Fluoroscopy

Fluoroscopy is a continuous X-ray imaging technique used to visualize catheter position and orientation in the body with high contrast.[41] Unfortunately, fluoroscopy has poor contrast visualization of soft tissues and cannot provide visualization of the cardiac anatomy or RFA lesions.[87, 88] Fluoroscopy also exposes the patient and medical personnel to ionizing radiation and should be used sparingly.

2.3.2 Intracardiac Echocardiography (ICE)

Intracardiac echocardiography (ICE), or catheter-based ultrasound, is performed with an 8 or 10 French catheter ultrasound probe and provides real-time visualization of the cardiac anatomy and function from within the cardiac chambers.[89-92]

ICE is an indispensable tool for guiding safe and accurate transseptal punctures for LA access during PVI procedures; real-time ICE imaging locates the fossa ovalis in the atrial septum and monitors the transseptal needle puncture and sheath introduction across the septum to the LA.[56, 89, 92, 93] The sheath is then used to feed procedural catheters (ablation and sensing) to the left side of the heart to perform the PVI. The ICE catheter is also frequently introduced to the LA using a "sheathless" or double transseptal puncture.[93, 94] ICE is also used to guide catheter placement and visually confirm RFA catheter-tissue contact for effective RF-delivery.

The real-time visualization and monitoring of potential procedural complications, such as pericardial effusions due to cardiac perforation, thromboembolism formation, atrioesophageal fistulas, or lesion steam pops is also done with ICE.[41, 89]

While ICE serves a variety of important roles in complex ablation procedures, the acoustic contrast between ablated and unablated tissue is insufficient for lesion characterization.[95, 96]

2.3.3 Electroanatomical Mapping Systems

EAM systems, such as the CARTO systems (CARTO XP™ and CARTO 3™; Biosense Webster; Diamond Bar, CA), are the current clinical standard of practice for guiding RFA lesion placement during TCA. EAM systems allow 1) tracking of procedural catheter tips in the heart without fluoroscopy, 2) construction of three-dimensional (3-D) geometric cartoons of the cardiac chamber anatomy, 3) tagging of important procedure locations such as RFA sites, and 4) mapping of local electrical information onto the 3-D geometries for large scale understanding of the arrhythmia substrate and the post RFA chamber conduction.[4, 41, 69, 97]

The CARTO systems use magnetic tracking to triangulate the 3-D positions of specialized mapping-ablation (NaviStar™; Biosense Webster, Inc., Diamond Bar, CA) and ultrasound (SoundStar™; Biosense Webster, Inc., Diamond Bar, CA) catheter tips in the heart to within 1 mm.[97]

A 3-D cartoon of the cardiac chamber is constructed by maneuvering the mapping catheter to multiple locations along the endocardial walls and plotting the relative tip positions. Important locations, such as RFA delivery positions, are saved and displayed on the 3-D geometry. The mapping catheter electrode-tip also collects local EG and calculates local activation times (LAT) relative to a reference EG or the ECG; the LAT are plotted on the 3-D volume to identify arrhythmogenic pathways and confirm electrical block post ablation. The reference EG is often a separate sensing and pacing catheter that is positioned in the coronary sinus (CS). Additional information about the CARTO XP™ system is provided in appendix A.

Despite these important functions, EAM tracking systems can only indirectly infer RFA treatment from sparse electrical data and cannot provide direct visualization of RFA lesions. The RFA point markers on the 3-D geometry represent RF-delivery locations, but do not characterize lesion size or transmurality.

2.3.4 MRI for Substrate Characterization and RFA Assessment

MRI (primarily T2-weighted and late gadolinium enhanced) is currently being vetted for pre and post-TCA substrate characterization and RFA lesions assessment during TCA.[92, 98-104] MRI has proven to be a gold-standard for fibrosis substrate mapping and provides a non-invasive method to visualize ablation lesion patterns.[105-107] While a promising pre and post-procedure substrate and lesion assessment tool, MRI has major limitations when translating to an intraprocedure imaging modality, such as the

requirement of non-metallic procedural catheters and lengthy acquisition times. Specialized MRI suites are also expensive to build, equip, and run. In addition, recent studies have shown MRI assessment of atrial RFA lesions has limited accuracy; MRI requires further investigation to prove it has adequate resolution for distinguishing unablated gaps in atrial lesion lines and adequate contrast sensitivity to distinguish transient interstitial edema from tissue necrosis.[102, 104, 108]

2.4 Acoustic Radiation Force Impulse (ARFI) Imaging

Acoustic radiation force impulse (ARFI) imaging is an ultrasound-based imaging technique that was recently developed at Duke University. This section describes the concepts and methods behind the implementation of ARFI imaging as well as preliminary work for imaging of cardiac RFA lesions.

2.4.1 Acoustic Radiation Force

Acoustic radiation force is a body force generated by a transfer of momentum from an acoustic impulse wave into the target medium.[109, 110] At ultrasonic frequencies the acoustic wave propagates as a plane wave and targeted soft tissue medium behaves as an incompressible, linearly viscous fluid.[109, 111, 112] The force magnitude generated by the propagating wave is approximated by the following relationship:

$$F = \frac{W_{absorb}}{c} = \frac{2\alpha I}{c} \qquad (6)$$

F is the acoustic radiation force magnitude (units kg/s^2·cm^2), W_{absorb} is the power absorbed by the tissue at a given spatial location (units W/100·cm^3), and c is the speed of sound in the tissue (approximated as 1540 m/s).[25, 65, 110] The absorbed power is equal to twice the attenuation-absorption coefficient of the tissue ($\alpha \approx 0.55$ dB/cm/MHz) times the temporal average intensity I (units W/cm^2) at the impulse location.[113]

In soft tissue the majority of the energy from the ARFI-excitation or "push" is absorbed at the impulse focal region, and this spatially localized (1-8 mm^3) energy generates a radiation force that deforms the tissue in the direction of the impulse propagation.[22] The magnitude of the deformation is largest at the focal depth and is related to the stiffness of tissue.[114, 115] The acoustic impulse length required to generate detectable axial displacements (on the order of microns, μm) in soft tissue is typically between 0.30 and 1 ms.[116]

2.4.2 ARFI Imaging

ARFI imaging is a novel imaging modality that has been refined into a unique clinical tool over the last two decades.[26, 117] Radiation force elastography methods such as ARFI imaging have been increasingly investigated for the visualization of stiffness changes at RF ablation sites in the liver, kidney, and heart.[29, 31, 32, 95, 96, 118-122]

ARFI images are formed by applying a coordinated sequence of radiation force impulses to soft tissue and temporally and spatially monitoring the resulting axial deformation with conventional ultrasound scan-lines. The magnitude of the tissue

displacement is calculated using delay estimator methods such as normalized cross-correlation or phase-shift autocorrelation.[23, 123, 124] The measured ARFI-induced displacement is inversely proportional to the tissue stiffness and directly proportional to acoustic attenuation.[25, 125-127] 2-D ARFI images are formed by spatially distributing the ARFI excitations across a lateral FOV and assigning a color scale to the measured displacements for visualization of the relative tissue stiffness.

ARFI imaging is currently implemented from software-modified diagnostic ultrasound scanners and uses conventional ultrasound transducers for the generation of the radiation force and the tracking of the tissue response. The use of traditional diagnostic equipment also provides the ability to acquire spatially and temporally co-registered traditional B-mode images.

Due to the assortment of ARFI imaging sequences, ultrasound scanners, and transducers used in this thesis, the specific imaging and sequencing parameters for each experiment are described in the methods section of each chapter.

2.4.2.1 Cardiac Motion and ARFI imaging

The maximum LA wall velocity is approximately 3.2 cm/s in the normal human heart.[128, 129] In elderly patients or in patients diagnosed with a cardiac arrhythmia this velocity could be higher. Motion of this magnitude can overwhelm the ARFI-induced displacement magnitude as well as cause decorrelation of the tracking scan-lines, thereby increasing the bias (mean of the displacement error) and jitter (error of the bias,

or standard deviation of the displacement error) of the displacement estimation.[23, 130] Specialized processing methods are used for cardiac ARFI imaging to separate the displacements generated by the ARFI-excitation from the bulk physiologic motion.[96, 130-132] These motion filtering methods estimate the bulk physiological motion by fitting a quadratic curve to the measured displacement profile at each pixel in the image. The estimated motion function is then subtracted from the measured displacements to recover the ARFI-induced displacement.

Two methods for constructing the motion curve fit are used in the thesis: 1) interpolation of the motion function from the pre-excitation position and a post ARFI-excitation position and 2) extrapolation of the motion function using the pre-excitation baseline motion to approximate the motion profile.[130] Basic motion filtering has been shown to reduce motion artifacts to under 1 μm over the cardiac cycle.[96]

2.4.2.2 Image Quality

In this thesis, image quality is quantified by calculating RFA lesion contrast (C) and contrast-to-noise ratio (CNR). C and CNR are calculated using equations 7 and 8, where μ_O and μ_L are the mean signal inside the lesion and outside the lesion respectively, and σ_O^2 and σ_L^2 are the variances.

$$C = \frac{\mu_O - \mu_L}{\mu_{UA}} \tag{7}$$

$$CNR = \frac{|\mu_O - \mu_L|}{\sqrt{{\sigma_O}^2 + {\sigma_L}^2}} \tag{8}$$

2.4.3 Preliminary Work on ARFI Imaging of RFA Lesions

Several studies investigating the feasibility of cardiac RFA lesion visualization with ARFI imaging have been conducted.[31, 32, 95, 96, 133] This section describes the studies that laid the groundwork for the research presented in this thesis.

2.4.3.1 *In vivo* Feasibility

Preliminary *in vivo* feasibility studies were conducted by Fahey *et al*. in 2005 and Hsu *et al*. in 2007.[95, 96] Fahey *et al.* were the first to observe the localized stiffness change caused by cardiac RFA using ARFI imaging.[95] Hsu *et al.* prepared this technology for potential clinical translation by developing ARFI imaging sequences for an intracardiac ultrasound transducer; in a canine model they observed an increase in tissue stiffness at three endocardial RFA sites, evident by a decrease in the measured ARFI-induced displacement.[96] This work also described the challenges encountered when implementing ARFI imaging from an ICE catheter.[96] It was discovered that the flexible transducer tip experienced a small rebound force from the generation of the ARFI-excitations. It was determined that the radiation force pulses transmit high intensity acoustic waves backwards into the transducer matching layer as well as forward into the tissue. The absorption of this mechanical energy generated a force that bent the flexible imaging catheter in the opposite direction of the ARFI-excitation. This transducer "kick-back" was initially non-linear and tracked in the displacement estimations. They prepared sequences that applied ten "priming pulses" before the 2-D ARFI imaging

sequence so any remaining kick-back motion was linear and could be effectively motion filtered from the ARFI displacement estimations. This priming pulse technique is used in the ICE-based sequences developed for the experiments in this thesis.

It has been shown that diastolic imaging is ideal for ARFI imaging of lesions *in vivo* because the contrast between the stiff RFA lesion and normal tissue decreases when the myocardium stiffens during systole.[95, 96, 133] Also, late diastole is the time of least intrinsic motion during the cardiac cycle and reduces the effects of bulk cardiac motion on the tissue displacement measurements. Figure 3A illustrates the relative stiffness difference between systole and diastole around a ventricular epicardial RFA lesion.[133] The lesion is visible as a semicircular region of relatively low ARFI-induced displacement (dark blue). The ARFI image contrast between the lesion and unablated myocardium (red) is maximal during diastole (figures 3A-1 and 3A-4)

All ARFI images presented in this thesis were ECG-gated to diastole. The challenges associated with non ECG-gated ARFI image acquisitions, for example during AF, was beyond the scope of this thesis, but is briefly discussed in the future work section of chapter 7.

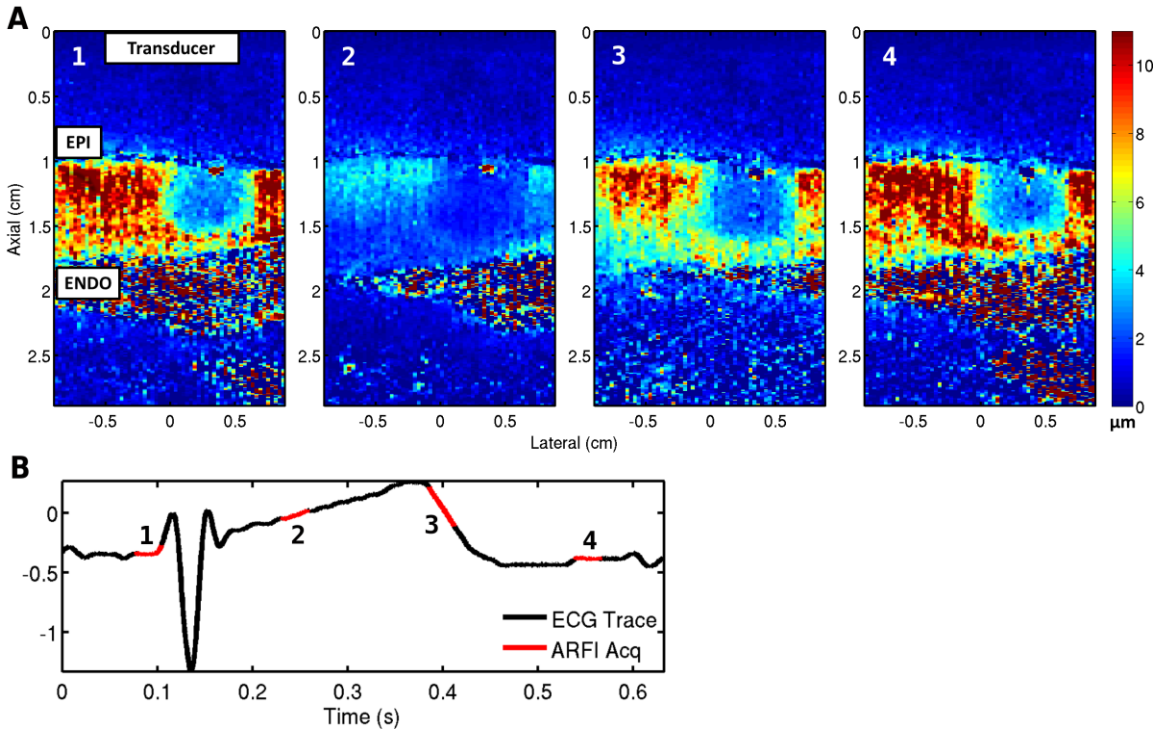

Figure 3: ARFI images of a right ventricular epicardial RFA lesion through the cardiac cycle. A non-irrigated electrode tip ablated the epicardial surface (EPI = epicardium, ENDO = endocardium) for 7 sec at 20 W. A) ARFI images acquired at different times during the cardiac cycle: (1) and (4) during diastole, (2) during systole, and (3) during end-systole. ARFI images were acquired with a linear transthoracic probe vacuum suctioned to the RV epicardium. Color bar units are maximum displacement away from the transducer in microns. Within the lesion the ARFI induced displacement is low (blue) throughout the cycle. The normal myocardium cycles between high displacement (red) during diastole and low displacement (blue) during systole. B) ARFI acquisition times corresponding to the ECG.

2.4.3.2 *In vitro* Lesion Assessment

The accuracy of determining RFA lesions size with ICE-based ARFI imaging was investigated *in vitro* in earlier work.[31] This study determined that lesion dimensions from ARFI and pathology images were statistically similar and within 1-2 mm.

An example lesion from this study is shown in figure 4. The red spectrum of the ARFI-induced displacement color bar represents normal myocardium, while the region of lower induced displacement is represented by the blue-green portion of the color bar. The determined lesion traces correlate will with the RFA lesion pathology.

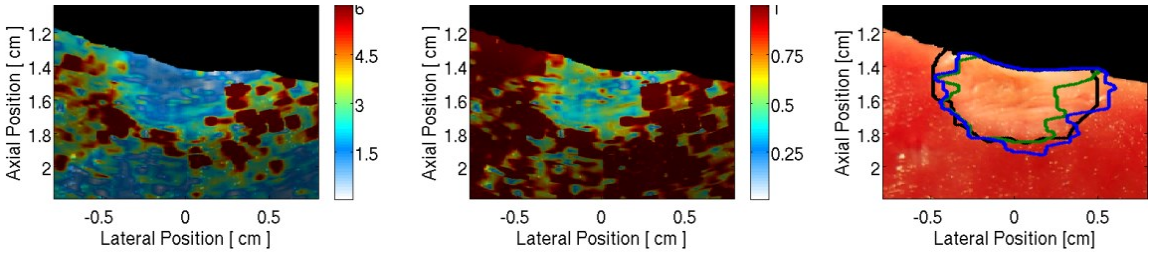

Figure 4: ARFI imaging determined lesion boundaries. The maximum ARFI-induced displacement (left) and depth normalized (center) image were overlaid onto the photograph of the lesion cross-section. The lesion boundary traces were determined by a manual (black) and automatic (blue: optimal, and green: standardized) segmentation of the digital image.

Another experiment demonstrated ARFI imaging can visualize the RFA-induced myocardial stiffness increase during lesion formation *in vitro*. Figure 5 shows the relative stiffness change in the myocardium that occurs during RFA.[32]

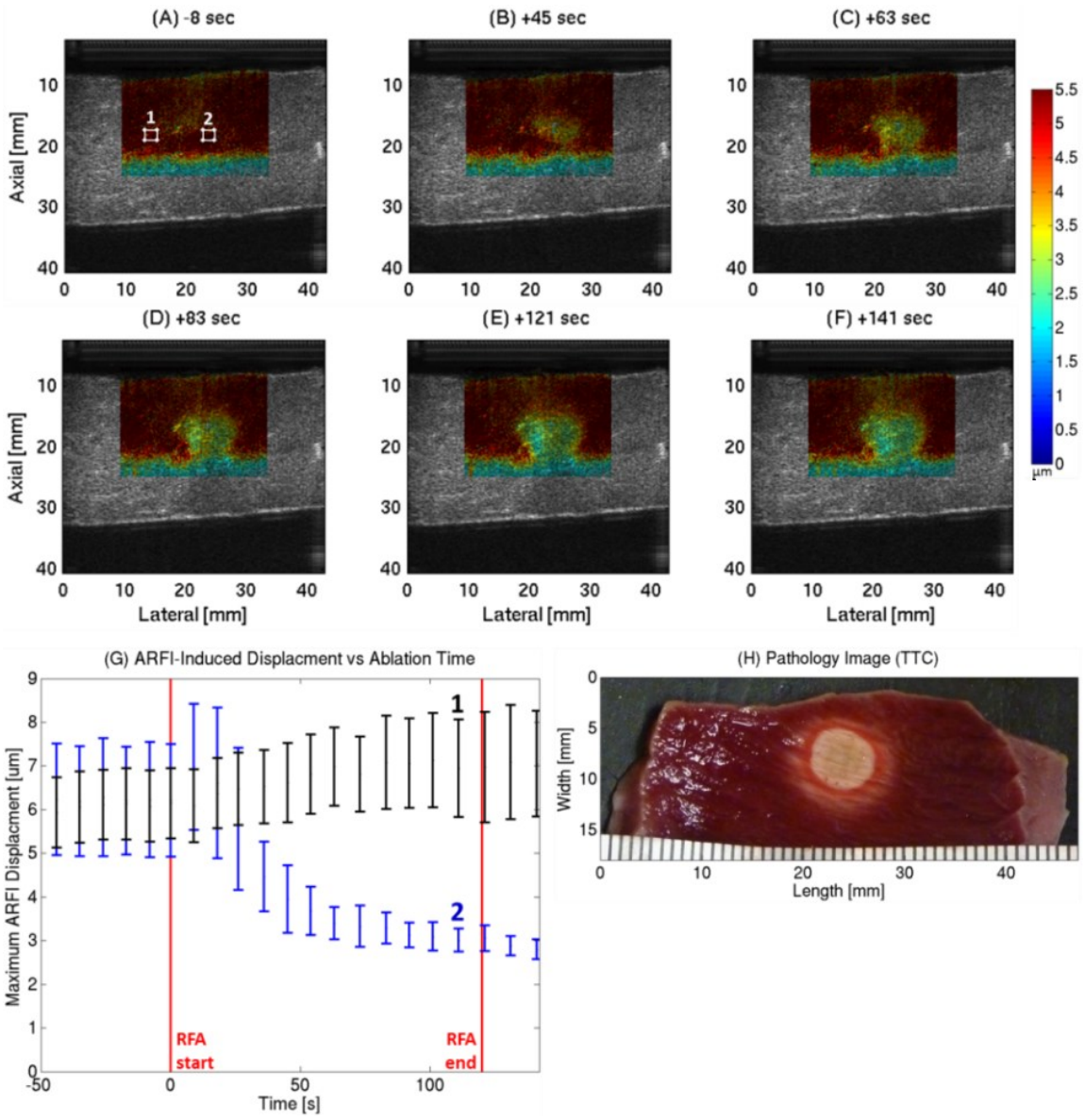

Figure 5: ARFI images acquired during an *in vitro* RFA. (A) The pre-RFA image shows high ARFI-induced displacement throughout the myocardium. During RFA a growing region of increased stiffness appeared (B-D). The plane of the RFA catheter is into the page and the effective depth of field (1.5 cm focus) is between 1.0 and 2.25 cm. (G) The mean and standard deviation of the ARFI displacements measured outside the lesion remained constant during RFA but decreased inside the lesion. (H) The tissue was sliced in the approximate imaging plane and stained with triphenyltetrazolium chloride (TTC) to confirm a lesion was created.

Chapter 3: Temporal-Spatial Monitoring of Acute Cardiac Radiofrequency Ablation Lesions with ARFI imaging *In Vivo*

The work described in this chapter will be submitted for publication in the following manuscript:

Eyerly SA, Dumont DM, Trahey GE, Wolf PD. Temporal-Spatial Monitoring of Acute Cardiac Radiofrequency Ablation Lesions with Acoustic Radiation Force Impulse Imaging In Vivo.

3.1 Introduction

Previous work has shown ARFI imaging can characterize RFA lesions *in vitro*, but RF-delivery in living tissue induces transient physiological processes (see section 2.2.2) that may affect the stiffness at the RFA site. Immediate post ablation lesion monitoring with ARFI imaging and could improve our understanding of acute RFA lesion formation and the stability of the tissue necrosis. This chapter investigates the *in vivo* temporal-spatial stability of acute RFA lesions evaluated with ARFI imaging.

This study utilized a linear array transducer suctioned directly to the cardiac wall to monitor endocardial lesion formation and post ablation lesion stabilization. The aims of this investigation were 1) to evaluate the contrast and stability of the ARFI-induced displacement measurements in regions of interest (ROI) inside the RFA lesion,

in the border zone, and outside the lesion and 2) to characterize any changes in lesion area over a 30 minute monitoring period immediately post ablation.

The chapter is organized as follows: section 3.2 describes the experimental protocol and ARFI imaging methods for repeatable imaging of acute RFA lesions sites. Section 3.3 describes the experimental results, and section 3.4 discusses the implications of these findings for implementation of *in vivo* ARFI imaging and the relevance to clinical translation.

3.2 Methods

3.2.1 Animal Experimental Protocol

The animal experimental protocol described in this study was approved by the Duke University Animal Care and Use Committee and conformed to the Guide for the Care and Use of Laboratory animals.[134]

Six canine subjects were anesthetized (pre-anesthesia: intramuscular acepromazine 0.02-0.05 mg/kg followed by interveinous propofol 4-6 mg/kg; general anesthesia: isoflurane gas 1-5% via inhalation), intubated, ventilated, and maintained metabolically stable. A thoracotomy was performed and the pericardium was opened and sutured to form a cradle, exposing the epicardium of the heart. A VF10-5 linear ultrasound transducer (Siemens Healthcare; Issaquah WA) was put into a vacuum-coupling device and positioned over the right ventricular (RV) epicardium using an adjustable stabilization arm mount. The vacuum-coupling device suctioned directly to

the epicardium to maintain the imaging position. The vacuum apparatus also held the transducer ~1 cm from the heart (imaging through an ultrasonically transparent standoff) to position the imaging focus in the center of the myocardium (figure 6).

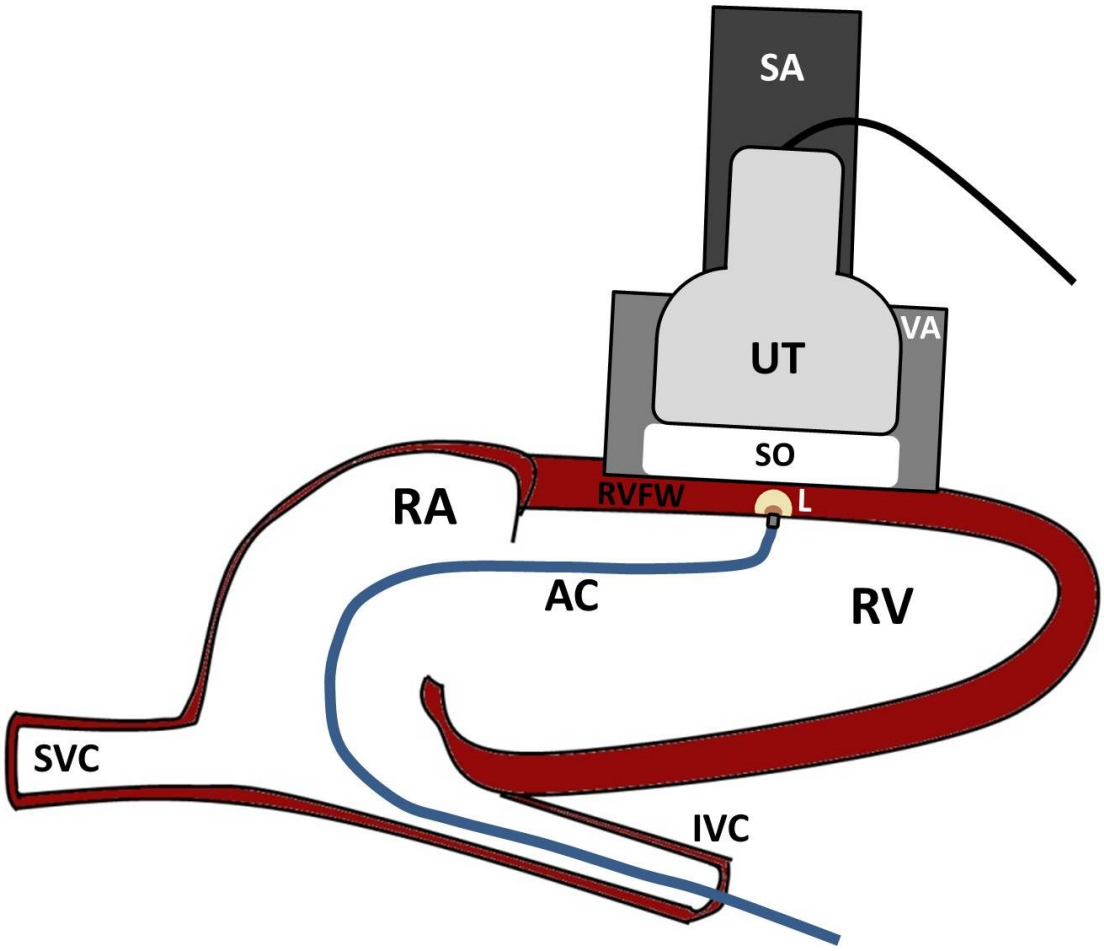

Figure 6: Open chest *in vivo* ARFI imaging experimental setup. The VF10-5 ultrasound transducer (UT) was held by a vacuum-coupling apparatus (VA) and positioned directly onto the right ventricular free wall (RVFW) using an adjustable stabilization arm (SA). The ablation catheter (AC) was introduced to the heart through the inferior vena cava (IVC) and brought in contact with the RVFW endocardium directly under the UT. The RFA lesion (L) formed in the ARFI imaging plane.

ARFI images were acquired before, during, and approximately every 30 to 45 seconds for 30 minutes after a 60 second temperature-controlled (65°C) endocardial ablation with the RFA catheter (7 Fr, Celsius™: Biosense Webster, Diamond Bar, CA) in the ARFI imaging FOV. All ARFI acquisitions were ECG-gated to diastole to maximize the stiffness contrast between the RFA lesion and surrounding myocardium, as well as minimize the cardiac motion during the acquisition.[133] Respiration was held during imaging to minimize the effects of respiratory motion on the image plane position.

At the end of the study, the canine was euthanized and the heart was removed. Each lesion (1-3 per canine) was manually cross-sectioned (~1 mm slices) parallel to the approximate imaging plane used during the procedure. The tissue samples were stained with triphenyltetrazolium (TTC) and photographed.

3.2.2 ARFI Imaging Methods and Image Processing

Co-registered ARFI and B-mode imaging was performed with a hardware and software modified Siemens SONOLINE Antares™ ultrasound scanner and an unmodified 192 element VF10-5 linear ultrasound transducer (Siemens Healthcare; Issaquah, WA). Each ARFI image sequence completed in 110 ms, and the raw data was saved as in-phase and quadrature demodulated (IQ) data by the ultrasound scanner.

All images were formed with a center frequency of 8.0 MHz and an ARFI-excitation frequency of 5.7 MHz. The ARFI images were acquired with a focal depth of 1.6 cm or 2.0 cm. For each acquisition, 36 radiation force impulses (53 μs pulse length)

were delivered at equally spaced locations over a 2.14 cm lateral FOV. At each lateral location, eight ultrasound pulses (~10 kHz tracking pulse reputation frequency, PRF) were transmitted before the ARFI-excitation to determine the initial position of the tissue, and fifteen were transmitted after the excitation to monitor the ARFI-induced tissue deformation. Four-to-one parallel-receive imaging (4:1, four echo lines received for each transmit pulse) was used to increase the line density of the ARFI image.[135] The final ARFI image had a line density of 67 lines per cm. The ARFI imaging parameters are summarized in table 3.

Table 3: ARFI imaging parameters for the VF10-5 linear transducer.

Transducer	Probe	VF10-5
	Elements	192
	Array Type	Linear
	Center Frequency [MHz]	5.71
Scanner	Model (Siemens)	Antares™ (SONOLINE)
	Data Type	IQ
B-mode and ARFI Imaging Parameters	Transmit Frequency [MHz]	5.71
	Tracking Frequency [MHz]	8.00
	Sampling Frequency [MHz]	40
	Focus [cm]	1.6 or 2.0
	F/#	2.4 or 3.0
	Cycles	300
	ARFI-excitation length [μs]	53
	ARFI-excitation lateral locations	36
	Parallel tracking	4:1
	Pre-tracks	8
	Post-tracks	15
	Tracking PRF [kHz]	10

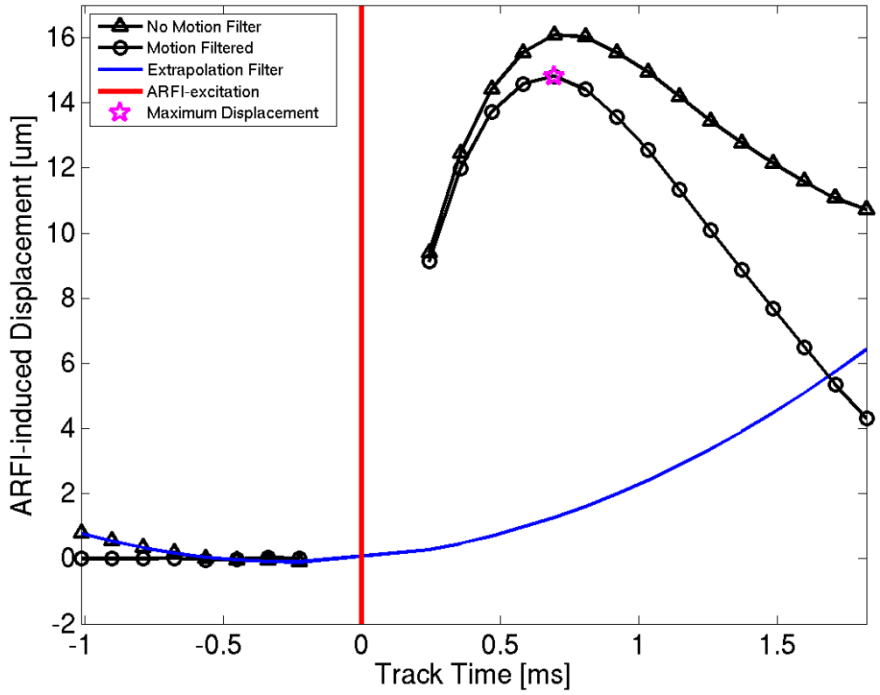

Figure 7: ARFI-induced displacement curve for a single pixel in the myocardium. Eight scan-lines were acquired before the excitation to determine the baseline position. The motion filter function (blue) was extrapolated from the pre-excitation data, and subtracted from the raw displacements (triangles) to calculate the motion filtered displacement profile (circles). Fifteen scan-lines were acquired after the ARFI-excitation to monitor the axial tissue displacement. Total tracking time for a single line was ~2.75 ms. The maximum displacement over the tracking time (magenta star) was the pixel value in the 2-D ARFI image.

The ARFI-induced axial displacement magnitudes were calculated by correlating each post-excitation track-line with the echo from the last reference line using a phase-shift estimation algorithm (Loupas, axial kernel: 1.5λ, wavelength).[23, 124] A quadratic extrapolation motion filter technique was used to minimize the effects of bulk axial motion on the estimated displacements.[24, 136, 137] An example of this process for a single pixel location is presented in figure 7.

The quality of the displacement estimation for each pixel-kernel location was quantified by calculating the magnitude of the complex correlation coefficient (CXCC) calculated during the phase-shift estimation.[117, 138] Pixel locations with low CXCC, such as in the blood, exhibited significant decorrelation of the signals between the tracking lines. Any pixel where the median CXCC through the tracking time was below 0.90 was removed from the final ARFI image. Displacements measured in the blood also had large standard deviations; any pixel with a standard deviation larger than 20 μm was also removed.

3.2.3 Temporal Image Registration and ARFI Image Normalization

The vacuum apparatus and arm mount stabilized the position of the transducer, but the dynamic motion of the heart and lungs inevitably caused small translations of the imaging plane between image acquisitions. A 2-D normalized cross-correlation registration of the B-mode images was performed to compensate for any small axial or lateral translations of the imaging plane through the time-course. The ARFI images were not involved in the registration process.

The image templates for the correlation were automatically chosen as 1 mm above the highest point of the epicardium and 1 mm below the lowest point of the endocardium for all the images in the lesion time-course. The epicardium and endocardium were automatically determined as the edges of the myocardium in the thresholded B-mode image. The applied threshold was the brightness intensity mean in

each image plus 0.8 (epicardium) or 0.45 (endocardium) of the standard deviation. The region containing the myocardium was manually segmented before the thresholding to mask the ablation catheter and far-field cardiac structures. The detected endocardium and epicardium were smoothed using an eight pixel median filter.

Each image was correlated with all the other images from the time-course. The maximum spatial correlation coefficient for the pair was used as a registration qualifier (RQ) to quantify the overall quality of the image registration.

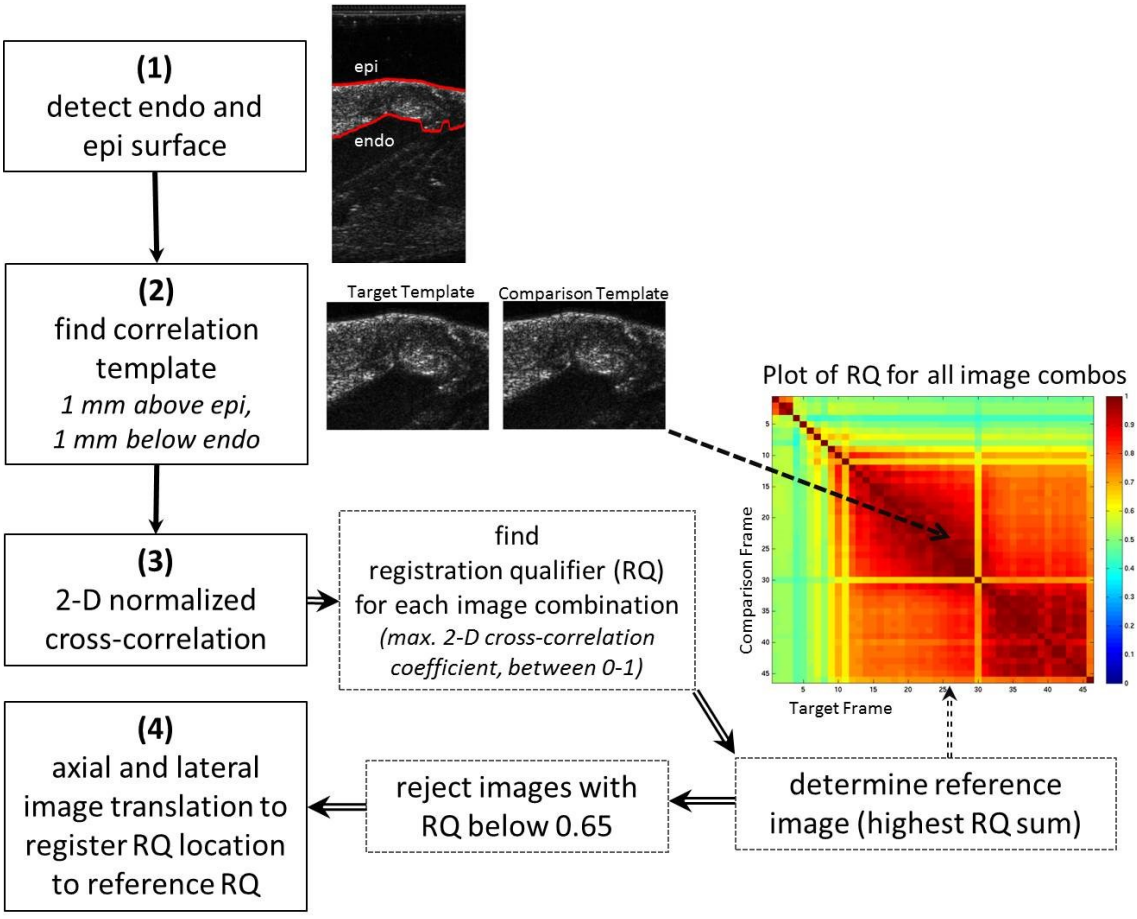

Figure 8: Block diagram of B-mode image spatial registration.

The post ablation image with the highest RQ sum for all image combinations was used as the reference image for the spatial registration (axial and lateral translation) of the other images. Individual images with a RQ lower than 0.65 were discarded from the statistical analysis. The registration process is summarized as a block diagram in figure 8. Occasionally air bubbles would become trapped between the transducer and myocardium; images where an air bubble created noisy artifacts in the myocardium were also removed from analysis.

The maximum ARFI-induced displacements were normalized to minimize the effects of the focal depth of field (DOF) and energy attenuation.[31, 139] The pre-ablation image with the highest RQ sum for all correlation combinations was used for the ARFI image normalization. In this image, the maximum measured ARFI-induced displacements in the myocardium (0.5 mm below the epicardial surface and 0.5 mm above the endocardial surface) were laterally averaged across FOV and plotted as a function of axial depth. A quadratic curve was fit to this plot and the resulting function was used to normalize each displacement pixel as a function of depth.

3.2.4 Contrast Analysis and Temporal Stability of Normalized Displacements

For all post ablation images, the RFA lesion was automatically detected by thresholding (mean normalized displacement in the myocardium minus one third of the standard deviation) the normalized ARFI-induced displacements. A composite lesion for each lesion group was defined by combining pixel locations that were classified as

lesion in at least 75% of the post ablation images. Three 1x1 mm regions of interest (ROI) were automatically defined for each lesion group using the composite lesion: 1) the lesion interior (lesion centroid), 2) the lesion border zone (lesion edge at axial depth of centroid), and 3) 3 mm outside lesion border zone (at axial depth of centroid). A repeated measures analysis of variance (ANOVA) was performed to test the significance of the variance between individual lesion and the effects of RFA (inside vs. outside) on the mean normalized displacement in the ROI.

The means of the ROI in each lesion group were plotted versus time to examine the stability of the normalized measurements. An exponential curve fit (equation 9) was used to find the stabilization time of the normalized ARFI displacements in the lesion interior and border zone ROI, where t (units, seconds) is time, d_{Final} is the final displacement, $d_{Initial}$ is the initial displacement from the last pre-ablation frame (t = 0 seconds), and τ (units, 1/seconds) is the stabilization time constant.

$$d(t) = d_{Final} + (d_{Initial} - d_{Final})\ e^{-t/\tau} \qquad (9)$$

The time to stabilization was approximated as three times the time constant, or when ~95% of the steady-state was reached.

The C and CNR of the RFA lesion were calculated using the maximum ARFI-induced displacements and B-mode signal intensities from the ROI from inside and

outside the lesion. A one-tailed t-test was performed to confirm an improvement in C and CNR in the ARFI images compared to the B-mode images.

3.2.5 Temporal Stability of Lesion Width and Area

The TTC stained lesion cross-section at the approximate imaging location was examined to compare the final lesion morphology and transmurality.

For each lesion, the normalized ARFI-induced displacements across the lateral FOV at the axial depth dictated by the lesion centroid were compiled in an image and plotted through the time-course to visually examine the stability of the lesion width.

The area of the lesion in each ARFI image was determined by thresholding (mean of displacements in border zone ROI) the normalized displacements and finding the filled area around the composite lesion centroid. For lesions at the edge of the FOV, the area calculation was bounded by the maximum lateral shift of the images through the time-course. The detected lesion area was plotted against time, and the approximate stabilization time was calculated using the exponential fit method described in the previous section.

3.3 Results

A total of 12 lesions were made in six canine subjects. Full analysis was completed for seven lesions; the five unreported lesions had a substantial number of frames removed (low RQ) during the registration analysis, and either had no ARFI

images within five minutes of the ablation (three) or no images past 20 minutes (two). The means and ranges of the RQ for the seven reported lesions are shown in table 4.

Figure 9 and 10 show B-mode, ARFI, and pathology images for two lesions before, during and after RFA lesion formation. The ablation catheter remained in place through the time-course ('stiff' (blue) region with artifact below). During RFA, the normalized ARFI-induced displacements in the myocardium decreased radially from the ablation catheter contact (ACC) point, forming a stiff semicircular lesion. Post RFA, ARFI imaging showed consistent lesion stiffness and morphology through the time-course. In figure 9, the thermocoagulated core was the stiffer (dark blue) in the ARFI images than the lesion border zone (light blue-yellow), identifiable as the less intensely stained brownish-pink rim around the lesion in the pathology image. All lesions that appeared transmural in the ARFI images were confirmed as transmural in the pathology images.

Table 4: Registration analysis of B-mode images.

	Post Ablation Images		
Lesion	**N**	**Mean RQ**	**RQ Range**
A	34	0.88±0.06	0.741 – 0.976
B	48	0.83±0.09	0.662 – 0.952
C	33	0.81±0.12	0.656 – 0.980
D	46	0.85±0.11	0.657 – 0.978
E	48	0.85±0.08	0.668 – 0.973
F	45	0.81±0.09	0.650 – 0.966
G	33	0.87±0.08	0.678 – 0.976

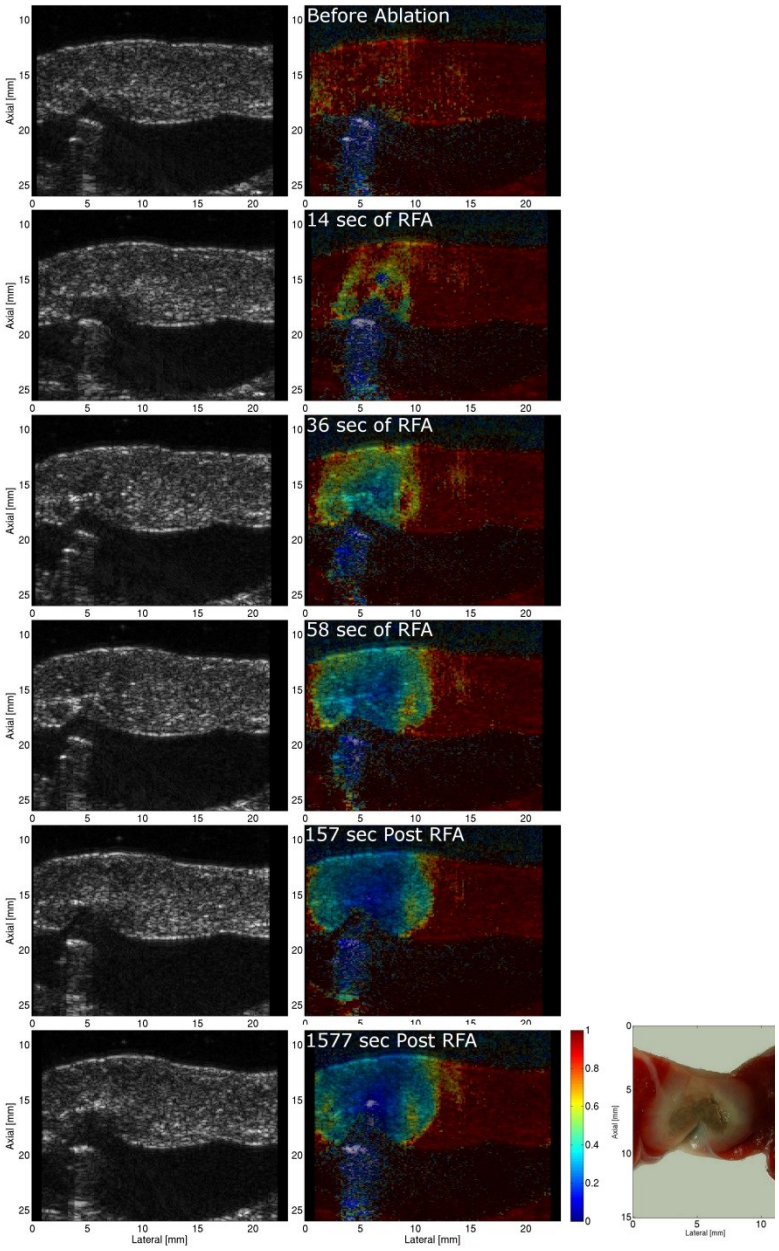

Figure 9: B-mode (left column), ARFI (center column), and pathology (right column) images for RFA lesions formation (lesion C). Before ablation, the normalized ARFI-induced displacements are homogeneous in the myocardium (red). During RFA, a semi-circular region of lower displacement (blue) grows from the ablation catheter contact point on the endocardium. The lesion size did not change significantly during the monitoring time-course and is comparable to the morphology in the TTC stained tissue pathology image at the approximate imaging plane.

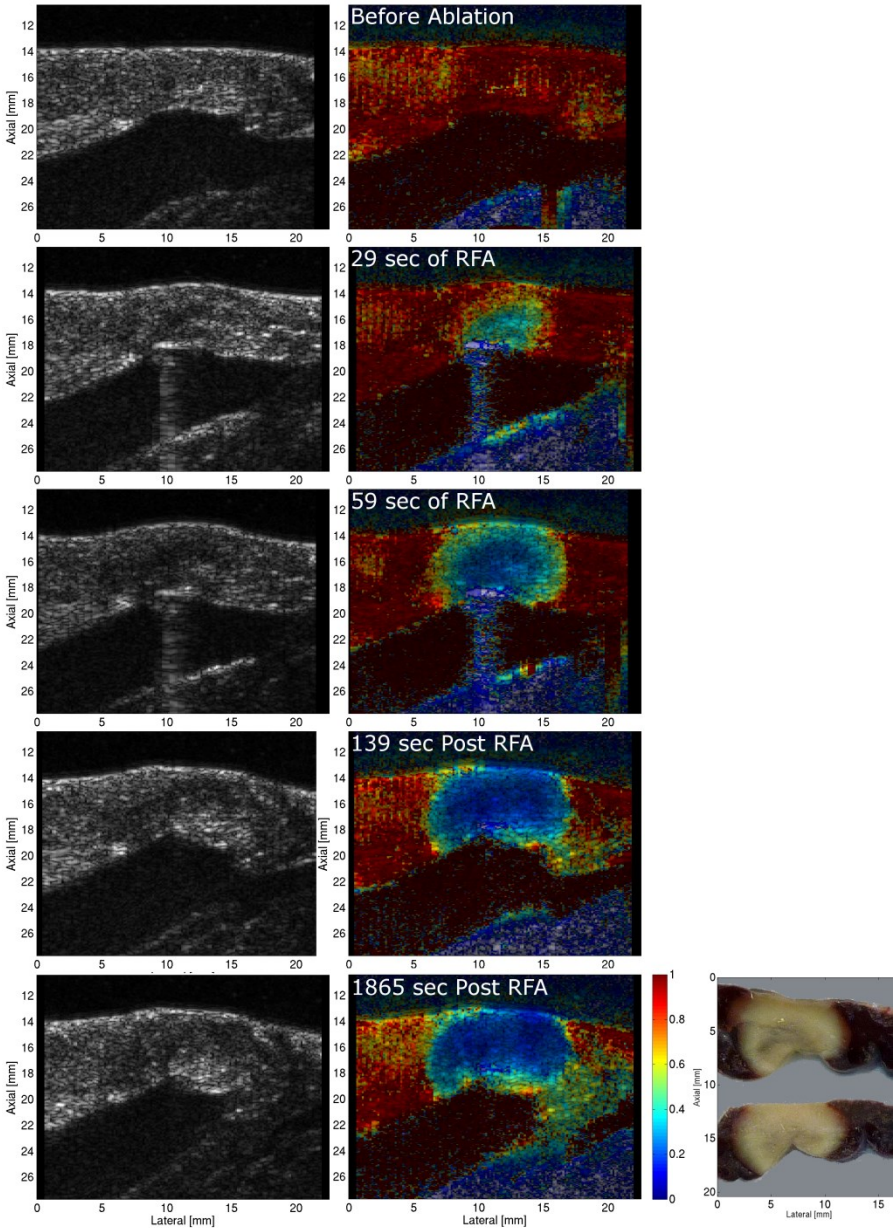

Figure 10: B-mode (left column), ARFI (center column), and pathology (right column) images for RFA lesions formation (lesion A). Before ablation, the normalized ARFI-induced displacements are homogeneous in the myocardium (red). During RFA, a semi-circular region of lower displacement (blue) grows from the ablation catheter contact point on the endocardium (slightly out of plane immediately after RFA). The lesion size did not change significantly during the monitoring time-course and is comparable to the morphology in the TTC stained tissue pathology image at the approximate imaging plane.

Overall, the lesion morphology and transmurality observed in the pathology images were consistent with the lesion morphology seen in the ARFI images.

3.3.1 Temporal Stability and Image Contrast Analysis

Figure 12 shows the post ablation reference B-mode images, ARFI images, and outlined ROI for five lesions. Figure 11 presents plots of the mean normalized ARFI-induced displacements and stabilization curve fits for the ROI inside, at the border zone, and outside the lesions. For all post ablation image ROI (n = 287), the mean normalized displacement values were 0.21±0.06, 0.59±0.12, and 0.90±0.15 respectively. An ANOVA determined RFA lesion had a significant ($p << 0.001$) effect on the normalized displacement means, while the individual lesion did not ($p = 0.425$).

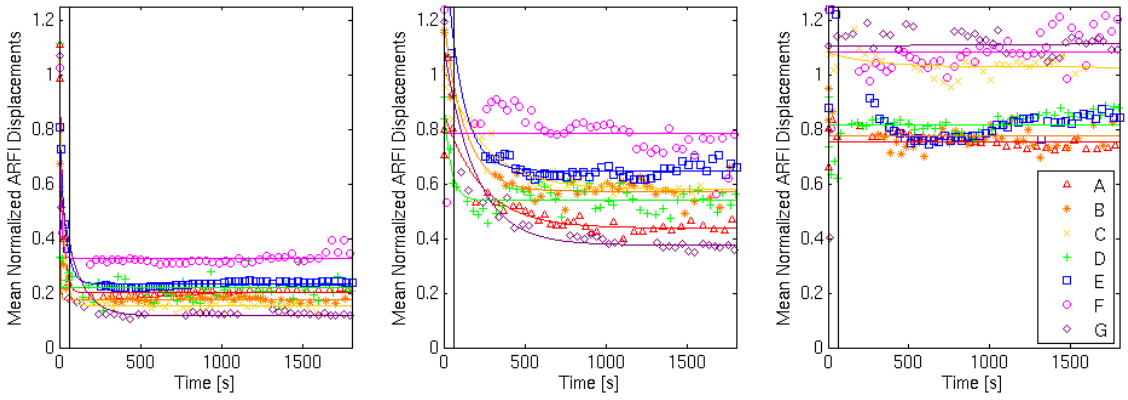

Figure 11: Means of the normalized displacement for the ROI inside the lesion (left), in the lesion border zone (center), and outside the lesion (right) and exponential stabilization curve fits (solid lines). Inside the lesion the normalized displacements reach maximum stiffness within the first two minutes post ablation. In the lesion border zone, the normalized displacements stabilized over the first several minutes post ablation. While showing variability over a narrow range, there was no significant change in the normalized displacements outside the lesion.

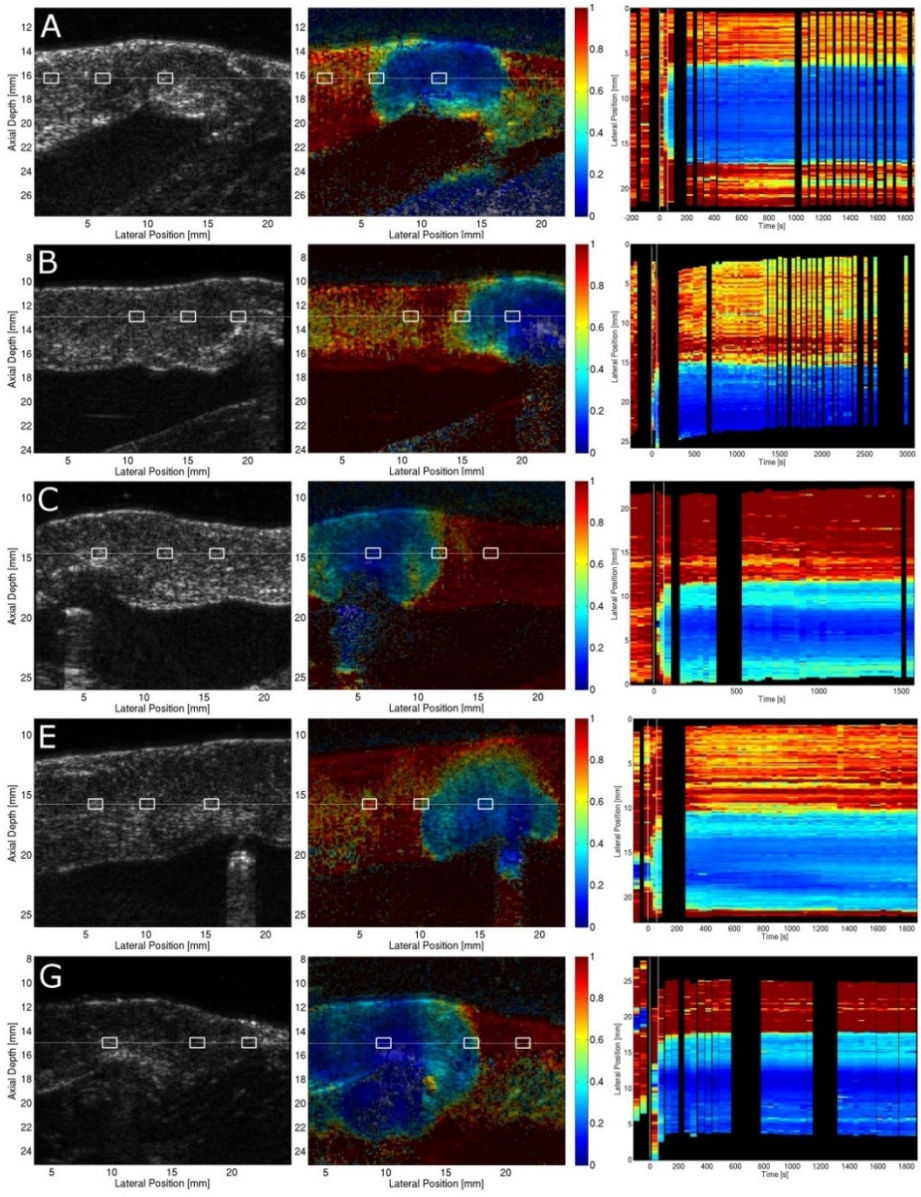

Figure 12: Reference B-mode (right column) and ARFI images (center column) of RV endocardial RFA lesions (lesion groups A, B, C, E, and G). White boxes outline 1x1 mm ROI inside the lesion, in the lesion border zone, and outside the lesion. The displacements at the axial depth delineated by the horizontal white line are plotted for each ARFI image through the time-course (30 second wide bars) to observe the spatial stability of the lesion (right column). The black region represents the temporal gaps or the lateral translation of each ARFI image based on the registration analysis. The ablation occurred between 0 and 60 seconds (white vertical lines). The lesion widths appear consistent through the time-course.

Table 5: Normalized displacement stabilization times and contrast analysis of ARFI and B-mode images of RFA lesions.

Lesion Group	Stabilization Time (sec)			RFA Lesion Contrast Analysis*			
	Lesion Center	Border Zone	Lesion Area	ARFI C	ARFI CNR	B-mode C	B-mode CNR
A	60	689	255	0.73±0.02	6.3±0.83	0.004±0.10	0.16±0.08
B	11	394	88	0.77±0.01	5.1±0.68	-0.17±0.10	0.28±0.15
C	69	737	109	0.85±0.01	6.4±0.97	-0.25±0.06	0.43±0.09
D	6	123	91	0.74±0.05	2.5±0.38	-0.32±0.16	0.49±0.17
E	107	297	120	0.71±0.01	4.8±0.73	-0.11±0.06	0.19±0.10
F†	-	-	-	0.70±0.02	3.2±0.63	0.15±0.06	0.31±0.12
G	302	575	463	0.89±0.01	3.5±0.94	-0.27±0.13	0.40±0.19
Mean	**92±109**	**469±239**	**188±149**	**0.77±0.07**	**4.5±1.52**	**-0.14±0.17**	**0.33±0.12**

***** Right-tailed paired t-test for C ($p = 8.9e-9$) and CNR ($p = 4.8e-6$) between ARFI and B-mode images.
† Lesion F: pre-ablation and lesion formation image occurred at different imaging position than the remainder of the time-course due to a large elevation shift of the transducer shift immediately following ablation.

The normalized displacement stabilization time and results of the contrast analysis are presented in table 5. A one-tailed paired t-test determined the mean C and CNR were significantly higher in the ARFI images than the B-mode images.

3.3.2 Temporal Stability of Lesion Width and Area

The compiled normalized ARFI-induced displacements for single axial location (axial depth delineated by white horizontal line) through the time-course is shown in figure 12. The locations of the lesion borders displayed temporal stability.

Figure 13 plots the detected lesion area and stabilization curve fits for each of the seven lesions. In all lesions, the detected area grows rapidly during RFA and stabilizes within the times presented in table 5. The mean increase in lesion area was 11.2±7.2% between the first post ablation image and the last (range 2.7-24.4%), and the lesion area stabilized within ~2 minutes of the ablation.

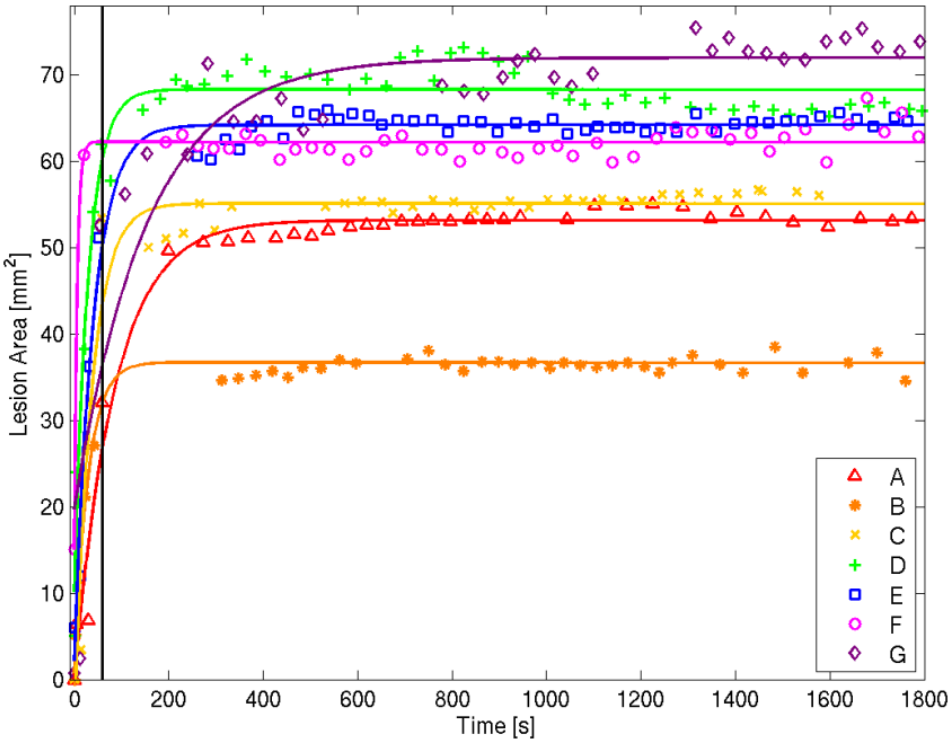

Figure 13: Time-course of RFA lesion area as detected by ARFI imaging. RF-energy delivery commenced at 0 sec and was terminated after 60 sec (black vertical line). Exponential stabilization curve fits are plotted as solid lines.

3.4 Discussion and Conclusions

This chapter described a method for monitoring cardiac RFA lesion formation *in vivo* and as well as the spatial and temporal stability of the lesion with ARFI imaging. The results showed ARFI imaging can successfully identify acute stiffness changes in RFA treated myocardium *in vivo* with good repeatability and high image contrast.

ARFI imaging measured a significant reduction in normalized ARFI-induced displacements in RFA lesion, and the normalized displacements in the lesion center stabilized within the first minute post ablation. The normalized displacements in the

border zones were stable within 10 minutes. The detected lesion area stabilized approximately 2 minutes after ablation, and the mean change in area over the post ablation monitoring time for all lesions was ~11% and no more that 25% for any individual lesion.

Tissue cooling following RF-delivery is not instantaneous; the myocardial temperature at RFA sites has been shown to remain in the hyperthermic injury range for almost a minute post ablation until convective cooling and tissue perfusion return the tissue temperature to baseline.[140-142] The 1-2 minute stabilization times for the lesion center and lesion area were consistent with this observation. The measurements of the relative tissue stiffness were stable through the remaining time-course.

3.4.1 Implications for Clinical Lesion Assessment

3.4.1.1 Edema at the RFA site

Lardo *et al*. conducted a comprehensive assessment of the temporal and spatial stability of RFA lesions in canine RV with MRI (T2 weighted fast-spin echo). This study found the lesion image intensity increased and plateaued after the first 10-12 min post ablation (temporal resolution of 2 minutes) once the hydrostatic pressure and edema infiltration equilibrated.[79] This study also showed the MRI imaged lesion size stabilized in the first 5-6 min of lesion formation and slightly overestimated the size of the lesion when compared to a histological cross-section of the tissue.

In this chapter, the detected lesion area based on the ARFI measured relative stiffness stabilized in the first 1-2 min after RF-delivery; therefore the ARFI imaging evaluation of tissue damage based on the stiffness changes at the ablation site stabilized faster than the MRI visualized changes in water content which was largely affected by edema. This finding suggests that the measured ARFI-induced displacements were not significantly confounded by any increase in the interstitial tissue pressure caused by edema around the ablation site.

3.4.1.1 Necrosis at the Lesion Boundary

It has also been shown that actin-myosin contraction band necrosis can be present around the edge of RFA lesions *in vivo*.[99, 143, 144] Possible mechanisms for the appearance of these bands are: 1) local ischemia due to decreased perfusion at the ablation site, or 2) a heat-induced rise in myocyte calcium influx that causes hypercontraction and cell death due to cytosolic calcium overload.[43, 145, 146] Studies have shown lesions composed of high concentrations of these bands appear in canine myocardium within 6 to 10 minutes of exposure to cardiotoxic doses of isoproterenol. The spatial and temporal formation of these bands during RF ablation has yet to be characterized.[146-148] It also remains unclear whether all contraction band necrosis becomes chronic scar.[143, 149] Edema accumulation from ruptured cells and micro-vessels has also been observed in areas of contraction band necrosis.[144]

In this study, this banded zone (incomplete thermocoagulation) at the lesion boundaries was presumably stained lighter pink in the TTC pathology images; the relative stiffness gradient (light blue-yellow spectrum, see figure 9) observed at the RFA lesion edge in the ARFI images often showed similar morphology to this boundary in the pathology images. Also, the longer and highly variable relative stiffness stabilization times for the border zone ROI likely reflected the spatial density and dynamic stiffening of the contraction bands and associated edema. A stiffening of these areas, as opposed to "growth" of the lesion, is consistent with the finding that the lesion width and area were stable within minutes post-ablation. Due to the ambiguity of determining myocyte death this region, in a clinical setting ablating the tissue to the blue spectrum (> ~30% of pre-ablation ARFI-induced displacement) of the ARFI imaging color scale would ensure complete RF ablation.

Overall, a better understanding of the connection between acute lesion compliance (protein coagulation, contraction band necrosis, and edema) and the degree of electrical damage could provide a method to distinguish viable or electrically "stunned" tissue from complete thermocoagulation and unablated myocardium. Elasticity-based evaluation of RFA lesion could also potentially provide a method to optimize the RF-energy delivery and avoid complications associated with excess delivery of RF-energy.

3.4.2 Study Design and Limitations

The exact experimental setup described in this study is not a clinically executable method. Given the study objectives, this experimental method was used because it 1) maximized the stability of the imaging plane during the ablation and time-course monitoring, 2) minimized any interference from the RF-energy application because ICE catheter transducers are unshielded and experience interference in the ultrasound signal when RF-energy is applied, and 3) maximized the ARFI imaging FOV.

A direct comparison between the ARFI imaging determined lesion area and the stained lesion pathology was not done in this experiment due to the likelihood of large misregistration errors between the pathology cross-section and the actual imaging plane. Moreover, several lesions were imaged at the edge of the FOV; attempting to spatially align the edges of the imaging plane to the pathology image would also have created errors in the area measurements. Despite any misregistration of the pathological lesion cross-sections, it was valuable to observe and compare the lesion morphology and transmurality to the ARFI image.

The stability of the imaging plane was the primary cause of variation and error in this study. The 2-D normalized cross-correlation was able to adjust for axial and lateral shifts of the imaging plane, but was unable to correct for any elevation or angular translation. Slight changes in the imaging location may have resulted in the imaging of a completely different cross-section of the lesion. Changes in the heart rate may also

have caused temporal variation in the ARFI images. The diastolic delay was held constant over the time-course and variations in the heart rate would acquire a slightly different point in the cardiac cycle. Regardless, any instability of the imaging planes did not appear to affect the findings of this study.

3.5 Acknowledgements

For their contributions to this work, I acknowledge Dr. Maryam Vejdani, Young Kim, Kelly Kang, and Virginia Chen.

Chapter 4: Integration of ARFI Imaging and Electroanatomical Mapping for Intraprocedure Intracardiac Radiofrequency Ablation Lesion Assessment

The work described in this chapter is under review for publication in Ultrasonic Imaging:

Eyerly SA, Bahnson TD, Koontz JI, Bradway DP, Dumont DM, Trahey GE, Wolf PD. Contrast in intracardiac acoustic radiation force impulse images of radiofrequency ablation lesions.

4.1 Introduction

In chapter 3, a method for acquiring high contrast ARFI images of RFA lesions in an *in vivo* open chest setup was described. While a successful experiment for precisely monitoring lesion formation and temporal-spatial stability, clinical TCA procedures are conducted in a closed environment with catheters; the use of a linear transducer to directly image the heart during clinical ablation procedures is not feasible.

Real-time ICE has become an important tool for imaging cardiac anatomy and ablation catheter-myocardium contact during clinical TCA procedures. Intracardiac ARFI imaging sequences were developed for the standard ICE transducer often used in TCA cases.

Unlike real-time ICE imaging, 2-D ARFI imaging requires a diastolic gated 50-100 ms acquisition time which limits the display update time interval to the order of

seconds. This frame rate makes it difficult to "scan" the heart for lesions during a TCA procedure. ARFI imaging from an ICE transducer also limits the FOV, as wide beam steering angles have shown a substantial decrease in the ARFI-excitation energy and the resulting displacements.[96] Therefore, a method for using EAM to precisely guide the ARFI imaging plane to RFA lesion sites during TCA was established. Background information about the CARTO EAM system is provided in appendix A.

The first objective of this chapter was to verify the integration of a multi-modality ARFI imaging-EAM system for efficient intraprocedure ARFI imaging of RFA lesions. With this system, the ARFI imaging plane could be navigated to RFA delivery locations marked in the electroanatomical map, and the EAM system RFA markers were treated as positive indicators for the presence of RFA lesions. This multi-modality system was then used to 1) determine the accuracy of identifying RFA lesion delivery locations in electroanatomical maps with ARFI images, 2) quantify the typical ARFI-induced displacement ranges achieved by the ICE transducer in RFA lesion and unablated myocardium, and 3) calculate and compare the C and CNR between RFA lesion and unablated myocardium for ARFI and conventional ICE images.

The chapter is organized as follows: Section 4.2 describes the ARFI imaging-EAM system integration as well as the animal experimental protocols to verify the system and assess linear RFA with intraprocedure ICE-based ARFI imaging. Section 4.3

describes the results from the system verification and linear RFA experiment, and section 4.4 discusses the findings and the utility of the integrated system.

4.2 Methods

The animal study protocol executed in this chapter was approved by the Duke University Animal Care and Use Committee and conformed to the Guide for the Care and Use of Laboratory animals.[16]

All canine subjects were anesthetized (pre-anesthesia: intramuscular acepromazine 0.02-0.05 mg/kg followed by interveinous propofol 4-6 mg/kg; general anesthesia: isoflurane gas 1-5% via inhalation), intubated, ventilated and maintained metabolically stable.

4.2.1 Multi-Modality Imaging System

4.2.1.1 ARFI Imaging Sequences and Image Processing

An ACUSON S2000™ ultrasound scanner (Siemens Healthcare, Issaquah, WA, USA) was software modified to implement 2-D ARFI beam sequences from a standard 64 element SoundStar™ catheter phased-array (Biosense Webster, Diamond Bar, CA, USA). Images were acquired with transmit and receive center frequencies of 6.15 MHz and with a 1.5 cm focus (F/# = 2.14). The imaging parameters are summarized in table 6.

The first part of the imaging sequence consisted of a 90° B-mode image. Next, ten high intensity ARFI priming-pulses were transmitted to linearize the transducer kick-back so it could be easily filtered from the ARFI-induced displacement profiles (see

section 2.4.3.1).[96] The next step in the imaging sequence was to acquire a 2-D (~54° FOV) ARFI image consisting of 42 equispaced spatially-interleaved (wiper-bladed) ARFI locations. Each lateral ARFI-excitation location was interrogated with 8 scan-lines before the excitation at a tracking PRF of 9.7 kHz.

Table 6: 2-D ICE-based ARFI imaging parameters.

Transducer	Probe	SoundStar™ (10 French)
	Elements	64 (7 mm length)
	Array Type	Phased
	Center Frequency [MHz]	6.15
Scanner	Model (Siemens)	S2000™ (ACUSON)
	Data Type	RF
B-mode and ARFI Imaging Parameters	Transmit/Tracking Frequency [MHz]	6.15
	Sampling Frequency [MHz]	40
	Focus	1.5 cm
	F/#	2.14
	Cycles	300
	ARFI push length [μs]	55
	ARFI lateral push locations	42 (54°)
	Parallel tracking	1:1
	Pre-tracks	8
	Post tracks	9
	Tracking PRF [kHz]	9.7

Hsu *et al*. determined the peak intracardiac ARFI-induced displacement in myocardium occurred ~0.60 ms post-excitation, thus the excitation location was tracked for 0.6 ms (9 scan-lines) to capture the peak tissue response while minimizing the acquisition time.[96] The total tracking time at each ARFI-excitation location was ~1.1 ms. Hsu *et al*. determined unablated and ablated myocardium fully recover to the pre-

excitation baseline after ~2.2 ms. The spatial-interleaving of the sequential excitation locations during the acquisition ensured the local tissue was unaffected by the previous ARFI-excitation.[95] The full imaging sequence took ~92 ms to complete and was within regulatory limits for mechanical index (MI < 1.7) and transducer surface heating (< 4.0°C).[150]

The ARFI image processing was completed offline after the experimental procedure. The 2-D ARFI images were formed using the normalized cross-correlation time-delay displacement estimation method outlined by Hsu *et al*.[96] A normalized CCC was calculated for each pixel location to quantify the quality of the phase-matching between the post ARFI scan-lines and the last pre-ARFI line (reference line). A low CCC for a displacement value indicated phase decorrelation during the cross-correlation, and therefore a poor displacement estimation. Poor displacement estimates were removed from the ARFI images by thresholding the median CCC (median CCC through tracking time was spatially median filtered by a ~0.5 mm axial by 4 mm lateral kernel) to include only values greater than 0.80. This processes eliminated most of the pixels from the blood in the RA.

The ARFI-induced displacement measurements were motion filtered with a quadratic extrapolation model to reduce the effects of axial physiological motion and catheter rebound on the displacement estimates.[96, 136, 151] An example of a displacement profile for a single pixel in unablated myocardium is presented in figure 14.

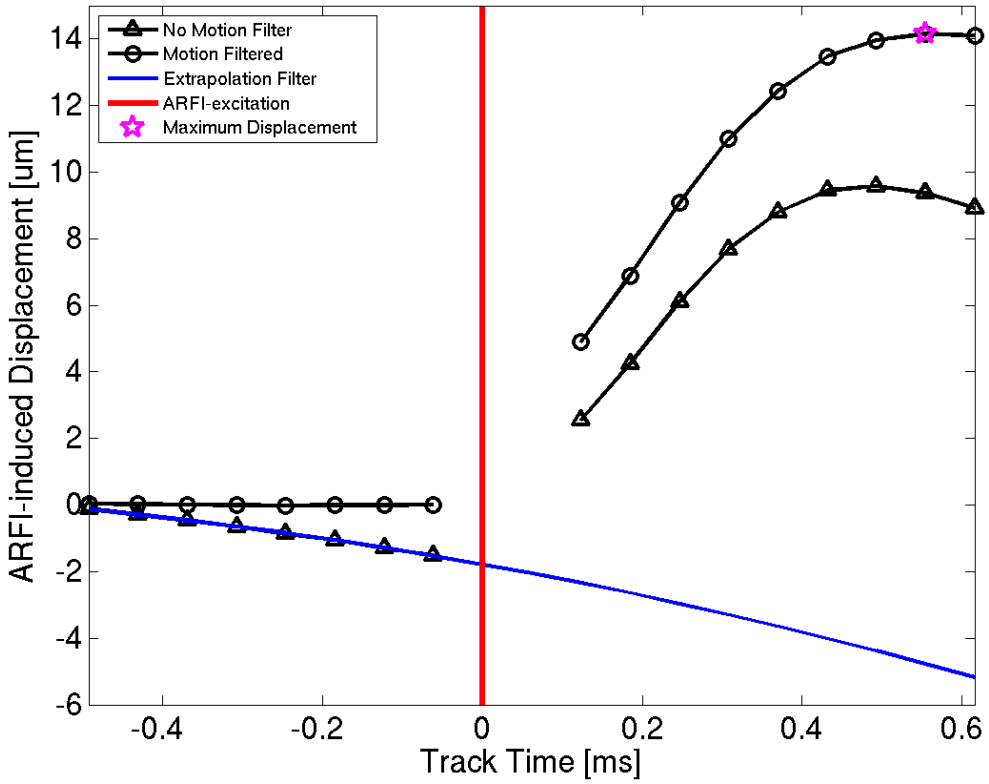

Figure 14: ARFI-induced displacement curve for a single pixel location in the myocardium imaged with an ICE transducer. In the ICE imaging sequences, 10 priming pulses were delivered to linearize the transducer kick-back. As a result, the catheter is recovering towards the myocardium during the eight pre-excitation scan-lines. This motion was removed from the raw displacements (triangles) using the quadratic motion function (blue) extrapolated from the pre-track data to create a profile of only the ARFI-induced displacement (circles). Nine scan-lines were collected to monitor the post-excitation tissue displacement. Total tracking time for a single line was ~1 ms. The maximum displacement over the tracking time (magenta star) was the pixel value in the 2-D ARFI image.

Remaining pixels in the blood or beyond the myocardium were masked from the image by removing individual locations if the measured displacement estimation was > 50 μm (likely noise) or the standard deviation of the displacement measurements through the tracking time was greater than 20 μm. The maximum ARFI-induced

displacement measurements were scan-converted (bilinear interpolation scan-conversion, 0.019 mm axial by ~1.33° lateral kernel pre scan-conversion, 0.05x0.05 mm pixel size post scan-conversion), color-coded at each pixel location, and overlaid onto the scan-converted B-mode image. The ARFI image pixel color scale was manually adjusted to increase the visual contrast and reduce saturation in the final displayed image. The upper limit of the displayed displacement range for all images was between 7.5 and 15 μm.

4.2.1.2 Hardware and Software Integration

The developed multi-modality imaging system consisted of a modified CARTO XP™ EP Navigation System (Biosense Webster; Diamond Bar, CA) and the software modified Siemens ACUSON S2000™ ultrasound scanner (Siemens Healthcare; Issaquah, WA). The S2000 platform used for this research was not supported by the CARTO XP software, and custom hardware and software modifications were made to the CARTO XP to complete the integration.

In the standard clinical system, the CARTO XP EAM system connects to a supported ultrasound scanner with an Ethernet cord and proprietary video cable. The CARTO XP software retrieves the ultrasound imaging parameters, such as the imaging fan depth, through the Ethernet connection and crops the real-time ICE video from the scanner to display in the electroanatomical map. To receive the correct video input from the S2000 scanner, a compatible frame grabber card (Vio Analog, VIO7IAOA/G*: Matrox

Electronic Systems Ltd., Dorval, Quebec, Canada) was installed in the CARTO computer tower to accommodate the video resolution output by the S2000. A custom Matrox Intellicam software (Matrox Electronic Systems Ltd., Dorval, Quebec, Canada) parameters file was developed with the assistance of Matrox to accept the exact video specifications of the S2000 output. A CARTO XP software update (V9.7) and a parameter "simulating" software (modified from the supported ACUSON X300™, Siemens Healthcare; Issaquah, WA;) provided by the Biosense Webster CARTO Software Development team (Tirat Carmel, Israel) was installed on the CARTO XP system to correctly crop and display the S2000 video signal in the CARTOSound™ Ultrasound Viewer window. The simulator provided modifiable, hard coded XML files to provide the imaging parameters from the S2000 scanner to the CARTO XP software. The S2000 parameter values were found in the scanner Diagnostic User Interface (DUI) and with a screenshot of the S2000 imaging software. Once the video input and XML file modification was complete, the real-time ICE imaging fan was visible in the CARTO XP ultrasound viewer.

4.2.1.3 Imaging System Implementation and Equipment Setup

The ARFI imaging-EAM integrated system used a commercially available unmodified 10 French SoundStar™ catheter (Biosense Webster; Diamond Bar, CA) to acquire spatially registered B-mode and ARFI images. Preliminarily processed ARFI

images were displayed on a laptop computer (Dell Precision M90) within 15 seconds of the acquisition during the procedure.

Catheters were navigated to the heart with fluoroscopy (Philips Healthcare; Andover, MA). All focal RFA lesions were delivered with a Stockert 70 radiofrequency generator (RFG) and NaviStar mapping/ablation catheter (Biosense Webster; Diamond Bar, CA). An octapolar reference catheter (XT™ Steerable, Bard; Lowell, MA) was positioned in the CS and the distal electrodes were used as pacing electrodes (Pulse Stimulator, Grass Technologies; West Warwick, RI).

The surface ECG and endocardial EG from the electrodes of the reference (R1-R8) and mapping (M1-M4) catheters were acquired by the CARTO patient interface unit (PIU), input into an Octal Bio Amp (ADInstruments; Milford, MA) using a custom fabricated cable (figure 15), and recorded using LabChart 7.0 data acquisition software (PowerLab, ADInstruments). In LabChart, an output channel was configured to provide an impulse at a user selected delay after a detected QRS of the ECG. This pseudo-ECG output signal was fed to the ultrasound scanner using a custom fabricated cable (figure 16) and used to gate the image acquisitions. The output signal was also input into the CARTO PIU (custom fabricated cable, figure 17) as a pseudo-EG signal to synchronize the CARTO XP position recoding and display (position data acquired once per heart beat) with the gated ARFI image acquisition.

A diagram of the full equipment setup is presented in figure 18.

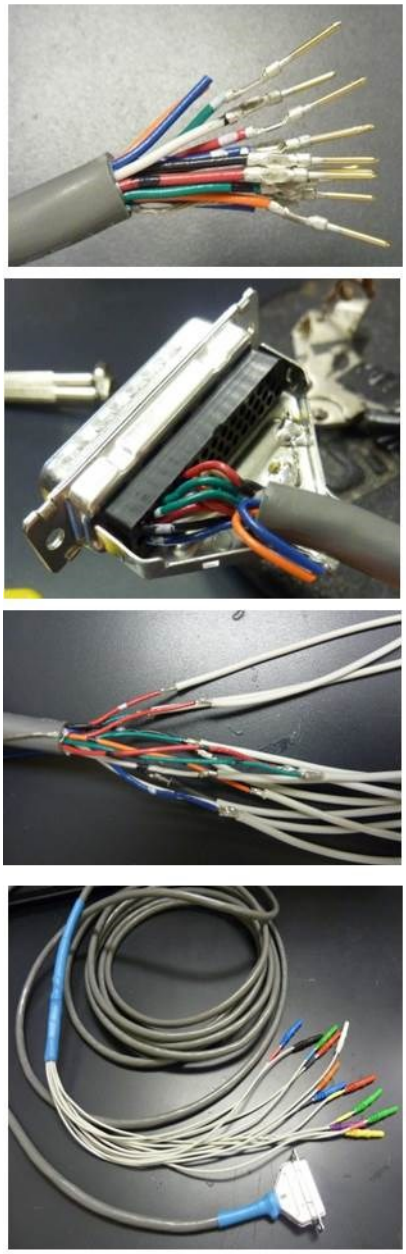

CARTO PIU
D-sub IC Output

IC Signal	Pin	Color
M1	5	White
M2	35	Green-Red
M3	21	Green-Yellow
M4	6	Green-Blue
R1	1	Red-Yellow
R2	31	Red-Black
R3	17	Orange
R4	2	Yellow
R5	32	Blue-Red
R6	18	Blue-Black
R7	3	Purple
R8	33	Black

Octal Bioamp System
2 mm pin inputs

Figure 15: Custom cable for transferring intracardiac (IC) EG recorded by the reference catheter (R1-R8) and mapping catheter (M1-M4) from the CARTO system to the bioamp data acquisition system.

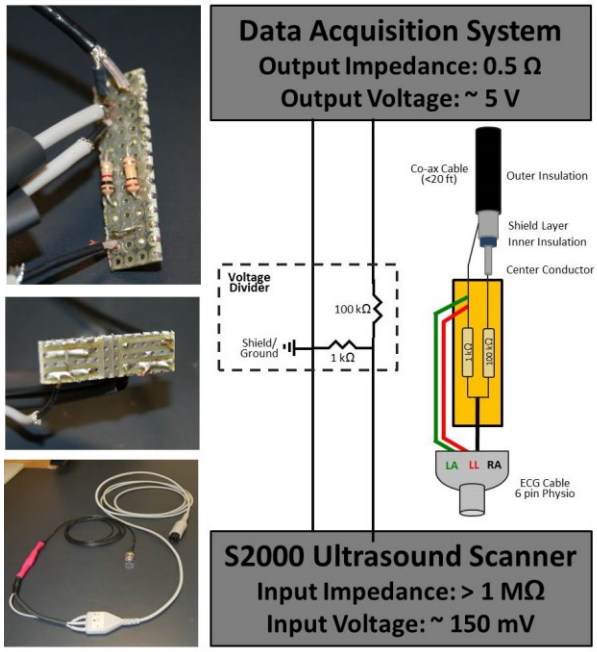

Figure 16: Custom cable to for input of pseudo-ECG from data acquisition system to the S2000 ultrasound scanner.

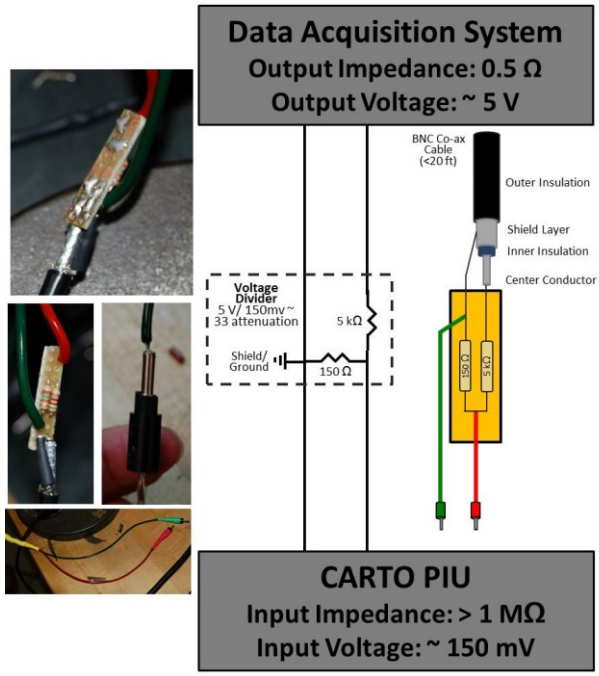

Figure 17: Custom cable to for input of pseudo-EG synchronization signal from data acquisition system to the CARTO.

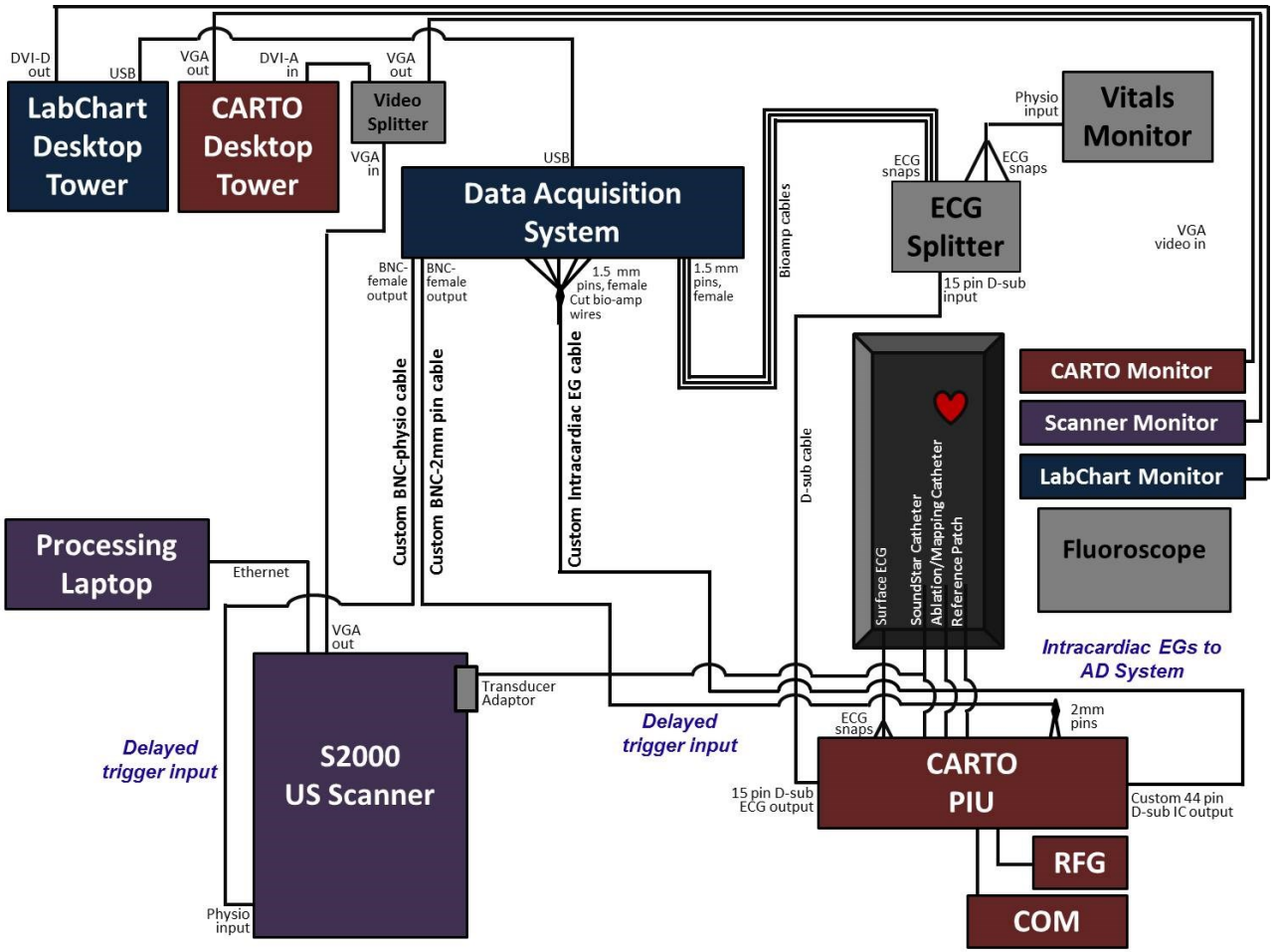

Figure 18: Diagram of ARFI imaging-EAM equipment and cable connections.

4.2.2 Integrated System Verification

The integrated system was tested in two canine subjects to confirm the spatial registration of the imaging plane and CARTO geometry. In the first canine subject, the integrated CARTO system was used to steer the ARFI imaging plane to interrogate two single RFA lesions before and after ablation. In a second canine, two parallel rows of RFA lesions were delivered in the RA, and the integrated system was used to visualize and ablate the unablated gap between the RFA lines.

4.2.3 ARFI Imaging of Linear RFA

A linear ablation was performed in eight canine subjects. A baseline point-by-point geometry of the RA was made with the ARFI imaging-EAM system. A guideline delineating the planned linear RFA delivery site was drawn on the map geometry, and EAM directed ARFI images of the pre-ablated tissue regions were acquired. A series of lesions were delivered along the guideline using a catheter dragging technique to minimize potential lesion line discontinuities, and the RFA sites were marked in the EAM geometry.[152] The ablation proceeded in two steps: first, the linear ablation left an intentional gap of approximately 1 cm length, and then the gap was closed with consolidating RFA lesions. The ablation catheter tip was temperature controlled between 50-60°C and RF-energy was applied for ~30-90 seconds per line segment. ARFI images

were acquired before and after RFA using the EAM geometry and guideline markers to direct the imaging.

The ablation catheter was removed from the FOV during ARFI imaging because the catheter tip blocked acoustic energy from reaching the myocardium, creating a distinct shadowing artifact. Also, the ICE catheter was positioned such that the endocardium appeared near the focus and as parallel to the transducer face as possible. This was done to maximize the induced displacement and to minimize depth dependent energy delivery to the tissue.[25, 96, 139] ARFI images where the endocardial surface was outside the focal DOF (above 0.5 or below 2.25 cm) were not included in the statistical analysis. Images were also excluded if the myocardium was at an angle greater than 50° because the depth dependent difference in acoustic energy-delivery could potentially be mistaken for RFA treatment.[139]

After the procedure, the heart was removed and photographed to confirm the presence of RFA lesions at the approximate sites shown in the electroanatomical map.

4.2.3.1 ARFI Image Review for the Presence of RFA Lesion

Three reviewers read the processed ARFI images for the absence or presence of RFA lesion in the myocardium at the imaging location, identifying lesion as at least one area (larger than approximately 0.5x0.5 mm) of low relative ARFI-induced displacement. The ARFI images were randomized, and each reviewer was blinded to the CARTO

maps, canine subject, and stage of ablation. The majority assessment was used as the final classification of the image, and the level of agreement between the reviewers was quantified with a kappa coefficient. In the CARTO maps, the ARFI imaging plane transecting any part of a 4 mm spherical RFA marker was used to indicate the presence of a RFA lesion at the imaging location. Each image was categorized in a 2x2 contingency table, and the sensitivity and specificity were calculated.

4.2.3.2 Contrast Performance Analysis of ARFI-induced Displacements in Unablated vs. Ablated Myocardium

A reviewer was blinded to the ARFI images and used the CARTO maps of the RFA markers and ICE-fan projection to classify each location as imaging no lesion (fan did not intersect markers), non-contiguous lesion (fan partially intersected marker lines), or contiguous lesion (fan completely intersected marker lines). Images that partially intersected RFA marker lines were used for the contrast analysis. For these images, the reviewer manually selected an ablated and unablated area in the myocardium on the B-mode image that matched to the marker intersection of the fan in the EAM map. This selection dictated the location of two (one ablated, one unablated) 1x1 mm (20x20 pixels) regions of interest (ROI) in the spatially registered ARFI image. For the ARFI images of no lesion and contiguous lesion, a 2x1 mm (40x20 pixels) region of interest was taken from the center of the FOV. Each image contributed the same number of data points

(800 total pixels) to the analysis. The 1 mm axial depth for the ROI was chosen because the atrial myocardium was typically between 1.5 and 2 mm thick. All ROI were taken 0.25 mm below a manual trace of the endocardial surface on the B-mode to ensure the measurement region was within the myocardium.

The mean and standard deviation of the ARFI-induced displacement (no spatial median filter) were calculated for the pixels in each ROI. A repeated measures ANOVA to test for the RFA lesion effect was performed on the ROI displacement values. This statistical model was used because multiple lesions were created in each animal.

The C and CNR were calculated for each image containing both ablated and unablated myocardium. The C and CNR were also calculated for the mean signal amplitude in the spatially registered ROI in the B-mode images. A repeated measured ANOVA for lesion was performed on the measured ROI displacement means. Additional repeated measure ANOVA tests were performed on the C and CNR values in the ARFI and B-mode images. A one-tailed paired t-test was used to determine if there was a significant increase in the C and CNR of lesion in the ARFI images over the B-mode images.

4.2.3.3 Bulk Motion Artifacts

The motion filtering technique described previously reduced the effects of bulk axial motion on the ARFI-induced displacement estimates, but large motion artifacts

(severe decorrelation of the track-lines) occurred if an acquisition was mistimed to acquire partially in systole or during an irregular heartbeat such as a premature ventricular contraction (PVC). The ARFI image scan-lines were acquired at spatially-interleaved lateral locations; therefore if substantial lateral or axial motion occurred during the acquisition, the endocardial surface was discontinuous or "jagged" in the B-mode image compiled from the pre-ARFI excitation RF track-lines (figure 19). Motion artifacts also presented a distinct "streaking" pattern in the displacement estimates that corresponded to the tracking of the largely decorrelated bulk cardiac motion instead of the ARFI-induced displacements.

ARFI images exhibiting such motion artifacts or images where more than 50% of the displacement estimates in the myocardium had cross-correlation coefficients below 0.80 were not included in the statistical analysis (28 of 247 total images).

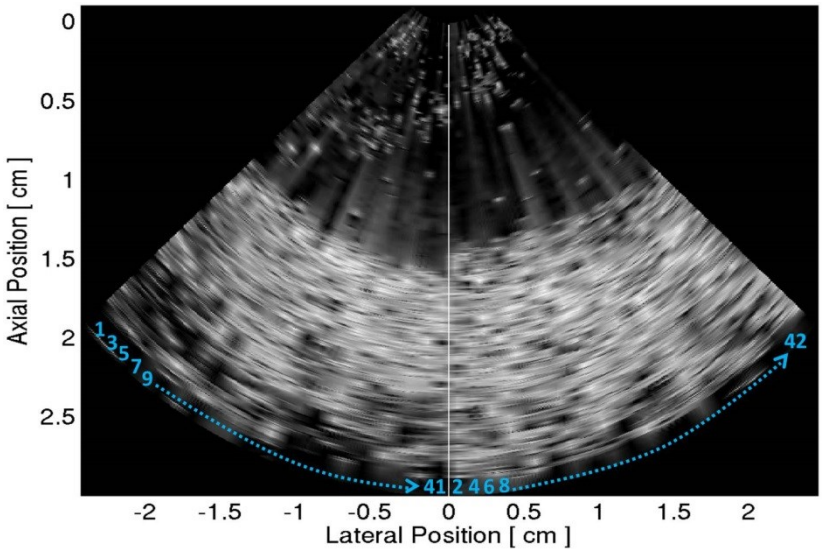

Figure 19: Motion artifact in B-mode image (RF data). The ARFI lines were acquired at the spatially interleaved locations dictated by the order of the blue numbers. A total of 42 lines were acquired across the FOV (before scan conversion). There is a discontinuity at the myocardial surface in the center of the field of view (white line) that shows the tissue had moved between the acquisition of the center line acquired at the beginning of the sequence and the line to the left that was acquired at the end of the sequence.

4.3 Results

4.3.1 Integrated System Verification

Figure 20 shows ARFI images of a right atrial RFA target site mapped in the CARTO geometry before (white sphere) and after (red sphere) ablation. Post ablation, there is a clear area of increased stiffness in the location of the CARTO RFA marker. Figure 21 is a second example of ARFI imaging of a single RFA lesion site in the RV. There is a region of increased stiffness at this location where the imaging plane intersects

the RFA marker. In figure 22, ARFI imaging verified an unablated gap between two parallel lines of RFA lesions after ablation. When consolidating RFA was delivered, the gap of relatively low ARFI-induced displacements became stiffer. These results verified the ARFI imaging plane was accurately imaging RFA delivery locations using the CARTO map as a guide.

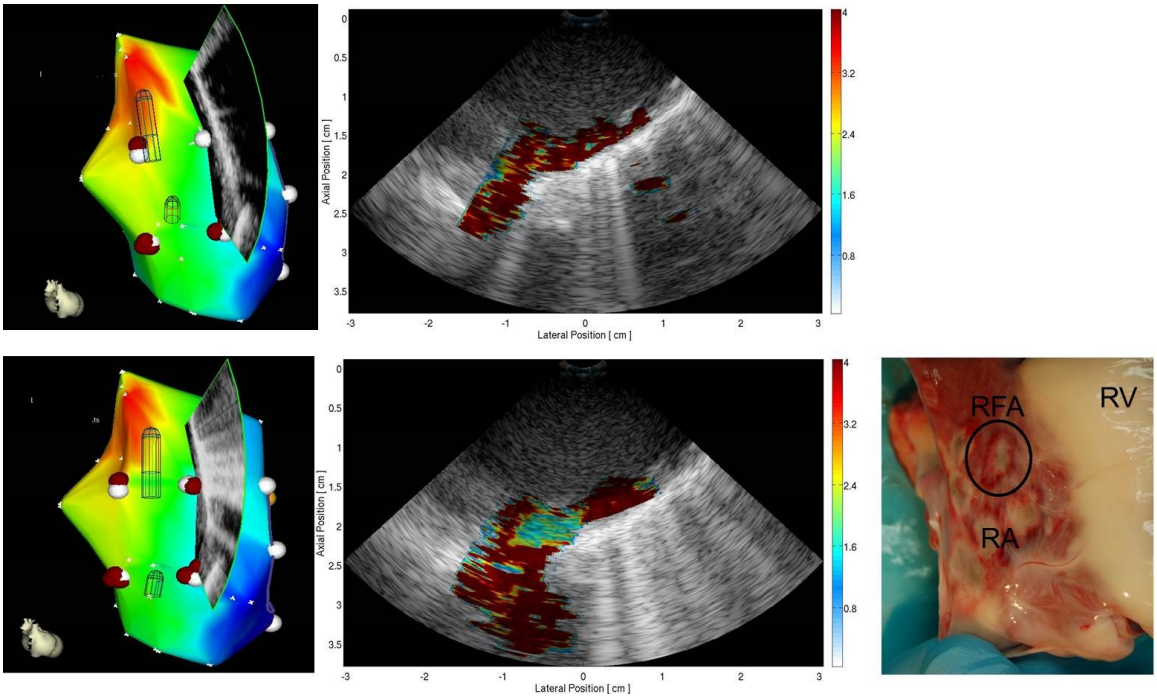

Figure 20: CARTO maps (left) and ARFI images (center) of a single RFA lesion in the right atrium (RA) before and after radiofrequency ablation (RFA). Post ablation the ARFI image shows a decrease in the relative ARFI-induced displacement (μm) where the imaging plane transects the RFA lesion site (red sphere) in the CARTO map. An image of the tissue pathology (right) confirmed the presence of a transmural lesion.

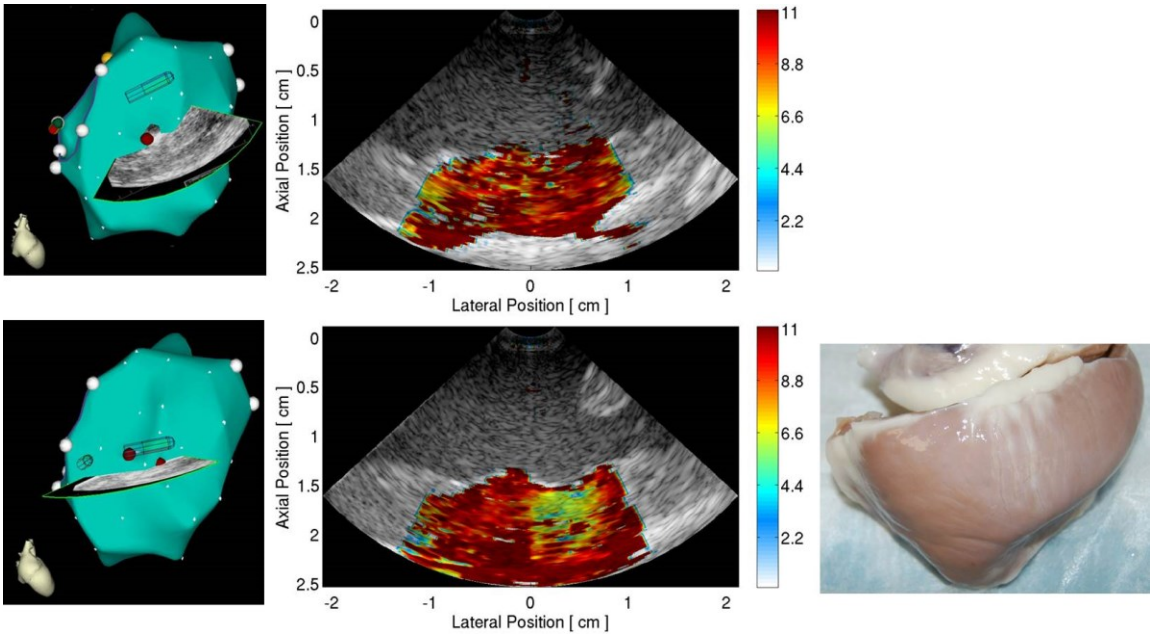

Figure 21: CARTO maps (right column) and ARFI images (center column) of single RFA lesion in the right ventricle (RV) before and after ablation. Post ablation the ARFI image shows a decrease in the relative ARFI-induced displacement (μm) where the imaging plane transects the RFA lesions site (red sphere) in the CARTO map. An image of the RV epicardial surface (right column) confirms the RFA lesion was not transmural.

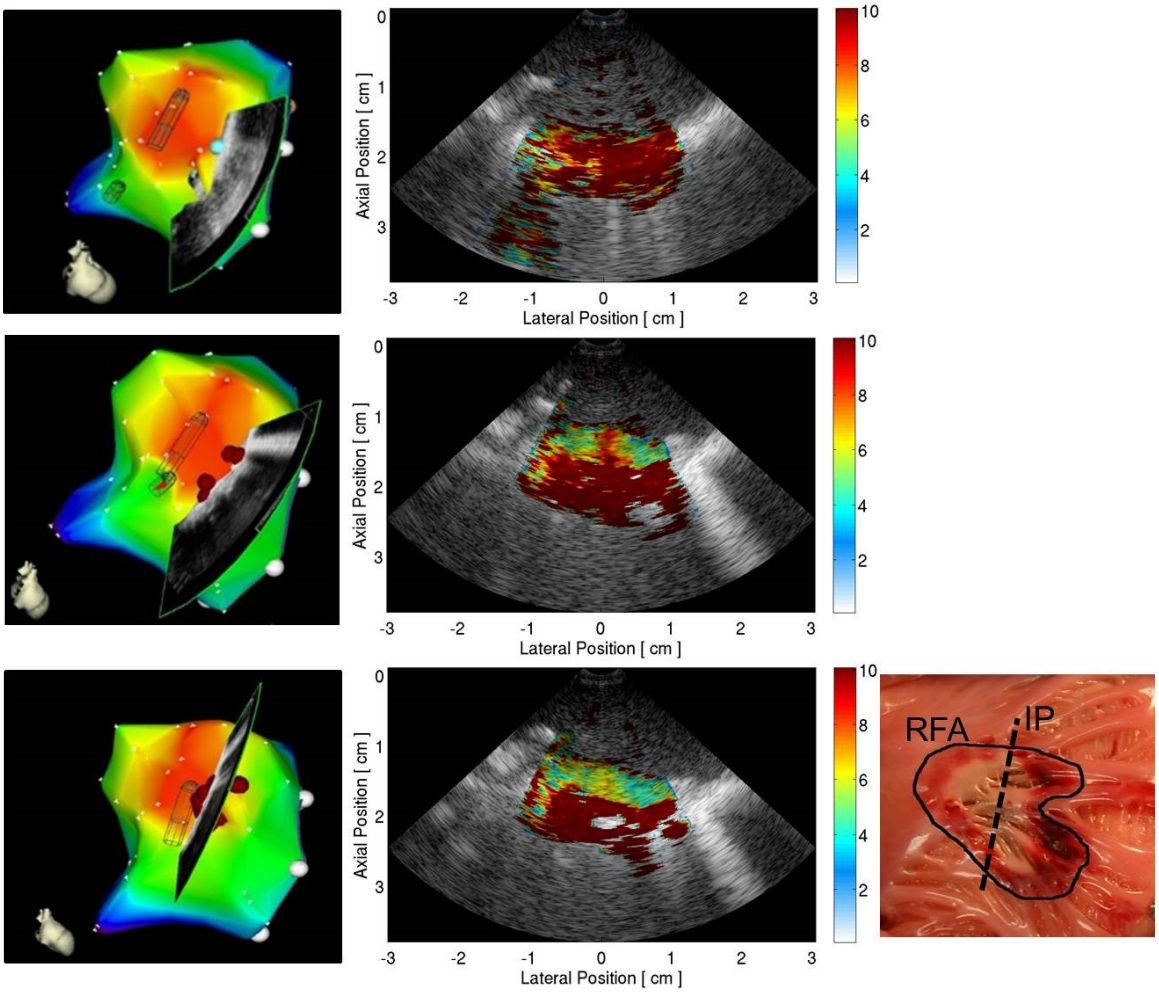

Figure 22: CARTO maps (right column) and ARFI images (center column) of a unablated gap between lesions before and after ablation. Before RFA (top row) the myocardium exhibits homogeneous ARFI-induced displacements (μm). After the delivery of two parallel RFA lines (middle row), ARFI imaging displayed a relatively soft region of unablated myocardium at the gap between the RFA lesions markers (red spheres) in the CARTO map. The relative stiffness increases when additional RFA is delivered at this gap. An image of the endocardial tissue pathology (right column) confirms a solid ablation line and the approximate imaging plane (IP) location.

4.3.2 Identification of RFA Sites with ARFI Imaging

A total of 219 ARFI images were read for the presence of lesions. Figure 23 is an example of ARFI images acquired before and after incomplete and complete linear RFA. Before RFA, the myocardium in the ARFI images exhibited relatively high ARFI-induced displacement, color coded by the red-orange spectrum of the color bar. Post ablation, the measured ARFI-induced displacements were lower in the RFA lesion (colored blue-green), indicating an increase in the tissue stiffness and the presence of lesions. The ARFI image of incomplete linear ablation confirmed an unablated gap in the lesion line. Table 7 shows the categorization of the 219 ARFI images. Reviewers of the ARFI images showed substantial agreement (kappa = 0.73) and the majority review identified RFA lesion sites with a sensitivity of 90.2% and a specificity of 94.3%. The RFA lesion width observed in the postmortem pathology photographs was typically between 4 and 8 mm.

Table 7: ARFI imaging based confirmation of RFA lesion sites in EAM (4-mm RFA marker diameter).

		ARFI Image Lesion Assessment		
		No RFA Detected	**RFA Detected**	**Total**
RFA Marker Location in EAM	**No RFA Lesion**	55	9	64
	RFA Lesion	6	149	155
	Total	61	158	219

Sensitivity = 90.2%; Specificity = 94.3%; chi-squared test $p<0.0001$

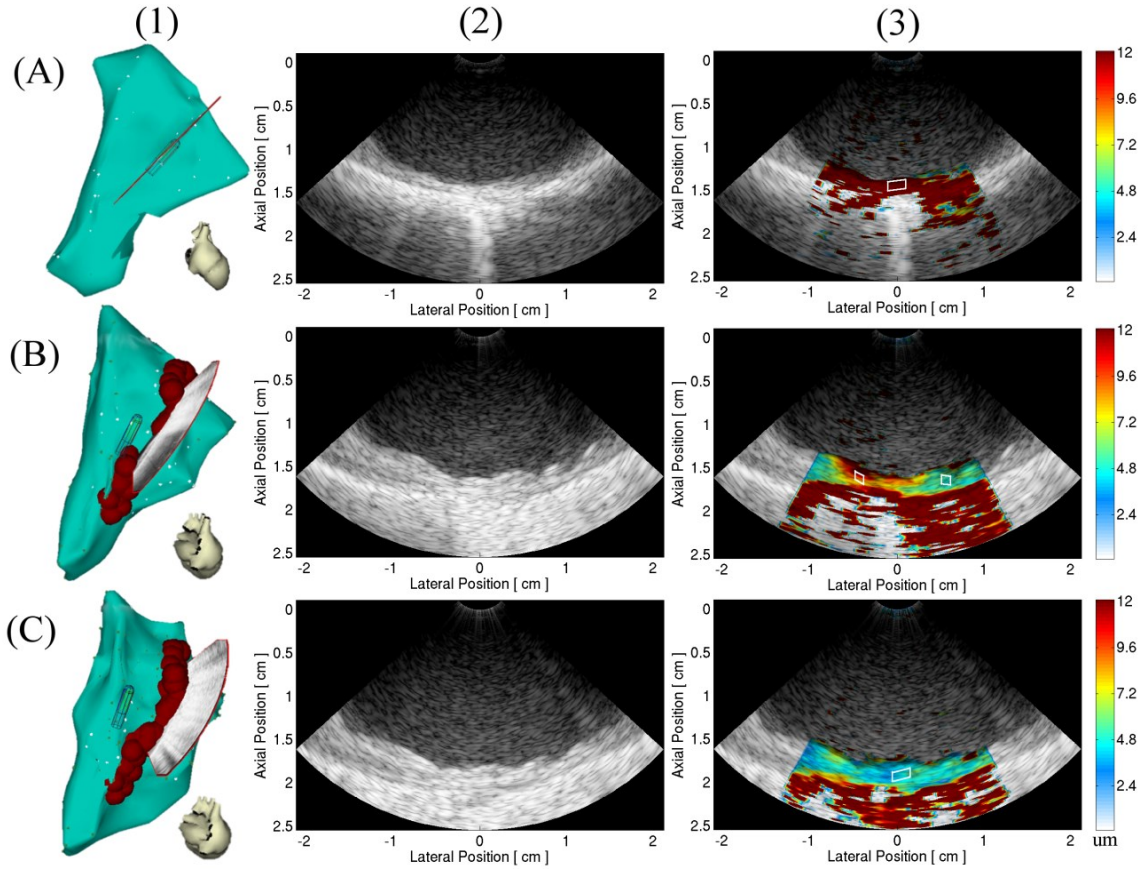

Figure 23: ARFI images before RFA (row A), after the delivery of a non-contiguous ablation line (row B), and after a complete linear ablation (row C) in a canine right atrium. The ARFI imaging plane was steered to transect the RFA lesion sites geometry (red spheres, 4-mm diameter) that are marked in the EAM (column 1). Conventional B-mode images look similar pre and post ablation. The ARFI images (column 3) exhibit low ARFI-induced displacement at the RFA ablation sites. The regions of interest for unablated and ablated myocardium are outlined in white. Color scale units are micrometers axial displacement away from the transducer.

4.3.3 Contrast of the ARFI-induced Displacements in RFA Lesion

Figure 24 plots the mean and standard deviation of the all the ARFI-induced displacement measurements in unablated and ablated canine myocardium. Table 8 summarizes the results of the statistical analysis. The mean displacement (all images, n = 219) was lower in ablated than unablated ROI (n = 143 unablated, n = 152 ablated). A repeated measures ANOVA indicated the presence of RFA lesion had a significant effect ($p = 0.0001$) on the measured displacements, whereas the canine subject did not ($p = 0.11$).

For images that contained both RFA lesion and unablated myocardium (n = 76 paired ROI images), the mean measured ARFI-induced displacement was lower for the ablated ROI. A repeated measures ANOVA determined that the presence of RFA lesion had a significant ($p = 0.0004$) effect on the measured displacement means and the canine subject did not at an alpha value of 0.01 ($p = 0.03$).

Table 8 presents the average C and CNR for the ARFI and B-mode images containing both unablated and ablated ROI. The B-mode image C and CNR were significantly lower than the ARFI image C and CNR based on a one-tailed paired t-test ($p < 0.001$). A repeated measures ANOVA determined the canine subject did not significantly affect the C and CNR for the ARFI ($p_C = 0.36$, $p_{CNR} = 0.72$) and B-mode ($p_C = 0.52$, $p_{CNR} = 0.73$) images.

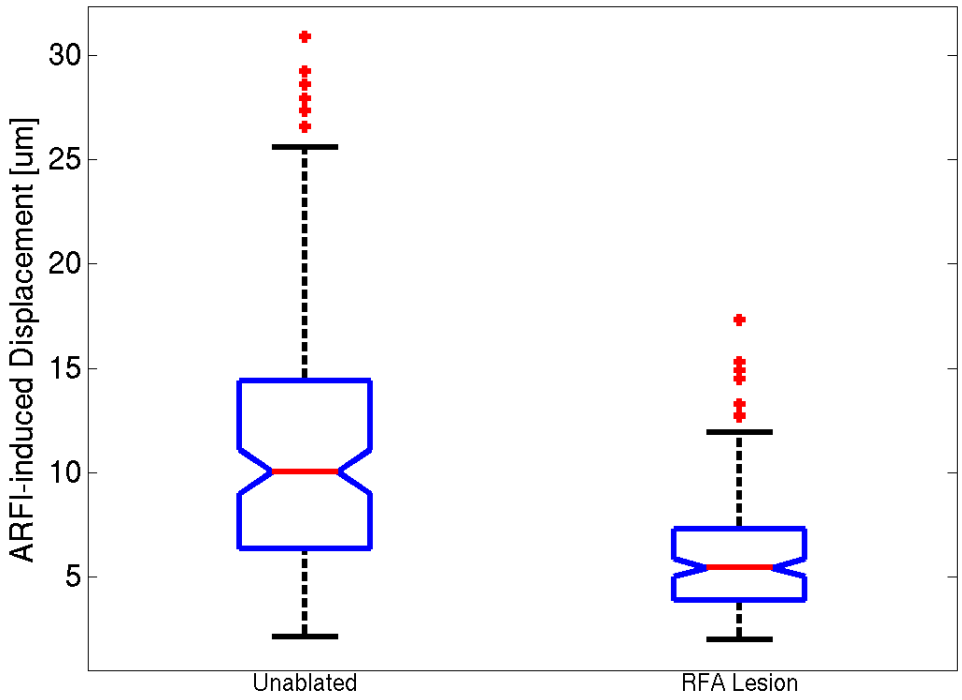

Figure 24: Boxplot of maximum ARFI-induced displacements for ROI in unablated and ablated canine myocardium (n = 219 images). The center line represents the median ARFI-induced displacement measurement. The top and bottom edges of the box (shown in blue) are the 75th and 25th percent quartiles. The top and bottom whisker edges are the extreme values (covering 99.3% of the data), and the individually plotted crosses (shown in red) are statistical outliers.

The criteria described in the methods (low CCC, unrealistic estimates) removed ARFI-induced displacement pixels from 33 ROI. Of these ROI, six had more than 5% of the pixels removed and no ROI had more than 17% of the pixels removed. No pixels were removed from the B-mode image ROI.

Table 8: Mean and standard deviations of the ARFI image ROI displacements and contrast analysis for ROI in unablated and ablated myocardium.

	Paired‡ Images		*All* Images*
	B-mode	**ARFI§**	**ARFI†**
Unablated Myocardium (μm)	-	8.31±4.30	11.23±1.71
Ablated Myocardium (μm)	-	5.11±2.36	6.06±0.94
Contrast (C)‖	-0.03±0.28	0.29±0.33	-
Contrast-to-noise ratio (CNR)‖	0.74±0.68	1.83±1.75	-

* 219 total images in 8 canine subjects

† n = 143 unablated ROI, 152 ablated ROI; repeated measures ANOVA, subject effect (p = 0.11, F = 2.61) and lesion effect (p = 0.0001, F = 47.21)

‡ 76 paired images in 8 canine subjects

§ n = 76 unablated ROI, 76 ablated ROI; repeated measures ANOVA, subject effect (p = 0.03, F = 4.67) and lesion effect (p = 0.0004, F = 31.54)

‖ repeated measures ANOVA analysis of subject effect of ARFI image C (p = 0.36, F 1.12), and CNR (p = 0.72, F = 0.64) and B-mode C (p = 0.52, F = 0.89) and CNR (p = 0.73, F = 0.63); one-tailed paired t-test for C (p = 1.15e-8) and CNR (p = 7.54e-7) between ARFI and B-mode images

4.4 Discussion and Conclusions

This chapter described the verification and use of an integrated ARFI imaging-EAM system for precise intraprocedure ARFI imaging of RFA treatment sites. A quantitative analysis showed RFA locations exhibited significantly lower maximum ARFI-induced displacements than untreated areas, and reviewers of the ARFI images identified RFA lesion sites with high sensitivity and specificity. The C and CNR indicated there was excellent contrast between the RFA lesion and unablated myocardium in the ARFI images, and the C and CNR were significantly higher in ARFI imaging than in conventional ICE images.

4.4.1 Qualitative Imaging

In this chapter, the quantitative analysis showed that ablated regions exhibit lower measured ARFI-induced displacements; however it is important to note that the measured ARFI-induced displacements are qualitative surrogates for relative tissue stiffness, and do not directly quantify a material property. Imaging the same location from a different angle, depth, or with different imaging parameters, such as frequency, focal depth, or F/# could result in different measurement ranges of ARFI-induced displacement. This study determined the range of the measurements and contrast for specific but clinically feasibly imaging conditions: the myocardium was imaged 1) in diastole, 2) within a specific focal depth range (0.5 to 2.25 cm below the transducer), 3) from a non-oblique angle (<50°), and 4) off-axis steering of the ultrasound beams was limited to ±27°. It is also important to note that negative displacement amplitudes and amplitudes above 50 μm were removed from the ROI before calculating the mean displacement; these bounds contributed to the skewed distributions and non-normal appearance of the plots in figure 24.

Despite the lack of a quantitative measure, qualitative ARFI imaging is optimally suited to image discrete targets of differing stiffness, such as ablation lesions. ARFI images have a spatial resolution that is dependent on the spatial density of the measurements. At 1.5 cm distance from the transducer, the imaging lines are 0.33 mm

apart. We believe this spatial sampling is adequate to visualize gaps greater than 0.66 mm. However, the measured gap resolution is unknown at this time and its value will be a critical factor in determining overall clinical effectiveness. Shear wave elasticity imaging (SWEI) has also been shown to be useful for quantifying the elasticity changes associated with RFA treatment.[153, 154] However, shear wave speed calculation requires a spatial kernel that can result in lower resolution; it is not yet clear if the resolution of SWEI images is adequate for the assessment of lesion line gaps.

The contrast analysis presented in this chapter demonstrated that the relative contrast in a single ARFI image can differentiate RFA lesion from non-lesion. This ability could provide a useful tool for TCA procedure guidance, where exact quantification of the tissue properties is not necessary.

Due to the qualitative nature of the image, the development of a method to automatically detect RFA lesion based on the value of the measured ARFI-induced displacements would require further investigation. In the previous chapter, a pre-ablation image was used to normalize the relative displacements. While this exact technique is not translatable to single intraprocedure images acquired during TCA, the development of a spatial normalization algorithm to compensate for the acoustic energy attenuation through depth and at extreme steering angles could increase the likelihood of developing an effective automatic segmentation method.

4.4.2 Considerations for Clinical Translation

As previously mentioned, diastolic imaging is necessary for successful ARFI imaging of lesions as most of the contrast between lesion and normal tissue disappears when the tissue stiffens during systole.[95, 96, 133, 155] Also, late diastole is the time of least intrinsic motion during the cardiac cycle. We manually set the post QRS delay to start the imaging in late diastole; however, this delay had to be adjusted multiple times throughout the study to account for changes in heart rate. Two of the false-positive images (ARFI image reader detected lesion, no marker in EAM) were acquired before the RFA delivery phase of the experiment, and may have indicated low ARFI-induced displacement due to a poor gating delay. Mistiming the acquisition due to intermittent variations in heart rate may have also contributed to the high number of images with motion artifacts. The development of a software tool to adjust the gating delay in real-time could potentially reduce the instances of motion artifacts. Shortening the acquisition time of the imaging sequence could also help reduce the physiological motion during the acquisition.

Imaging the myocardium with the transducer face parallel to the endocardium and at the center of the focal DOF provided the highest contrast ARFI images. Using these criteria, we were able to acquire a substantial number of high-quality ARFI images in the canine RA. The restricted DOF made imaging some areas of the canine heart

challenging, and may limit the number of sites that can be imaged with contemporary ICE catheters during a clinical TCA procedures. Significant technical advances to address these limitations, such as the development of an ARFI imaging optimized transducer or more flexible ICE catheter steering technology, would improve the likelihood of clinical translation.

ARFI images require multiple ultrasound scan-lines at each ARFI-excitation location to monitor the tissue deformation and therefore cannot be acquired at the same high frame rate as B-mode. This, combined with need for diastolic imaging means that continuous display ARFI imaging for lesion evaluation is not possible. Accelerated ARFI imaging could allow the acquisition of multiple frames in a single beat, but any increase in the ARFI imaging acquisition rates must consider the effects of increased acoustic exposure (mechanical index/transducer face heating). With this in mind, the development of 3-D ARFI imaging could reduce the number of acquisitions needed to interrogate a lesion line.

Due to the restricted DOF, ARFI imaging lesion evaluation in the left atrium (LA) would require a double transseptal puncture to position the ICE catheter across the atrial septum. While ICE imaging in the LA is not mandatory for TCA procedures, it is a safe and effective method used by many electrophysiologists to monitor RF-delivery and the ablation catheter contact in real-time. In this study, ARFI images were acquired in

the canine RA to avoid performing a double transseptal puncture; transseptal punctures are difficult in the smaller canine heart. While these results were obtained in the RA, it is expected that similar results would be found in the LA.

4.4.3 Considerations for EAM Guided ARFI Imaging

The experiment described in this chapter determined EAM was an indispensable tool for mapping RFA treatment sites and guiding the imaging plane. The RFA markers in EAM were treated as the gold-standard for indicating lesion locations. The experiment was designed this way because attempting to match the exact orientation and location of each imaging plane to the *ex vivo* pathology would risk substantial misregistration errors that would affect the accuracy of the lesion evaluations. A concern when using EAM as the gold-standard was that the RFA markers themselves only indirectly inferred RFA delivery; the EAM marker did not directly indicate the presence or size of an actual lesion. Discrepancies between the actual pathological lesion configuration and the electroanatomical map could have resulted in the incorrect classification (ablated vs. unablated) of some ROI in the ARFI images. These misclassifications likely affected the statistical analysis and the C and CNR calculations. For example, the six false-negative sites in table 7 could have been sites where the RF-energy did not induce a high enough temperature for ablation despite the location marker or the lesion could have been very small (<4 mm) due to poor electrode-

endocardium contact. At six of the nine false-positive sites, the imaging plane was positioned within ~4 mm of a lesion marker. One of the eight was within ~8 mm. In these cases, the pre-determined marker diameter of 4 mm in the EAM could have contributed to the misclassifications. In the pathology examination, several lesions were substantially larger (> 8 mm) than the EAM marker diameter. Despite this potential for misclassification, expert reviews of the ARFI images were very highly correlated with the presence of the RFA markers in the EAM.

4.4.4 Study Limitations

It is important to note that the displacement ranges, C, and CNR were calculated from the maximum ARFI-induced displacement measurements within 0.6 ms of the ARFI-excitation. An examination of these parameters at different time points after the ARFI-excitation could potentially result in different values for measured displacement.[114, 156-158] Also, the ~0.60 ms post tracking time may not have captured the peak displacement in some locations. An optimization of ICE-based ARFI sequences would have to balance any increase in tracking time with overall lengthening of the sequence. Lengthening the sequence increases the effects of bulk tissue motion during the acquisition and would change the safety parameters affected by increased acoustic exposure.

ARFI imaging of lesion borders can result in shear wave (off-axis mechanical wave propagation) reflections from lesion-tissue boundaries.[25, 158, 159] The potential effect of such interactions on the contrast for thin (1–3 mm) inhomogeneous viscoelastic atrial tissue with irregular ablation lesion borders are beyond the scope of this thesis.

In this study, the maximum ARFI-induced displacement was not compared for the same exact sites before and after ablation. Therefore, stiffness inhomogeneity in the atrial tissue could be mistaken for RFA lesion in the ARFI images. Despite this possibility, in the healthy canine heart it is expected that such inhomogeneities would be minimal.

4.5 Acknowledgements

For their contributions to this work, I acknowledge Dr. Stephen Hsu, Dr. Mark Palmeri, Dr. Veronica Rotemberg, Peter Hollender, Joshua Hirsch, Brittany Potter, Matt Brown, and Ellen Dixon-Tulloch.

Chapter 5: Correlation of Electrical Substrate Modification and RFA-Induced Stiffness Changes in ARFI Imaging

The work described in this chapter was published in the following manuscript:

Eyerly SA, Bahnson TD, Koontz JI, Bradway DP, Dumont DM, Trahey GE, Wolf PD. Intracardiac Acoustic Radiation Force Impulse Imaging: A Novel Imaging Method for Intraprocedural Evaluation of Radiofrequency Ablation Lesions. Heart Rhythm. 2012. Vol. 9, 11:1855-1862.

5.1 Introduction

The aim of the previous chapter was to verify the use of an integrated ARFI and EAM imaging system for intraprocedure imaging of RFA lesions using ARFI imaging. Reviewer successfully identified RFA lesion locations in EAM based on the relative stiffness contrast between the lesion and unablated myocardium. While evaluation of the location and extent of the tissue damage is important, to be a clinically relevant method for lesion evaluation during TCA the presence of lesions in the ARFI images must also correlate with the electrical substrate modification, particularly electrical block at the ablation site.

The ARFI images from the animal experiment described in the last chapter were used to determine if ARFI-based lesion assessments accurately identified areas of

conduction disturbance and electrical block. It is hypothesized that ARFI image locations that contain no RFA lesion or non-contiguous lesion will show electrical conduction in the EAM local activation time (LAT) map, while locations showing transmural, contiguous lesion will exhibit conduction block in the LAT map.

The chapter is organized as follows: Section 5.2 describes the *in vivo* ARFI imaging and conduction mapping protocol as well as the evaluation methods used for the LAT maps and ARFI images. Section 5.3 describes the correlation of the ARFI imaging and LAT map evaluations, and section 5.4 discusses considerations and the potential importance of the results for clinical translation.

5.2 Methods

5.2.1 ARFI Imaging Protocol and Experimental Setup

The full equipment setup (including the ARFI imaging-EAM integration) and ARFI imaging procedure used for this study were described in chapter 4. The ARFI imaging sequences were also identical to those presented in the previous chapter. Refer to chapter 4 for specific details regarding the ARFI imaging protocol.

5.2.2 Animal Experimental Protocol

The animal experimental protocol described in this chapter was conducted on the same animal subjects as described in chapter 4.

In each canine subject, a baseline point-by-point geometry and LAT map was made of the RA with the Navistar mapping catheter and CARTO XP navigation system (Biosense Webster; Diamond Bar, CA). A pre-RFA guideline of points delineating the intended ablation sites was drawn on the CARTO LAT map; baseline ARFI images were acquired along this guideline. The ICE fan position and orientation for each ARFI imaging location was saved for post-procedure review. Discrete RFA lesions were delivered along the guideline in two stages. The first stage left an intentional ~1 cm gap, and the gap was closed in the second stage.

After each stage, a new LAT map was constructed and the ablation line was ARFI imaged. See figure 34 in appendix A for examples of LAT maps and RFA site markers for a canine RA before RFA, after the incomplete linear RFA, and after complete linear ablation with confirmed full conduction block.

At the end of the study, the animal was euthanized and the heart was removed to confirm lesion delivery. The RFA lesions were photographed with a digital camera.

5.2.3 Local Activation Time Map Evaluation

Screenshots of each imaging fan position were compiled with the LAT map using the CARTOSound Module in the system Review Mode. The tricuspid annulus (TA) was cut from the map, and internal points were removed. The ablation (red spheres) and

guideline markers were hidden, and the color scale of each LAT map was adjusted to increase the color gradient at the ablation line.

The LAT maps for each ARFI image location were randomized and read by three different reviewers who were blinded to the ARFI images, the stage of ablation, and canine subject.

The reviewers (two clinical electrophysiologists, one electrophysiology expert) were posed three yes or no questions about each LAT map in reference to the baseline map: 1) "*Is there conduction block anywhere on this LAT map?"* (additional possible answer of "Cannot be determined"), 2) "*Based on the activation pattern in the LAT map, does there appear to be RF lesions present at the ICE imaging fan location?"*, and 3) "*Is the ICE imaging plane completely parallel to and transecting a line of block, thereby imaging a continuous line of lesion?"*. The RFA lesion widths observed in the postmortem pathology photographs were typically between 4 and 8 mm; therefore, questions #2 and #3 were answered considering the imaging plane could be transecting RFA lesions within ~8 mm of conduction block. The majority (at least 2 of 3 reviewers) responses to the questions determined the final evaluations.

5.2.4 ARFI Image Evaluation

The ARFI images were randomized and read by three different reviewers who were blinded to the CARTO maps, stage of ablation, and canine subject.

The reviewers (all experienced in ARFI imaging) were instructed to classify the ARFI images into one of three categories: 1) *no lesion*, defined as the ARFI image depicts no visible area of low relative displacement in the myocardium, 2) *non-contiguous lesion*, depicts at least one area of low relative displacement that does not extend the entire length or depth of the imaged myocardium, or 3) *contiguous lesion*, the full extent of the imaged myocardium depicts low relative displacement. The majority (at least 2 of 3 reviewers) review determined the final image classification.

5.2.5 Statistical Analysis of Evaluations

The degree of the agreement within the sets of three reviewers was quantified with the kappa statistic.[160] Image pairs where the LAT map evaluation had no majority review or the majority review misidentified the correct stage of ablation (question #1, pre vs. post RFA) were also removed from the analysis.

The majority ARFI image categorization and LAT map assessment from question #2 were used to compile a 2x2 contingency table of all image pairs to summarize the ability of ARFI imaging to identify RFA induced conduction disturbances. For the ARFI images, the category "lesion" included the non-contiguous and continuous classifications. A second 2x2 contingency table was compiled to summarize the ability of ARFI imaging to identify conductive lesion line discontinuities and conduction block using the LAT map evaluations from questions #2 and #3. This table only included post-

ablation image pairs with a yes response to LAT map assessment question #2. The sensitivity, specificity, positive predictive value (PPV), and negative predictive value (NPV) were calculated for both tables. Heterogeneity analysis was performed to justify pooling the data for all animals. A heterogeneity chi-square statistic was calculated to confirm that the data from different animals came from a homogeneous population.[20]

5.3 Results

In eight canine subjects, 243 ARFI images were acquired with the outlined imaging conditions (see section 4.2.2). Twenty-eight images were rejected due to motion artifacts; the remaining 219 ARFI image-LAT map pairs (54 pre-ablation, 80 after incomplete ablation, and 85 after gap closure) were reviewed for statistical analysis.

The kappa coefficient for the ARFI image assessments indicated substantial agreement ($\kappa = 0.73$) between the three reviewers. The individual kappa coefficients for the LAT map review questions showed substantial agreement for identifying lesions at the imaging plane ($\kappa = 0.68$), and moderate agreement when assessing full conduction block at the imaging plane ($\kappa = 0.43$). The LAT map reviewers had different question responses (no majority review) for 15 image pairs. The majority review misidentified the correct stage of ablation in five LAT maps. These 20 image pairs we excluded from the final analysis.

The statistical calculations included 199 image pairs. The reviews for detecting RFA treatment with ARFI imaging compared to the reviews for identifying conduction disturbance in the LAT map is shown in table 9. Table 10 shows the ARFI image reviews for RFA lesion contiguity vs. functional conduction block (n = 140, includes only post ablation image pairs confirmed by the LAT map review). The heterogeneity analysis justified pooling the data from all the animal subjects. Table 11 summarizes the heterogeneity chi-square and p-value, sensitivity, specificity, PPV, and NPV for tables 9 and 10.

An image pair example from each ablation stage is shown in figure 25. Before RFA (figure 25C-1), the ARFI-induced displacements within the myocardium were relatively high and homogeneous. Figure 25C-2 shows the unablated gap in the lesion line, visible as the area of high tissue displacement surrounded by areas of relatively low tissue displacement. The final ARFI image (figure 25C-3) shows a homogeneous region of low displacement, confirming complete ablation of the gap.

Table 9: ARFI image assessment for RFA treatment.

	LAT map assessment at imaging fan location		
ARFI image lesion assessment	**No conduction disturbance**	**Conduction disturbance inferring the presence of lesions**	**Total**
No RFA Lesion	54	6	60
RFA Lesion	5	134	139
Total	59	140	199

Table 10: ARFI image assessment for contiguous RFA.

	LAT map assessment at imaging fan location		
ARFI image lesion assessment	**No block**	**Block**	**Total**
Noncontiguous lesion	67	27	94
Contiguous lesion	22	24	46
Total	89	51	140

Table 11: Summary of statistical analysis for tables 9 and 10.

	RFA treatment	**Contiguous RFA**
n	199	140
Heterogeneity, χ^2	4.59	9.29
Heterogeneity, p value*	0.7099	0.2325
Sensitivity (%)	95.7	47.1
Specificity (%)	91.5	75.3
PPV (%)	96.4	52.2
NPV (%)	90.0	71.2

*Heterogeneity analysis: degrees of freedom = 7, do not reject Ho (8 samples from homogeneous population

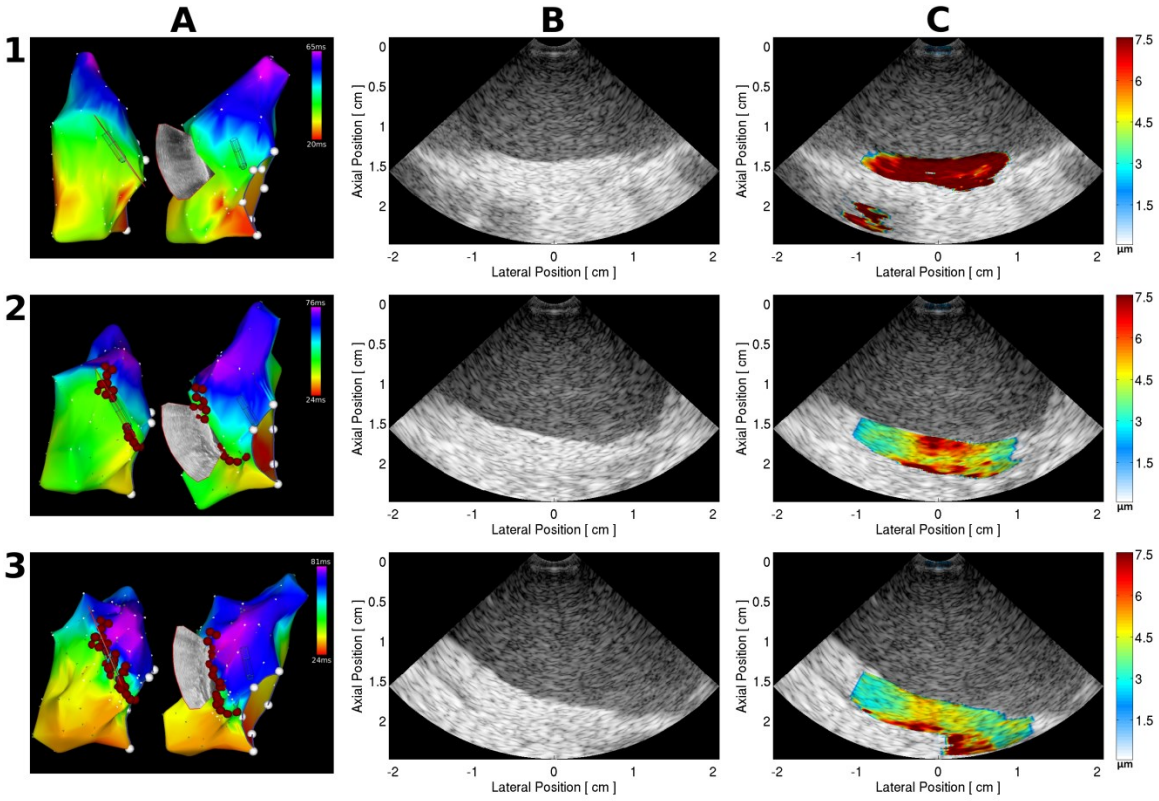

Figure 25: An example of three ARFI image-LAT map pairs. Row 1) acquired before RFA, row 2) acquired after intentionally creating a 1 cm conductive gap, and row 3) acquired after closure of the 1 cm gap. Column A) LAT maps showing the imaging fan position in the canine RA and the location of delivered RFA lesions (red spherical markers). Column B) conventional B-mode images acquired at the location indicated on the LAT maps. There is no lesion visible in the B-mode images. Column C) Maximum ARFI-induced displacement images. The color bar units are microns of tissue displacement away from the transducer. RFA lesions sites are visible as regions of lower relative displacement (stiffer tissue), represented by the blue-green-yellow portion of the color bar.

5.4 Discussion and Conclusions

The results of the study described in this chapter confirmed ARFI images predicted RFA-induced conduction disturbances at the imaging site on the LAT maps. Reviewers of the ARFI images identified RFA treated areas with high sensitivity, specificity, and predictive values. Reviewers also distinguished gaps between adjacent RFA lesions that frequently corresponded to conduction "breakthrough" on the activation map. In many cases, ARFI images reviewed as contiguous RFA displayed conduction block on the activation map.

5.4.1 Clinical Translation and Implications

Lesion evaluation with an ARFI imaging-EAM system could guide the delivery of consolidating RFA to conductive lesion line discontinuities, and subsequently decrease the total procedure time and increase the success rate of procedures that use linear ablation strategies. An ARFI imaging-EAM system uses existing clinical tools and techniques, therefore clinicians would not need to purchase and install expensive new equipment in the operating rooms and electrophysiologists would not need significant training to use the system.

5.4.1.1 Distinguishing Conductive from Non-Conductive Unablated Gaps

Cardio-myocytes near sites of RFA delivery can be reversibly stunned (see section 2.2.2), and areas of conduction block observed acutely after circumferential or

antral PVI have shown conduction recovery in some patients.[21-23] The lower sensitivity and discordance between the activation defined completeness of conduction block and the ARFI imaging defined lesion contiguity could potentially be explained by the indirect functional vs. direct imaging method of assessing block. Further investigation will be required to test if imaging tissue stiffness is a more sensitive measure of ablation lesion durability and long-term ablation success than acute activation mapping.

5.4.2 Study Limitations

EAM is the current end procedure gold-standard for assessing ablation line completeness, therefore this study used EAM to identify regions of conduction disturbance or block. Unfortunately, the accuracy of the LAT maps was largely dependent on the mapping catheter stability and EG acquisition density. For example, figure 26C shows an RFA line that was incompletely anchored at the TA. LAT conduction mapping at the annulus was sparse due to the difficulty of achieving stable catheter contact at the annulus. In this case, it was challenging to verify or deny an anchored lesion line from the LAT map. The ARFI image (figure 26A) conclusively visualizes an unablated region at the TA that likely corresponds to the unanchored gap. Adding differential pacing to the methods may have improved the accuracy of these ambiguous EAM maps, but this was difficult to achieve in the small canine RA and was not performed in this study.

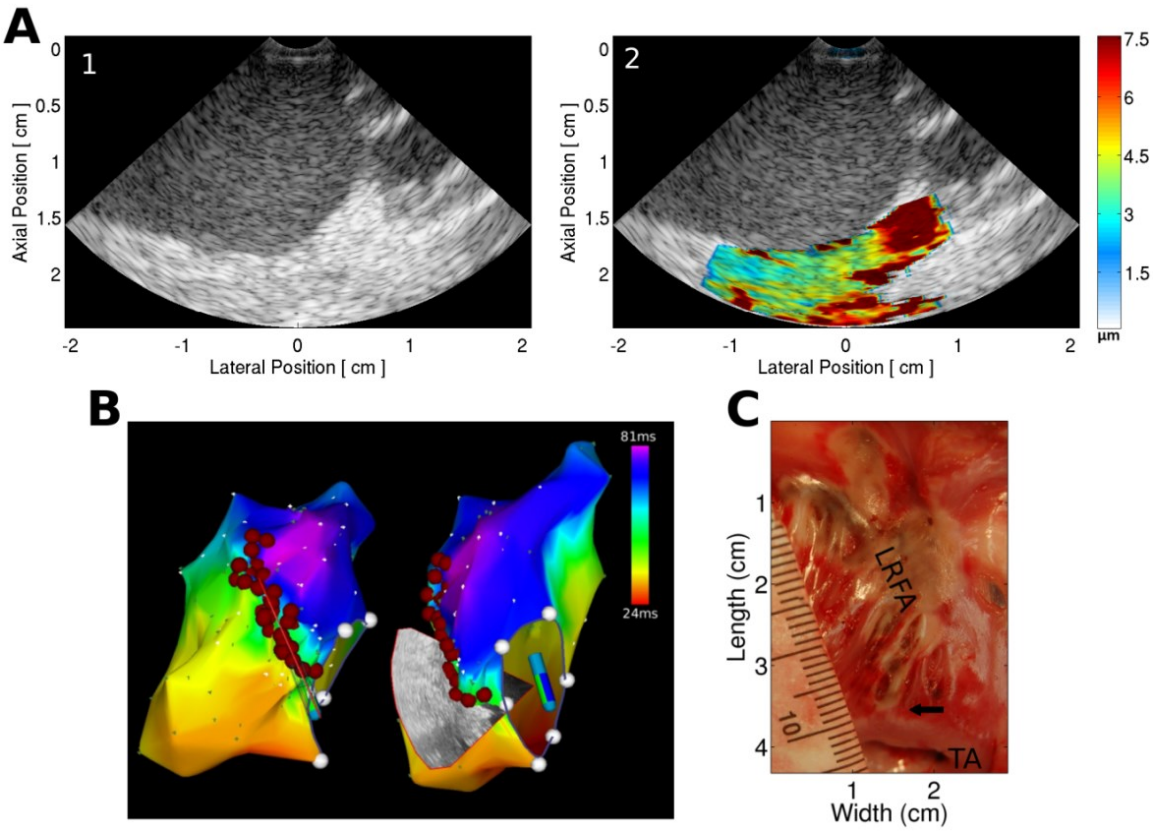

Figure 26: Conventional (1) B-mode and (2) ARFI image at the tricuspid annulus. The ARFI image shows an area of relatively high displacements at the annulus indicating a likely unablated region. ARFI image color bar units are microns displacement away from the transducer. B) LAT map surrounding a line of RFA lesions in the right atrium, red spheres indicate RFA delivery sites C) Pathology photograph of the RA endocardial surface confirming continuous line of RFA lesions (LRFA). A small unablated gap is visible at the tricuspid annulus (TA), indicated by the black arrow.

Assessing if the 2-D ARFI imaging plane was parallel and completely transecting a line of conduction block on the LAT map was challenging; the difficulty was reflected in the moderate inter-reviewer agreement. LAT maps could not provide information about lesion line thickness or irregular lesion morphology if the catheter drifted, making it difficult to predict the exact extent of RFA treatment based on the functional conduction map alone. Misalignment of the 2-D imaging plane through complete RFA lines could be responsible for the low sensitivity (non-contiguous lesion in ARFI image, conduction block in LAT) when detecting conduction block. Such misalignments and the corresponding alignment interpretation from the LAT maps were likely a primary source of discrepancy between the ARFI imaging and EAM lesion assessments.

5.5 Acknowledgements

For their contributions to this work, I acknowledge Dr. Stephen Hsu, Dr. Mark Palmeri, Dr. Veronica Rotemberg, Peter Hollender, Joshua Hirsch, Brittany Potter, Matt Brown, and Ellen Dixon-Tulloch.

Chapter 6: ARFI Imaging of RFA Lesions in Human Patients during Clinical TCA

6.1 Introduction

The pre-clinical work described in the previous chapters proved ARFI imaging can visualize the relative stiffness difference between untreated myocardium and RFA lesion *in vivo*. Also, EAM guided intracardiac ARFI imaging successfully identified RF-delivery locations and conduction disturbances at the imaging site. Based on these findings, a pilot clinical study was undertaken to investigate the feasibility of intraprocedure RFA lesion evaluation with ARFI imaging in human patients.

The following chapter presents images and results from the first human patients imaged with intracardiac ARFI imaging. In six clinical patients undergoing TCA for AF, intraprocedure ICE-based ARFI images were acquired at a target ablation site before and after RFA to observe any relative stiffness change in the myocardium.

The chapter is organized as follows: section 6.2 describes the clinical software imaging tool developed for the ultrasound scanner and the imaging protocol for the clinical patients. Section 6.3 presents images and observations from the patients, and

section 6.4 discusses the technical and procedural successes and challenges encountered during this initial clinical experience.

6.2 Methods

6.2.1 Clinical Tool for ARFI Imaging

A custom software tool was developed at Siemens Healthcare (Issaquah, WA) for the S2000™ ultrasound scanner and either a 10 or 8 French AcuNav™ catheter transducer (Biosense Webster). The tool provided an imaging platform within the scanner software that allowed the fast acquisition and display of co-registered ICE and ARFI images during clinical TCA procedures. The clinical tool also transitioned quickly between live ICE imaging as needed for the clinical procedure and ARFI imaging mode.

The tool allowed the real-time selection of the ARFI imaging focal depth, imaging fan FOV (degrees), and fan imaging direction and depth (within the ICE image) using the scanner panel controls. An ARFI image was acquired with a single button-press and was displayed overlaid onto the ICE image or in a split screen mode within the scanner software. A screen shot of the ARFI imaging display is shown in figure 27. The dynamic range of the ARFI induced displacements could be adjusted in the display using the control panel. A mandatory 3 second "cool-down" time was built into the imaging platform to prevent rapid ARFI image acquisitions that could cause excessive acoustic exposure or transducer heating.

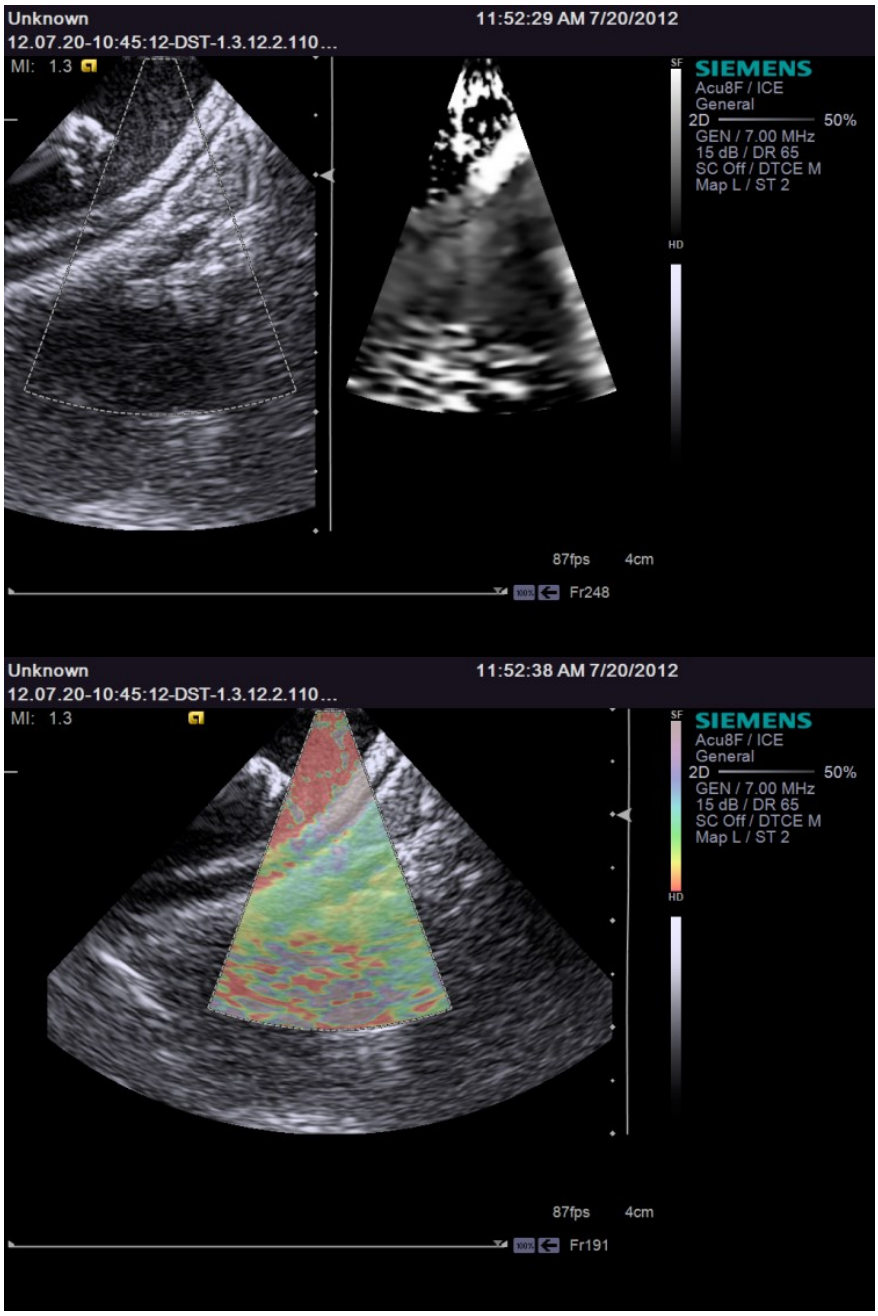

Figure 27: Screen shots of the clinical ARFI imaging tool software. The ARFI imaging focal depth, field of view, and fan steering angle were user selected using the scanner control panel. The ARFI image was displayed within seconds of the acquisition in split screen mode (top) or color overlay mode (bottom).

Table 12: ARFI imaging parameters for S2000 clinical studies.

Transducer	Probe	AcuNav™ (10 or 8 French)
	Elements	64
	Array Type	Phased
	Center Frequency [MHz]	6.15
Scanner	Model (Siemens)	S2000™ (ACUSON)
	Data Type	IQ
B-mode and ARFI Imaging Parameters	Transmit Frequency [MHz]	6.15
	Tracking Frequency [MHz]	6.15
	Sampling Frequency [MHz]	40
	Focus	1.0 – 2.5 cm
	F/#	1.43 – 3.57
	Cycles	300
	ARFI push length [μs]	55
	ARFI lateral push locations	42 (20 – 90°)
	Parallel tracking	2:1
	Pre-tracks	4
	Post tracks	8 – 15
	PRF [kHz]	9.67

The patient ECG was monitored by an external defibrillator (LifePak 12, Medtronic; Minneapolis, MN) during the procedure and relayed to the scanner through a custom physio cable (see section 4.2.1.3). All ARFI images were gated to diastole by manually selecting an estimated QRS delay; the delay was determined by observing several seconds of m-mode at the imaging location and measuring the time from the QRS to diastole (least intrinsic motion).

The ranges and fixed parameters for the clinical ARFI imaging tool are presented in table 12. The safety analysis confirmed the sequences were within the FDA limits for MI (< 1.7) and transducer surface heating (<4.0°C).[150]

6.2.2 ARFI Image Processing

The raw IQ data was saved for each ARFI image acquisition, and the full image processing was completed offline after the procedure. The measured ARFI-induced displacements were calculated from the raw IQ data using a phase-shift estimation algorithm (Loups, axial kernel = 1.5λ).[124] Poor displacement estimations with low CXCC (median through the tracking time was less than 0.90) were removed from the image.[117] Displacement estimations larger than 50 μm were also removed from the image.

No priming pulses were applied during the acquisition sequence. The measured displacement profiles were motion filtered using a quadratic function interpolated between the pre-excitation locations and the four latest post-excitation displacement measurements. [130] An example of a single pixel displacement profile from unablated myocardium and the resulting motion filter and filtered profile is shown in figure 28.

After the application of the motion filter, the maximum displacement was found for each pixel location. The data was then median filtered (2.25 mm lateral by 0.462 mm axial) and scan converted, and the final image was overlaid onto the B-mode image.

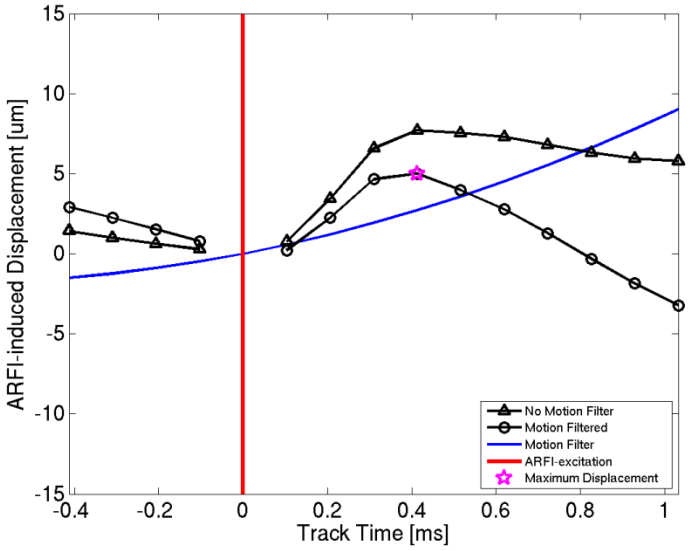

Figure 28: ARFI-induced displacement curve for a single pixel location in unablated myocardium. In the clinical ARFI imaging sequences, no priming pulses were transmitted. The raw displacements (triangles) were motion filtered using a quadratic motion function (blue) interpolated from the pre-track points and the last four post-track points. This function was subtracted from the raw displacement to recover the ARFI-induced displacement profile (circles). Ten scan-lines were collected to monitor the post-excitation tissue displacement. Total tracking time for a single line was ~1.5 ms. The maximum displacement through time was the pixel value in the 2-D ARFI image.

6.2.3 Clinical Imaging Procedure

Clinical patients undergoing catheter ablation for clinically diagnosed drug-refractory AF were considered eligible for study enrollment. All patients provided informed consent, and the research protocol was approved by the Duke University Institutional Review Board (IRB) for clinical research.

Real-time ICE imaging was used to guide a double transseptal puncture for LA access. Two steerable catheter sheaths were positioned through the atrial septum to guide the ablation and ICE catheters into the LA. During the ablation procedure, the ultrasound transducer tip was positioned within 2.5 cm of a targeted endocardial RFA sites and as parallel to the ICE array as possible (0 – 40°). These bounds maximized acoustic energy to the tissue and minimized any depth dependent energy attenuation. A diastolic-gated ARFI image was acquired in NSR before RFA, and three images were acquired within several minutes of RF-delivery at the target site. The ablation catheter was removed from the ARFI imaging FOV during image acquisitions; a screenshot was taken of the live ICE image during the ablation to verify the ablation catheter contact (ACC) site and RF-delivery location. Images successfully ECG-gated to diastole and acquired within transducer positioning bounds were read and analyzed for RFA lesions.

Standard continuous 2-D ICE imaging was available to the clinical operator at all times during the procedure when ARFI images were not being acquired. ARFI imaging added no more than 5–10 minutes to the TCA procedure, and the ARFI images were not used to guide ablation during the procedure.

6.2.4 Statistical Analysis

The mean ARFI-induced displacement (no spatial median filtering) was calculated for a 1x1 mm region of interest (ROI) below the ACC site in the pre-ablation

image and the three sequential post ablation images. The ROI locations were manually selected using the co-registered B-mode image and ACC snapshot to approximate the RFA lesion location; the manual selection of the ROI was blinded to the ARFI image to prevent biased selection of the RFA location.

The mean, standard deviation, and coefficient of variation (standard deviation divided by mean) were calculated for the ARFI-induced displacement ROI in the three post ablation images. The percent decrease in displacement at the ablation site was calculated by dividing the mean displacement in the pre-ablation ROI by the average of the mean (n = 3) displacement for the post ablation ROI.

6.3 Results

ARFI images were acquired with the S2000 ARFI imaging tool in six patients with drug-refractory AF. ARFI images were successfully acquired of several anatomical structures targeted for ablation, including the LA roofline, posterior wall, and ligament of Marshall (LoM). There were no acute peri-procedural complications in the study patients (stroke, pericardial effusion, and pericardial tamponade). All patients were in NSR at the conclusion of the procedure.

Figure 29 shows the progression of a LA roofline ablation. As the RFA line is created, the ARFI-induced displacements become relatively low (blue) at the ACC site. Figure 30 shows three images of RFA treatment at the LA posterior wall. The RFA

lesion is visible as the area of low ARFI-induced displacement, and the displacement measurements are repeatable across the three acquisitions. Figure 31 presents ARFI images taken before and after a 60 second RF-delivery on the top of the LoM. There was an observable increase in the myocardial stiffness at the RFA site, but this image suggested complete transmural ablation of the LoM was not achieved.

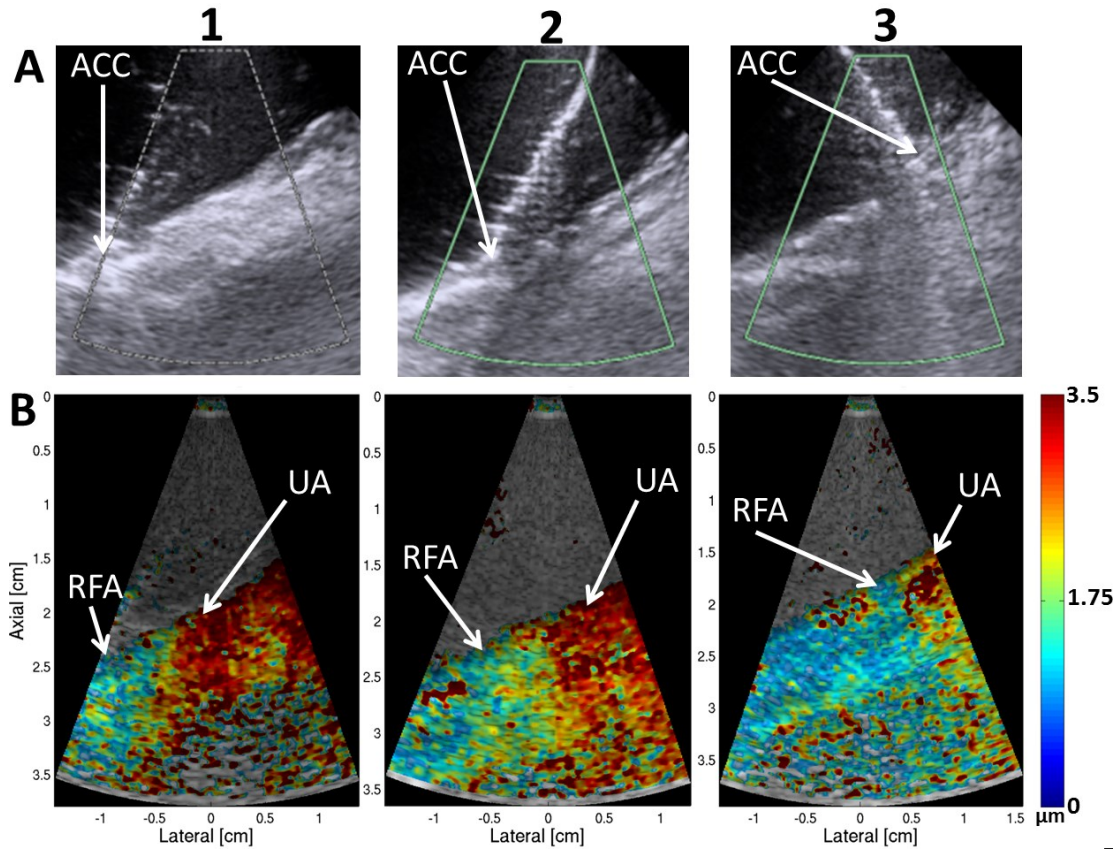

Figure 29: ARFI images of sequential RF ablations along the LA roof. Two-dimensional ICE images of the ablation catheter contact (ACC, row A) and corresponding ARFI images of the transmural RFA lesions (RFA, row B) show there is an increase in the myocardium stiffness immediately following 60 second ablation of the unablated (UA) myocardium.

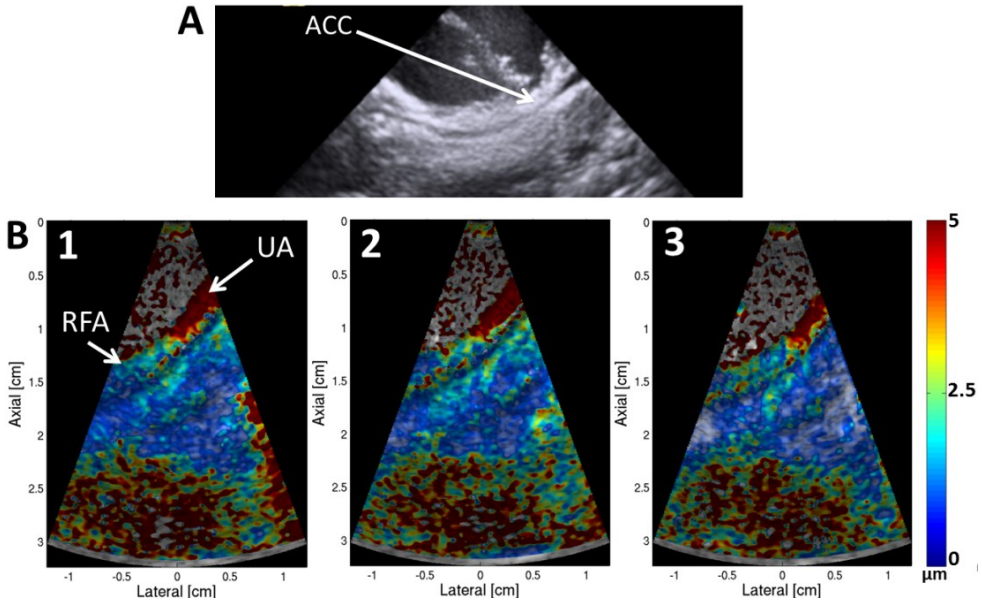

Figure 30: ARFI images of RFA at the posterior left pulmonary vein antrum. The RFA lesion (RFA) displacements in the ARFI images (row B) exhibited relatively high stiffness at the ablation catheter contact (ACC) point in the ICE image (row A) after a 60 second ablation as compared to the unablated (UA) myocardium. The AFRI images were acquired immediately following RFA (B1) and 12 seconds (B2) and 19 seconds (B3) after the initial image.

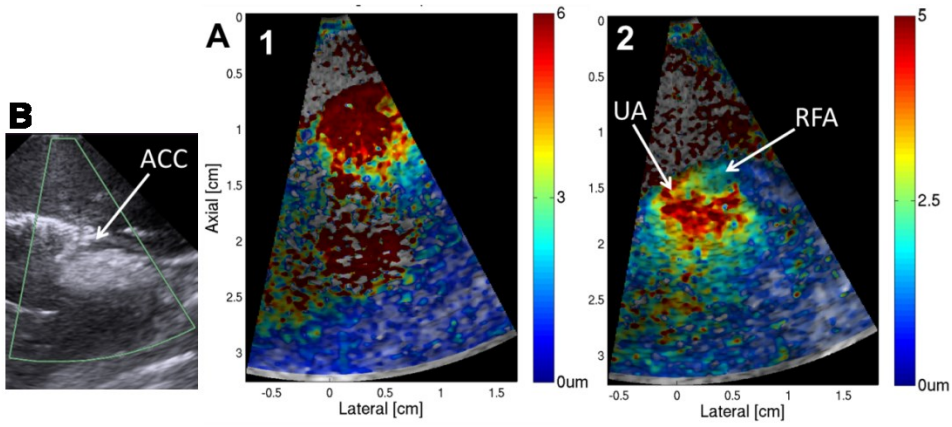

Figure 31: ARFI images of RFA at ligament of Marshall (LoM). There is a decrease in the ARFI-induced displacement at the ablation catheter contact (ACC) site shown in the live ICE image (B) after a 60 second ablation. The unablated (UA) myocardium to the left and below the lesion suggests transmurality was not achieved.

Table 13: Statistical summary of measured ARFI-induced displacements in a 1x1 mm region of myocardium below the ACC point before and after RFA.

Pair	Imaging Location (left atrium)	Pre-RFA Mean Displacement (μm)	Post RFA Mean Displacement (μm)	Post RFA Coefficient of Variation	Percent Decrease (%)
1	Roofline	2.86	2.19±1.00	0.46	23.58±34.85
2	Roofline	3.22	2.53±0.88	0.35	21.28±27.39
3	Posterior	5.07	1.95±0.42	0.21	50.68±16.72
4	LoM	10.36	3.67±0.60	0.16	64.51±5.81
5	LoM	11.94	2.26±0.23	0.10	81.11±1.94
6	LoM	4.52	2.73±0.20	0.07	39.58±4.40
Mean		**6.33±3.58**	**2.56±0.61**	**0.23±0.15**	**46.79±23.45**

In four patients, six RFA locations were ARFI imaged before (single acquisition) and after (three sequential acquisitions) a 60 second ablation. All post images showed a decrease in the measured ARFI-induced displacements, and the average percentage decrease in the displacements at the ACC site post ablation was ~47%. The average coefficient of variation between sequential images (mean of 0.23, range between 0.07 – 0.46) indicated there was low-variability and good repeatability of the post ablation displacement measurements. A summary of the statistical results is presented in table 14.

6.4 Discussion and Conclusions

The preliminary clinical study presented in this chapter demonstrated ARFI imaging is feasible in human patients using catheters and equipment currently available for clinical care. Several anatomical structures typically targeted during TCA for

treatment of AF were successfully ARFI imaged from inside the LA. Intraprocedure ARFI imaging identified a ~47% reduction in the relative stiffness in human myocardium at RFA sites. This is similar to the difference between the mean displacements seen in the canine subjects between RFA sites and unablated myocardium.

6.4.1 Clinical Experience Observations

The LoM was imaged in 5 of the 6 clinical patients, and proved to be the easiest structure to image in this preliminary patient group. The LoM is often an arrhythmogenic structure, and the complete ablation of the LoM is a primary goal during most cardiac ablation procedures for AF.[161, 162] It is difficult to achieve transmural lesion in the LoM due to the unique shape and thickness; ARFI images of the post RF ablated LoM showed incomplete ablation transmurality in 4 of the 5 patients after the first round of ablation.

ARFI imaging could be a useful tool to study the optimal amount of RFA that should be applied in specific areas of the atria, such as at the LoM. Studying the optimal RF-delivery duration for structures that need minimal RFA would also be useful. A better understanding of the optimal doses of RFA for the various structures and regions of the heart using ARFI imaging could potentially reduce the length of the procedure,

the number of redo procedures, and the instance of procedural complications association with excessive ablation.

Two main challenges stood out during the initial clinical studies: 1) the difficulty of positioning the catheter parallel to and within 2.5 cm of the myocardium and 2) the need for an efficient method to ECG-gate the ARFI acquisitions.

Quickly and efficiently maneuvering the catheter to within 2.5 cm of the chamber wall was very difficult for several locations. For example, it was only possible to image the LA roof when the catheter was in a steerable sheath. To prepare this technology for future trials and widespread clinical adoption, there will likely need to be an increase in the usable rage of the system. It is estimated that a range of 4-6 cm would provide the needed utility. Unfortunately, development of the current ARFI imaging sequences for existing clinical ICE transducers would only marginally increase the imaging DOF range. With the current transducer, increasing the focal depth beyond 2.0 cm (F/# > 3) decreases the intensity of the focused ARFI-excitation, resulting in a substantial reduction in the energy delivered to the tissue and the resultant displacements. Therefore, a solution to this obstacle will require the development and optimization of the catheter hardware for ARFI imaging. Possible developments could include more controlled steering mechanisms for more degrees of freedom when positioning the ICE

catheter, or modifications to the ultrasound transducer to increase the available imaging DOF.

Manual selection of the ECG-gating delay was often inconsistent and time consuming. As in the animal studies, several images contained large motion artifacts because the acquisition was not fully completed in diastole. The development of software to automatically detect changes in the heart rate and update the ECG-gating delay in real-time could improve the consistency of the acquisition timing. Displaying the ECG and exact acquisition time window would provide an efficient method for the operator to quickly discard and reacquire any images that may have been mistimed.

Future work and further developments for clinical translation, including identification of lesion line gaps with ARFI imaging and the correlation with acute and long-term electrical block, are discussed in the final chapter of this thesis.

6.4.2 Study Limitations

In the pre-clinical studies, the canine subject was in NSR through the majority of the cases. In the clinical patients, the heart was frequently in AF and diastolic-gated images could not be acquired. Several pre-ablation sites were not imaged because the heart was in AF, and this resulted in only a few (n = 6) imaging pairs that could be analyzed. A larger number of post ablation images were acquired because the patients had been cardioverted and restored to NSR. While imaging during AF was beyond the

scope of this research thesis, an effective method for imaging lesions during AF would provide more imaging opportunities in TCA procedures.

6.5 Acknowledgements

For their contributions to this work, I acknowledge Dr. Tristram Bahnson, Dr. Douglas Dumont, Joshua Doherty, and Young Kim.

Chapter 7: Conclusions and Future Work

7.1 Conclusions

It has been previously shown *in vitro* that ARFI imaging accurately measures RFA lesions size when compared to tissue pathology.[31, 32] A preliminary *in vivo* study demonstrated feasibility of RFA lesion visualization with intracardiac ARFI imaging for three endocardial lesions.[96]

The work described in this thesis investigated the hypothesis that ARFI imaging can be used for visualization of RFA lesions during cardiac ablation procedures. This hypothesis was successfully proven with four specific aims.

The transition from an *in vitro* model to an *in vivo* model presented new challenges that could have affected the ability of ARFI imaging to visualize RFA lesions, including: 1) cardiac motion, 2) changes in the myocardium stiffness through the cardiac cycle, and 3) transient physiological processes that affect the tissue elasticity such as interstitial edema. In the first aim it was shown that ARFI imaging can be used to visualize RFA lesions with high C and CNR during and immediately after RFA *in vivo*, and ARFI determined lesion stiffness and area were temporally and spatially stable within several minutes of the ablation. This experiment demonstrated ARFI imaging

can be used to evaluate RFA lesions based on the change in tissue stiffness throughout a TCA procedure in a living heart.

Two-dimensional ARFI image acquisition rates are limited by the time needed to acquire the image (50-100 ms) and the necessity for diastolic-gated acquisitions for measurable lesion contrast. With a frame rate of approximately one per second, it would be time consuming to scan the cardiac chamber for ablation lesions with 2-D ARFI imaging. An integrated ARFI imaging-EAM system was developed in the second research aim to efficiently guide intraprocedure ARFI imaging of RFA lesions. Transcatheter ablation lesion sites were accurately identified with this system in an animal model.

The purpose of TCA is to block or isolate electrical conduction of a cardiac arrhythmia. To be a relevant method for clinical evaluation of RFA lesions, ARFI image lesion assessments must be consistent with electrical substrate modification at the imaging site. The results of the third experimental aim verified the presence of conduction disturbances at ARFI imaging determined RFA sites, thereby confirming the lesion assessment was consistent with the clinical gold-standard for lesion evaluation.

In the last aim, the feasibility of identifying RFA lesions based on the tissue stiffness at clinically relevant sites in human myocardium was investigated. Results from a pilot study of ARFI imaging in human patients undergoing TCA for AF

confirmed ARFI imaging measured a decrease in the relative tissue stiffness at RFA sites. These results support the undertaking of a larger clinical trial.

Until this point, MRI and computed tomography (CT) have dominated the effort to develop an imaging method for RFA lesion characterization during clinical cardiac ablation procedures. This work is the first to demonstrate that the difference in the tissue elasticity between normal and ablated myocardium can be used as an indicator of lesion location and size. While ARFI imaging was the only modality used to characterize the stiffness change in this thesis, other imaging modalities could emerge that take advantage of the elasticity contrast shown in this work. The promising results of this research also establish ARFI imaging as a potential tool for intraprocedure lesion characterization during clinical TCA, and this work should encourage the commercial development of ARFI imaging tools and techniques for the assessment of cardiac ablation lesions.

7.1.1 Factors for Clinical Translation

ARFI imaging shows great potential for RFA lesion evaluation in clinical TCA procedures. Development and optimization of the technology and methods are needed, but the results presented in this thesis lay the groundwork for clinical feasibility of this technology.

As previously mentioned, the clinical equipment needed to implement ARFI imaging is currently used in TCA procedures. Therefore, the integration of a multi-modality ARFI imaging-EAM system into existing EP labs may not require a significant investment in equipment. The expenses and resources needed to obtain and operate the systems would also be substantially less burdensome for rural and developing world centers than other complex imaging solutions for lesion characterization such as MRI.

Introduction of the ICE imaging catheter into the LA is not a common practice for the majority of electrophysiologists, and the catheter manipulation techniques needed to obtain useful images would require practice and would improve with experience. Regardless, additional training to implement a clinical ARFI imaging system would be minimal for current clinical operators because it uses existing clinical imaging tools.

7.1.2 Significance for Procedure Safety

ARFI imaging could be used to investigate optimal site-specific RF-energy dosages for different regions of the heart. Visual feedback of lesion size and placement would determine the amount of RF-energy necessary to completely ablate the target site, while minimizing damage to collateral tissue.

Due to the unpredictability of determining pathological lesion size based on the RF-energy delivery parameters, particularly when using irrigated ablation catheters

where the ablation is not temperature controlled, clinical operators may apply excessive RF-energy at a target site to improve the likelihood of complete ablation. In some cases, such over-titration of RF-energy can cause life-threatening complications during the ablation procedure, in particular: 1) perforation of the cardiac wall due to a "steam pop" in overheated myocardium (cardiac tamponade) or 2) severe damage to the esophagus due to excessive RF-energy delivery in the adjoining myocardium (transesophageal fistula).[4, 84] The ability to directly visualize RFA lesions in the myocardium during the ablation procedure would provide feedback to help minimize RF-energy delivery. Optimization of the RF-energy delivery could reduce procedural complications caused by excessive RFA and improve overall procedure safety.

7.2 Continuing Efforts and Future Work

7.2.1 Development of a Clinically Approved ARFI Imaging-EAM System

An approved integrated platform for the ACUSON SC2000™ ultrasound scanner (Siemens Healthcare; Issaquah, WA) and CARTO 3™ and SoundStar™ (Biosense Webster; Diamond Bar, CA) was recently announced. This platform can be used for a clinically approved version of the integrated system described in chapter 4.

An integrated SC2000-CARTO 3 clinical system is currently being developed for ARFI imaging, and images have been gathered in four patients undergoing catheter ablation with an introductory version of this system (Duke IRB approved). Work on a

clinical imaging tool for the SC2000 scanner is also currently in progress. A preliminary image from a patient imaged with the system in shown in figure 32.

This system will provide a platform for conducting larger scale clinical studies for intracardiac ARFI imaging, including: 1) assessing the temporal-spatial stability of acute RFA lesions in human myocardium, 2) the reliability of differentiating complete electrical block from transient electrical block based on the tissue stiffness, 3) and characterization of chronic RFA lesions that are primarily composed of fibrotic scar.

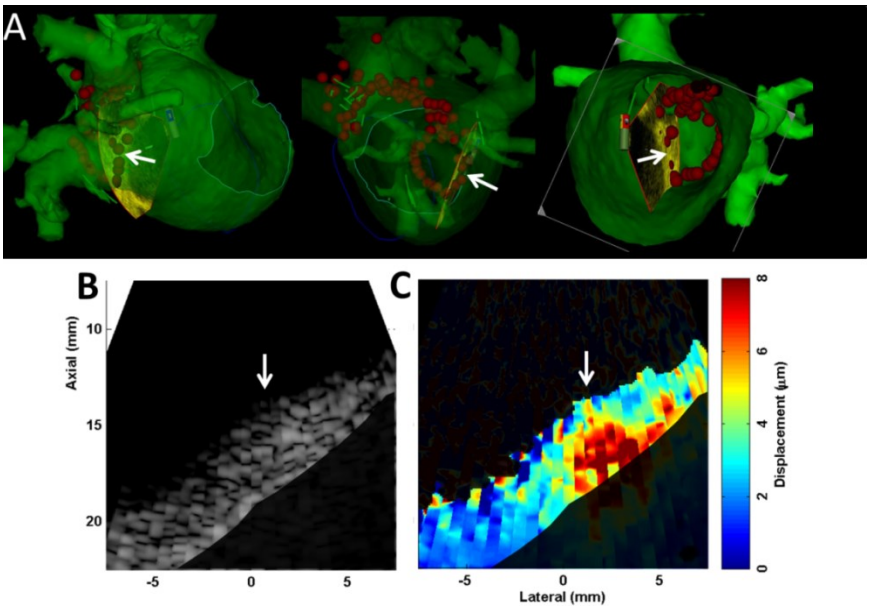

Figure 32: ARFI imaging with an integrated SC2000-CARTO3 imaging system. Panel A depicts an EAM geometry merged with a registered MRI image (CARTO 3™/CARTOMerge™). The ICE catheter and the 2-D ICE imaging plan are projected in EAM, and points of RFA are denoted by red spheres. Panel B and C are the ICE and ARFI images corresponding to the projected imaging plane in A. The arrow in all panels denotes a point of interest where the measured ARFI-induced displacements suggested an unablated gap between RFA lesions.

7.2.2 Development of 3-D ARFI Imaging

Precisely aligning the straight 2-D ARFI imaging plane to cross-sect lines of irregular RFA lesions is challenging. Misalignment with the lesion line could generate ambiguous images of potential lesion line gaps. For example, figure 32 shows an unablated area in the center of the imaging location; it is not clear when examining the EAM markers if this gap corresponds to a discontinuity in the lesion line or is rather the result of imaging slightly inside the curved lesion line. While additional 2-D ARFI images in this area or validation of electrical connection could clarify the significance of the gap, 3-D ARFI imaging would greatly improve the ease and the reliability of characterizing such discontinuities. ARFI imaging in 3-D could also reduce the dependence on EAM for guidance when imaging RFA sites. Siemens Healthcare recently released the AcuNav V™, a 3-D ICE imaging catheter for the SC2000 ultrasound scanner. ARFI imaging development for this novel intracardiac transducer is underway.

7.2.3 Optimization of Intracardiac ARFI Imaging Sequences and Displacement Motion Filtering

Before the launch of widespread clinical trials, steps must be taken to optimize the ARFI imaging sequences and processing methods for image formation and display in a clinical setting. A thorough investigation of the optimal configuration of pre and post-excitation track-lines, priming pulse application, line sampling density, and maximum steering angle could improve the ARFI imaging quality.

The optimal motion filtering technique for intracardiac ARFI imaging also requires further investigation. It has been shown that extrapolation motion filters offer the best estimate of cardiac motion immediately after the ARFI-excitation (0.1 ms), whereas interpolation motion filters better estimate the physiological motion during the post-excitation tissue recovery (0.7 ms).[130] It was also shown that a quadratic fit may not be an ideal estimate for the physiological motion profile.[130] More sophisticated physiological motion estimation functions and catheter kick-back filtering methods could reduce the bias and jitter in the displacement estimations and improve image quality. Current motion filters are applied to each individual pixel with no regard for the estimated motion of neighboring pixels. Motion filtering techniques that employ a spatially-interpolative algorithm are under investigation. Application of a "no push" or zero power ARFI-excitation sequence to monitor the pure physiological motion at the imaging location may also prove a useful tactic for filtering the ARFI-induced displacement estimations.

7.2.4 Correlation of ARFI Images to Tissue Histology, Ablation Temperature, and Electrical Viability

Further investigation of the histological significance of the stiffness and stiffness gradients seen in ARFI images is recommended. A direct comparison of the ARFI images to the *ex vivo* tissue cellular level histology has not been completed due to the difficulty of accurately aligning the imaging plane to the histology slice. Methods to

acquire spatially registered *ex vivo* histology and ARFI images are currently in discussion.

Plans are underway to modify the experimental setup presented in chapter 3 to characterize the relationship between RF-induced tissue damage as measured by the relative myocardial stiffness in ARFI images and the ablation temperature and electrical conductivity at the ablation site. An investigation of the ability of ARFI imaging to accurately differentiate complete thermocoagulation necrosis from reversibly stunned myocardium is also in progress. Such experiments will provide valuable insight for ARFI imaging technologies, as well as increasing the general understanding of the bio-physical mechanisms of RFA.

7.2.5 ARFI imaging During Atrial Fibrillation

It is possible to acquire ARFI images during AF, although the images cannot be ECG-gated to diastole and may be overwhelmed by motion artifacts. Possible methods for acquiring interpretable images of RFA lesions and tissue elasticity during AF are under investigation; different types of ARFI-based imaging methods, for example fast rate stiffness monitoring with ARFI m-mode and composite ARFI images built from sequential un-gated acquisitions, may prove to be useful tools for identifying RFA lesions during AF.

7.2.6 Evaluation of Other Ablation Modalities with ARFI imaging

While radiofrequency ablation is currently the most common ablation modality used in clinical practice, other ablation modalities such as cryoablation and laser ablation are gaining popularity in PVI occlusion-ablation devices.[82, 163, 164] It is likely that any hyperthermic ablation modality (laser, microwave) would exhibit a similar thermocoagulation response to RFA, and could potentially be evaluated with ARFI imaging.

The mechanism for tissue necrosis is significantly different for hypothermic cryoablation.[165] A preliminary feasibility study found ARFI imaging can visualize cryoablation lesions *in vivo*; it is conjectured that cell rapture and severe interstitial edema increases the stiffness at the ablation site, but further work is necessary to evaluate the feasibility of characterizing cryoablation lesions with ARFI imaging.[166]

The experimental method presented in chapter 3 would be a powerful validation tool for testing new ablation catheter designs due to its unique ability to capture snapshots of the lesion size and morphology within living myocardium during lesion formation. In recent years, contact-force catheters have been developed to increase the confidence of the myocardium-electrode contact during lesion delivery.[15, 16, 167, 168] ARFI imaging could be a useful tool for confirming and optimizing the force necessary for complete transmural ablation.

Appendix A: Introduction to CARTO

Electroanatomical mapping and navigation systems are widely used in clinical ablation procedures.[4] The CARTO XP™ EP navigation system (Biosense Webster®, Inc., Diamond Bar, CA) was developed to serve four main functions: 1) accurately locate the 3D location of catheter tips without fluoroscopy, 2) construct a 3D geometric representation of relevant cardiac chambers and anatomy using points locations cataloged from the catheter positions, 3) tag important locations in the chamber geometry, such as RFA delivery locations, and 4) capture and map local electrical information onto the 3D geometries for large scale understanding of the complex arrhythmia.[41]

A.1 Magnetic Tracking

A coil placed in a magnetic field will generate an electrical current that is dependent on the field strength and the orientation of the coil within the field. The CARTO navigation system triangulates the position and orientation of the mapping catheter (NaviStar™) and ultrasound (SoundStar™) catheter tips in using location sensor coils in the catheter tip. The coils measure the magnetic field generated by a magnetic location pad mounted to the procedure table directly under the patient's

thoracic cavity; the pad generates three low strength ($5x10^{-6}$ to $5x10^{-5}$ Tesla) magnetic fields that decay as a function of distance from the pad.[169] The heart is contained in the mapping area, and the location sensor measures the strength of the magnetic field. The strength of the magnetic field determines the distance of the sensor from each of the three magnetic field sources. The distances are considered radii of theoretical spheres around the field origins, and the calculated intersection of the three spheres is the spatial location of the catheter tip sensor. The CARTO XP system has been shown to locate the catheter tip to within 1 mm of the actual 3-D position.[97]

A.2 CARTO Maps

Figure 33 shows an example of a CARTO geometry map. The 3-D positions of the catheter tips are displayed in the CARTO software relative to a stationary reference patch attached to the back of the patient. A 3-D volume of the cardiac chamber is constructed by maneuvering the NaviStar™ to multiple locations along the endocardial walls and plotting the relative tip positions. The heart chamber geometry is interpolated from a point catalog of the acquired mapping catheter positions.

During RFA, the NaviStar™ tip location is marked on the 3D geometry to indicate an RFA treatment location. On the map, the RFA spherical point markers are purely location tags and do not represent lesion size.

The SoundStar™ catheter position is also located in the mapping area. The location and orientation of the ICE catheter and imaging plane can be projected in the CARTO geometry using the CARTOSound™ module. One study measured a mean distance error of ~1.5 mm between the contour of the endocardium in the ICE plane projection and the CARTO geometry in the human LA.[170]

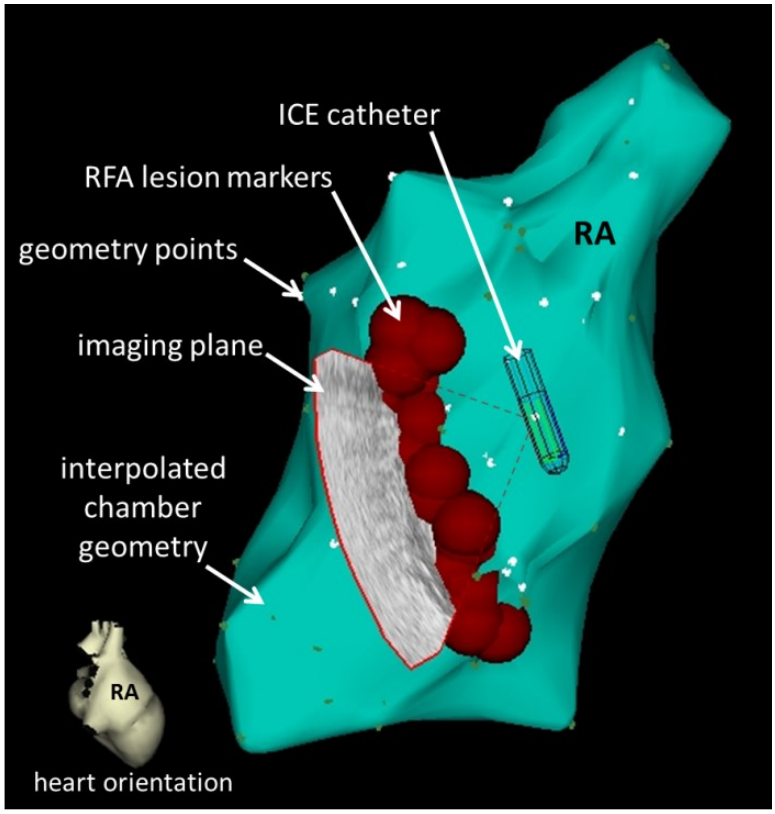

Figure 33. CARTO XP™ right atrium (RA) geometry showing RFA markers and the orientation of the ICE imaging fan in the geometry (CARTOSound™).

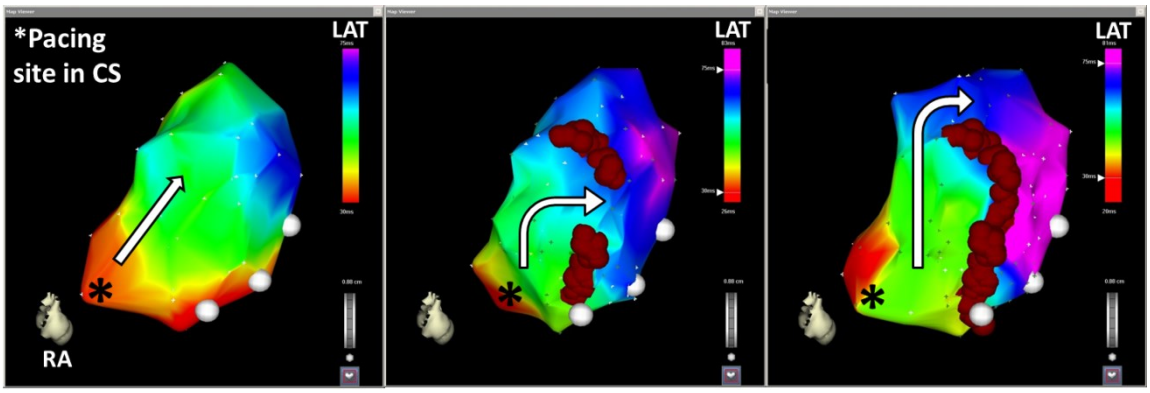

Figure 34. CARTO local activation time (LAT) maps of a canine right atrium (RA) before (left), after incomplete linear RFA (center), and after complete linear ablation (right). The heart was paced from the coronary sinus (CS). Color scale represents activation time, where red is the earliest activation time and magenta is the latest. White arrow indicates direction of electrical propagation. Red spheres indicate RFA treatment locations. The white spheres outline the tricuspid annulus.

Conduction maps are constructed before and after RFA to identify the initial arrhythmia for ablation and confirm substrate modification.[41, 169] The NaviStar™ mapping catheter tip collects endocardial EG at each contact position. Local activation times (LAT) are calculated relative to a reference EG, and plotted on the surface of the 3-D volume using a color scale. The reference EG is often a separate sensing/pacing catheter that is positioned in the CS. The LAT map provides visualization of the electrical propagation through the cardiac chamber and is used to identify arrhythmogenic ablation targets and confirm electrical block. Figure 34 shows example LAT maps for a linear ablation.

A.3 Magnetic vs. Electric Impedance-Based Mapping Systems

As previously described, the CARTO XP™ and CARTO 3™ EAM systems locate catheter tips and the tip orientation in the heart using magnetic tracking technology. A second type of EAM mapping system in clinical use is the St. Jude Medical NavX™ and the next generation Ensite Velocity™ navigation system (St. Jude Medical Inc.; Minneapolis, MN). These systems use external surface patches to generate transthoracic electrical fields in three orthogonal directions; the electric field measured by the catheter electrode determines the 3-D position of the catheter tip in the mapping area.[171, 172] Unfortunately, while this electrical impedance-based mapping method accurately locates catheter tips in the heart, the catheter orientation, specifically the yaw, pitch, and roll, cannot be determined with this method. These orientation parameters are necessary to accurately determine the direction of the projected ultrasound imaging plane from the ICE catheter. Therefore, existing electrical impedance-based mapping systems cannot be used to guide intraprocedure ARFI imaging as was done with the CARTO mapping system in this thesis.

Appendix B: Image Review Considerations

Chapters 4 and 5 presented the accuracy of identifying RFA lesions with ARFI imaging based on image reviews from calibrated ARFI image readers. It is important to note that the dynamic range of the displayed maximum ARFI-induced displacement was manually chosen for each image. The chosen dynamic range was selected to maximize the contrast and minimize color saturation; the sensitivities and specificities reported in these chapters represent the detection accuracy for the chosen display range. It must be acknowledged that the selection of a different display dynamic range could result in a different image review. In future work, providing the image reader with a control to adjust the display dynamic range during review could provide a more robust interpretation of the image, effectively allowing the reader to observe the complete receiver operating characteristic (ROC) curve during the analysis.[173]

The reading of the LAT maps to identify conduction disturbances at the imaging plane, such as in chapter 5, could also benefit from the inclusion of user controls during review. Providing the reader the ability to rotate the 3-D geometry as well as manually adjust the LAT color map gradient would be a more robust review method for future projects.

References

1. Naccarelli GV, Varker H, Lin J, Schulman KL. Increasing prevalence of atrial fibrillation and flutter in the united states. *Am J Cardiol*. 2009;104:1534-1539

2. Go AS. Prevalence of diagnosed atrial fibrillation in adults: National implications for rhythm management and stroke prevention: The anticoagulation and risk factors in atrial fibrillation (atria) study. *J Amer Med Assoc*. 2001;285:2370-2375

3. Wattigney WA, Mensah GA, Croft JB. Increasing trends in hospitalization for atrial fibrillation in the united states, 1985 through 1999 - implications for primary prevention. *Circulation*. 2003;108:711-716

4. Calkins H, Kuck KH, Cappato R, Brugada J, Camm AJ, Chen SA, Crijns HJ, Damiano RJ, Jr., Davies DW, DiMarco J, Edgerton J, Ellenbogen K, Ezekowitz MD, Haines DE, Haissaguerre M, Hindricks G, Iesaka Y, Jackman W, Jalife J, Jais P, Kalman J, Keane D, Kim YH, Kirchhof P, Klein G, Kottkamp H, Kumagai K, Lindsay BD, Mansour M, Marchlinski FE, McCarthy PM, Mont JL, Morady F, Nademanee K, Nakagawa H, Natale A, Nattel S, Packer DL, Pappone C, Prystowsky E, Raviele A, Reddy V, Ruskin JN, Shemin RJ, Tsao HM, Wilber D, Heart Rhythm Society Task Force on C, Surgical Ablation of Atrial F. 2012 hrs/ehra/ecas expert consensus statement on catheter and surgical ablation of atrial fibrillation: Recommendations for patient selection, procedural techniques, patient management and follow-up, definitions, endpoints, and research trial design. *Heart Rhythm*. 2012;9:632-696 e621

5. Cappato R, Calkins H, Chen SA, Davies W, Iesaka Y, Kalman J, Kim YH, Klein G, Natale A, Packer D, Skanes A, Ambrogi F, Biganzoli E. Updated worldwide survey on the methods, efficacy, and safety of catheter ablation for human atrial fibrillation. *Circ Arrhythm Electrophysiol*. 2010;3:32-38

6. Callans DJ, Gerstenfeld EP, Dixit S, Zado E, Vanderhoff M, Ren JF, Marchlinski FE. Efficacy of repeat pulmonary vein isolation procedures in patients with recurrent atrial fibrillation. *J Cardiovasc Electrophysiol*. 2004;15:1050-1055

7. Melby SJ, Lee AM, Zierer A, Kaiser SP, Livhits MJ, Boineau JP, Schuessler RB, Damiano RJ. Atrial fibrillation propagates through gaps in ablation lines: Implications for ablative treatment of atrial fibrillation. *Heart Rhythm*. 2008;5:1296-1301

8. Kowalski M, Grimes MM, Perez FJ, Kenigsberg DN, Koneru J, Kasirajan V, Wood MA, Ellenbogen KA. Histopathologic characterization of chronic radiofrequency ablation lesions for pulmonary vein isolation. *J Am Coll Cardiol*. 2012;59:930-938

9. Tungjitkusolmun S, Woo EJ, Cao H, Tsai JZ, Vorperian VR, Webster JG. Finite element analyses of uniform current density electrodes for radio-frequency cardiac ablation. *IEEE Trans Biomed Eng*. 2000;47:32-40

10. Jain MK, Wolf PD. A three-dimensional finite element model of radiofrequency ablation with blood flow and its experimental validation. *Ann Biomed Eng*. 2000;28:1075-1084

11. Zheng X, Walcott GP, Rollins DL, Hall JA, Smith WM, Kay GN, Ideker RE. Comparison of the temperature profile and pathological effect at unipolar, bipolar and phased radiofrequency current configurations. *J Interv Card Electrophysiol*. 2001;5:401-410

12. Pilcher TA, Saul JP, Hlavacek AM, Haemmerich D. Contrasting effects of convective flow on catheter ablation lesion size: Cryo versus radiofrequency energy. *Pacing and Clin Electrophysiol*. 2008;31:300-307

13. Haines DE. The yin and yang of convective cooling in radiofrequency catheter ablation. *Circ Arrhythm Electrophysiol*. 2011;4:794-795

14. Martinek M, Lemes C, Sigmund E, Derndorfer M, Aichinger J, Winter S, Nesser HJ, Purerfellner H. Clinical impact of an open-irrigated radiofrequency catheter with direct force measurement on atrial fibrillation ablation. *Pacing Clin Electrophysiol*. 2012;35:1312-1318

15. Reddy VY, Shah D, Kautzner J, Schmidt B, Saoudi N, Herrera C, Jais P, Hindricks G, Peichl P, Yulzari A, Lambert H, Neuzil P, Natale A, Kuck KH. The relationship between contact force and clinical outcome during radiofrequency catheter ablation of atrial fibrillation in the toccata study. *Heart Rhythm*. 2012;9:1789-1795

16. Kumar S, Haqqani HM, Chan M, Lee J, Yudi M, Wong MC, Morton JB, Ling LH, Robinson T, Heck PM, Kelland NF, Halloran K, Spence SJ, Kistler PM, Kalman JM. Predictive value of impedance changes for real-time contact force measurements during catheter ablation of atrial arrhythmias in humans. *Heart Rhythm*. 2013

17. Balk EM, Garlitski AC, Alsheikh-Ali AA, Terasawa T, Chung M, Ip S. Predictors of atrial fibrillation recurrence after radiofrequency catheter ablation: A systematic review. *J Cardiovasc Electrophysiol*. 2010;21:1208-1216

18. Mickelsen S, Dudley B, Treat E, Barela J, Omdahl J, Kusumoto F. Survey of physician experience, trends and outcomes with atrial fibrillation ablation. *J Interv Card Electrophysiol*. 2005;12:213-220

19. Rostock T, O'Neill MD, Sanders P, Rotter M, Jais P, Hocini M, Takahashi Y, Sacher F, Jonsson A, Hsu LF, Clementy J, Haissaguerre M. Characterization of conduction recovery across left atrial linear lesions in patients with paroxysmal and persistent atrial fibrillation. *J Cardiovasc Electrophysiol*. 2006;17:1106-1111

20. Rostock T, Salukhe TV, Steven D, Drewitz I, Hoffmann BA, Bock K, Servatius H, Müllerleile K, Sultan A, Gosau N, Meinertz T, Wegscheider K, Willems S. Long-

term single and multiple procedure outcome and predictors of success after catheter ablation for persistent atrial fibrillation. *Heart Rhythm*. 2011

21. Gaztañaga L, Frankel DS, Kohari M, Kondapalli L, Zado ES, Marchlinski FE. Time to recurrence of atrial fibrillation influences outcome following catheter ablation. *Heart rhythm : the official journal of the Heart Rhythm Society*. 2013;10:2-9

22. Nightingale K, Soo MS, Nightingale R, Trahey G. Acoustic radiation force impulse imaging: In vivo demonstration of clinical feasibility. *Ultrasound Med Biol*. 2002;28:227-235

23. Pinton GF, Dahl JJ, Trahey GE. Rapid tracking of small displacements with ultrasound. *IEEE Trans Ultrason Ferroelectr Freq Control*. 2006;53:1103-1117

24. Hsu SJ, Bouchard RR, Dumont DM, Ong CW, Wolf PD, Trahey GE. Novel acoustic radiation force impulse imaging methods for visualization of rapidly moving tissue. *Ultrason Imaging*. 2009;31:183-200

25. Palmeri ML, Sharma AC, Bouchard RR, Nightingale RW, Nightingale KR. A finite-element method model of soft tissue response to impulsive acoustic radiation force. *IEEE Trans Ultrason Ferroelectr Freq Control*. 2005;52:1699-1712

26. Nightingale K, Bentley R, Trahey G. Observations of tissue response to acoustic radiation force: Opportunities for imaging. *Ultrason Imaging*. 2002;24:129-138

27. Nath S, Redick JA, Whayne JG, Haines DE. Ultrastructural observations in the myocardium beyond the region of acute coagulation necrosis following radiofrequency catheter ablation. *J Cardiovasc Electrophysiol*. 1994;5:838-845

28. Bosman S, Pickering JW, van Marle J, van Gemert MJ. Ultrastructural alterations in heated canine myocardium. *Lasers Surg Med*. 1995;17:39-48

29. Pernot M, Mace E, Dubois R, Couade M, Fink M, Tanter M. Mapping myocardial elasticity changes after rf-ablation using supersonic shear imaging. *Computers in Cardiology, 2009*. 2009:793-796

30. Wright NT, Humphrey JD. Denaturation of collagen via heating: An irreversible rate process. *Annual review of biomedical engineering*. 2002;4:109-128

31. Eyerly SA, Hsu SJ, Agashe SH, Trahey GE, Li Y, Wolf PD. An in vitro assessment of acoustic radiation force impulse imaging for visualizing cardiac radiofrequency ablation lesions. *J Cardiovasc Electrophysiol*. 2010;21:557-563

32. Eyerly SA, Dumont DM, Trahey GE, Wolf PD. In vitro monitoring of the dynamic elasticity changes during radiofrequency ablation with acoustic radiation force impulse imaging. *J Cardiovasc Electrophysiol*. 2013;24:472-473

33. Konings KT, Kirchhof CJ, Smeets JR, Wellens HJ, Penn OC, Allessie MA. High-density mapping of electrically induced atrial fibrillation in humans. *Circulation*. 1994;89:1665-1680

34. Nattel S. New ideas about atrial fibrillation 50 years on. *Nature*. 2002;415:219-226

35. Allessie MA, Boyden PA, Camm AJ, Kleber AG, Lab MJ, Legato MJ, Rosen MR, Schwartz PJ, Spooner PM, Van Wagoner DR, Waldo AL. Pathophysiology and prevention of atrial fibrillation. *Circulation*. 2001;103:769-777

36. Everett THt, Olgin JE. Atrial fibrosis and the mechanisms of atrial fibrillation. *Heart Rhythm*. 2007;4:S24-27

37. Everett THt. Pulmonary veins and the initiation of atrial fibrillation: Are we getting closer to understanding their role? *Heart Rhythm*. 2007;4:1563-1564

38. Chen YJ, Chen SA. Electrophysiology of pulmonary veins. *J Cardiovasc Electrophysiol*. 2006;17:220-224

39. Chen YJ, Chen SA, Chen YC, Yeh HI, Chang MS, Lin CI. Electrophysiology of single cardiomyocytes isolated from rabbit pulmonary veins: Implication in initiation of focal atrial fibrillation. *Basic Res Cardiol*. 2002;97:26-34

40. Chen YJ, Chen SA, Chen YC, Yeh HI, Chan P, Chang MS, Lin CI. Effects of rapid atrial pacing on the arrhythmogenic activity of single cardiomyocytes from pulmonary veins: Implication in initiation of atrial fibrillation. *Circulation*. 2001;104:2849-2854

41. Calkins H, Jais P, Steinberg JS. *A practical approach to catheter ablation of atrial fibrillation*. Philadelphia: Wolters Kluwer/Lippincott Williams & Wilkins Health; 2008.

42. Fuster V, Ryden LE, Cannom DS, Crijns HJ, Curtis AB, Ellenbogen KA, Halperin JL, Le Heuzey JY, Kay GN, Lowe JE, Olsson SB, Prystowsky EN, Tamargo JL, Wann S, Smith SC, Jacobs AK, Adams CD, Anderson JL, Antman EM, Hunt SA, Nishimura R, Ornato JP, Page RL, Riegel B, Priori SG, Blanc JJ, Budaj A, Camm AJ, Dean V, Deckers JW, Despres C, Dickstein K, Lekakis J, McGregor K, Metra M, Morais J, Osterspey A, Zamorano JL. Acc/aha/esc 2006 guidelines for the management of patients with atrial fibrillation: Full text: A report of the american college of cardiology/american heart association task force on practice guidelines and the european society of cardiology committee for practice guidelines (writing committee to revise the 2001 guidelines for the management of patients with atrial fibrillation) developed in collaboration with the european heart rhythm association and the heart rhythm society. *Europace*. 2006;8:651-745

43. McRury ID, Haines DE. Ablation for the treatment of arrhythmias. *P Ieee*. 1996;84:404-416

44. Shiroshita-Takeshita A, Brundel BJ, Nattel S. Atrial fibrillation: Basic mechanisms, remodeling and triggers. *J Interv Card Electrophysiol*. 2005;13:181-193

45. Allessie M, Ausma J, Schotten U. Electrical, contractile and structural remodeling during atrial fibrillation. *Cardiovasc Res*. 2002;54:230-246

46. Nattel S, Li D. Ionic remodeling in the heart: Pathophysiological significance and new therapeutic opportunities for atrial fibrillation. *Circ Res*. 2000;87:440-447

47. Dorian P, Jung W, Newman D, Paquette M, Wood K, Ayers GM, Camm J, Akhtar M, Luderitz B. The impairment of health-related quality of life in patients with intermittent atrial fibrillation: Implications for the assessment of investigational therapy. *J Am Coll Cardiol*. 2000;36:1303-1309

48. Wattigney WA, Mensah GA, Croft JB. Increased atrial fibrillation mortality: United states, 1980-1998. *Am J Epidemiol*. 2002;155:819-826

49. Lloyd-Jones D, Adams RJ, Brown TM, Carnethon M, Dai S, De Simone G, Ferguson TB, Ford E, Furie K, Gillespie C, Go A, Greenlund K, Haase N, Hailpern S, Ho PM, Howard V, Kissela B, Kittner S, Lackland D, Lisabeth L, Marelli A, McDermott MM, Meigs J, Mozaffarian D, Mussolino M, Nichol G, Roger VL, Rosamond W, Sacco R, Sorlie P, Stafford R, Thom T, Wasserthiel-Smoller S, Wong ND, Wylie-Rosett J, Stroke AHASC. Heart disease and stroke statistics-2010 update a report from the american heart association. *Circulation*. 2010;121:E46-E215

50. Wilber DJ, Pappone C, Neuzil P, De Paola A, Marchlinski F, Natale A, Macle L, Daoud EG, Calkins H, Hall B, Reddy V, Augello G, Reynolds MR, Vinekar C, Liu CY, Berry SM, Berry DA, Investigators TAT. Comparison of antiarrhythmic drug therapy and radiofrequency catheter ablation in patients with paroxysmal atrial fibrillation a randomized controlled trial. *J Amer Med Assoc*. 2010;303:333-340

51. Calkins H, Reynolds MR, Spector P, Sondhi M, Xu Y, Martin A, Williams CJ, Sledge I. Treatment of atrial fibrillation with antiarrhythmic drugs or radiofrequency ablation: Two systematic literature reviews and meta-analyses. *Circ Arrhythm Electrophysiol*. 2009;2:349-361

52. Cappato R, Calkins H, Chen SA, Davies W, Iesaka Y, Kalman J, Kim YH, Klein G, Natale A, Packer D, Skanes A, Ambrogi F, Biganzoli E. Updated worldwide survey on the methods, efficacy, and safety of catheter ablation for human atrial fibrillation. *Circ Arrhythm Electrophysiol*. 2010;3:32-38

53. Cheema A, Dong J, Dalal D, Marine JE, Henrikson CA, Spragg D, Cheng A, Nazarian S, Bilchick KC, Almasry I, Sinha S, Scherr D, Halperin H, Berger R, Calkins H. Circumferential ablation with pulmonary vein isolation in permanent atrial fibrillation. *Am J Cardiol*. 2007;99:1425-1428

54. Oral H, Pappone C, Chugh A, Good E, Bogun F, Pelosi F, Bates ER, Lehmann MH, Vicedomini G, Augello G, Agricola E, Sala S, Santinelli V, Morady F. Circumferential pulmonary-vein ablation for chronic atrial fibrillation. *New Engl J Med*. 2006;354:934-941

55. Haissaguerre M, Shah DC, Jais P, Hocini M, Yamane T, Deisenhofer I, Chauvin M, Garrigue S, Clementy J. Electrophysiological breakthroughs from the left atrium to the pulmonary veins. *Circulation*. 2000;102:2463-2465

56. Earley MJ. How to perform a transseptal puncture. *Heart*. 2009;95:85-92

57. Akoum N, Daccarett M, McGann C, Segerson N, Vergara G, Kuppahally S, Badger T, Burgon N, Haslam T, Kholmovski E, Macleod R, Marrouche N. Atrial fibrosis helps select the appropriate patient and strategy in catheter ablation of atrial fibrillation: A de-mri guided approach. *J Cardiovasc Electrophysiol*. 2011;22:16-22

58. Labonte S. Numerical model for radio-frequency ablation of the endocardium and its experimental validation. *IEEE Trans Biomed Eng*. 1994;41:108-115

59. Berjano EJ. Theoretical modeling for radiofrequency ablation: State-of-the-art and challenges for the future. *Biomed Eng Online*. 2006;5:24

60. Calkins H, Brugada J, Packer DL, Cappato R, Chen SA, Crijns HJ, Damiano RJ, Jr., Davies DW, Haines DE, Haissaguerre M, Iesaka Y, Jackman W, Jais P, Kottkamp H, Kuck KH, Lindsay BD, Marchlinski FE, McCarthy PM, Mont JL, Morady F, Nademanee K, Natale A, Pappone C, Prystowsky E, Raviele A, Ruskin JN, Shemin RJ. Hrs/ehra/ecas expert consensus statement on catheter and surgical ablation of atrial fibrillation: Recommendations for personnel, policy, procedures and follow-up. A report of the heart rhythm society (hrs) task force on catheter and surgical ablation of atrial fibrillation. *Heart Rhythm*. 2007;4:816-861

61. Shimko N, Savard P, Shah K. Radio frequency perforation of cardiac tissue: Modelling and experimental results. *Med Biol Eng Comput*. 2000;38:575-582

62. Kaouk Z, Shahidi AV, Savard P, Molin F. Modelling of myocardial temperature distribution during radiofrequency ablation. *Med Biol Eng Comput*. 1996;34:165-170

63. Wang PJ. *New arrhythmia technologies*. Malden, Mass.: Blackwell Futura; 2005.

64. Chang IA. Considerations for thermal injury analysis for rf ablation devices. *The open biomedical engineering journal*. 2010;4:3-12

65. Masugata H, Mizushige K, Senda S, Kinoshita A, Sakamoto H, Sakamoto S, Matsuo H. Relationship between myocardial tissue density measured by microgravimetry and sound speed measured by acoustic microscopy. *Ultrasound Med Biol*. 1999;25:1459-1463

66. Sekins KM, Emery AF, Lehmann JF, MacDougall JA. Determination of perfusion field during local hyperthermia with the aid of finite element thermal models. *J Biomech Eng*. 1982;104:272-279

67. Petersen HH, Chen X, Pietersen A, Svendsen JH, Haunso S. Temperature-controlled radiofrequency ablation of cardiac tissue: An in vitro study of the impact of electrode orientation, electrode tissue contact pressure and external convective cooling. *J Interv Card Electrophysiol*. 1999;3:257-262

68. Tungjitkusolmun S, Woo EJ, Cao H, Tsai JZ, Vorperian VR, Webster JG. Thermal--electrical finite element modelling for radio frequency cardiac ablation: Effects of changes in myocardial properties. *Med Biol Eng Comput*. 2000;38:562-568

69. Wilber DJ, Packer D, Stevenson WG. *Catheter ablation of cardiac arrhythmias : Basic concepts and clinical applications*. Malden, Mass.: Blackwell Futura; 2008.

70. Schwartzman D, Parizhskaya M, Devine WA. Linear ablation using an irrigated electrode electrophysiologic and histologic lesion evolution comparison with ablation utilizing a non-irrigated electrode. *J Interv Card Electrophysiol*. 2001;5:17-26

71. Chang IA, Nguyen UD. Thermal modeling of lesion growth with radiofrequency ablation devices. *Biomed Eng Online*. 2004;3:27

72. Zervas NT, Kuwayama A. Pathological characteristics of experimental thermal lesions - comparison of induction heating and radiofrequency electrocoagulation. *J Neurosurg*. 1972;37:418-&

73. Bharat S, Techavipoo U, Kiss MZ, Liu W, Varghese T. Monitoring stiffness changes in lesions after radiofrequency ablation at different temperatures and durations of ablation. *Ultrasound Med Biol*. 2005;31:415-422

74. Nath S, Lynch C, 3rd, Whayne JG, Haines DE. Cellular electrophysiological effects of hyperthermia on isolated guinea pig papillary muscle. Implications for catheter ablation. *Circulation*. 1993;88:1826-1831

75. Ge YZ, Shao PZ, Goldberger J, Kadish A. Cellular electrophysiological changes induced in vitro by radiofrequency current: Comparison with electrical ablation. *Pacing Clin Electrophysiol*. 1995;18:323-333

76. Schwartzman D, Ren JF, Devine WA, Callans DJ. Cardiac swelling associated with linear radiofrequency ablation in the atrium. *J Interv Card Electrophysio*. 2001;5:159-166

77. Cheema A, Dong J, Dalal D, Marine JE, Henrikson CA, Spragg D, Cheng A, Nazarian S, Bilchick K, Sinha S, Scherr D, Almasry I, Halperin H, Berger R, Calkins H. Incidence and time course of early recovery of pulmonary vein conduction after catheter ablation of atrial fibrillation. *J Cardiovasc Electrophysiol*. 2007;18:387-391

78. Nath S, Whayne JG, Kaul S, Goodman NC, Jayaweera AR, Haines DE. Effects of radiofrequency catheter ablation on regional myocardial blood flow. Possible mechanism for late electrophysiological outcome. *Circulation*. 1994;89:2667-2672

79. Lardo AC, McVeigh ER, Jumrussirikul P, Berger RD, Calkins H, Lima J, Halperin HR. Visualization and temporal/spatial characterization of cardiac radiofrequency ablation lesions using magnetic resonance imaging. *Circulation*. 2000;102:698-705

80. Badger TJ, Adjei-Poku YA, Marrouche NF. Mri in cardiac electrophysiology: The emerging role of delayed-enhancement mri in atrial fibrillation ablation. *Future cardiology*. 2009;5:63-70

81. Dickfeld T, Kato R, Zviman M, Nazarian S, Dong J, Ashikaga H, Lardo AC, Berger RD, Calkins H, Halperin H. Characterization of acute and subacute

radiofrequency ablation lesions with nonenhanced magnetic resonance imaging. *Heart rhythm : the official journal of the Heart Rhythm Society*. 2007;4:208-214

82. Herrera Siklody C, Arentz T, Minners J, Jesel L, Stratz C, Valina CM, Weber R, Kalusche D, Toti F, Morel O, Trenk D. Cellular damage, platelet activation, and inflammatory response after pulmonary vein isolation: A randomized study comparing radiofrequency ablation with cryoablation. *Heart Rhythm*. 2012;9:189-196

83. Spragg DD, Dalal D, Cheema A, Scherr D, Chilukuri K, Cheng A, Henrikson CA, Marine JE, Berger RD, Dong J, Calkins H. Complications of catheter ablation for atrial fibrillation: Incidence and predictors. *J Cardiovasc Electrophysiol*. 2008;19:627-631

84. Everett Iv TH, Lee KW, Wilson EE, Guerra JM, Varosy PD, Olgin JE. Safety profiles and lesion size of different radiofrequency ablation technologies: A comparison of large tip, open and closed irrigation catheters. *J Cardiovasc Electrophysiol*. 2009;20:325-335

85. Dong J, Vasamreddy CR, Jayam V, Dalal D, Dickfeld T, Eldadah Z, Meininger G, Halperin HR, Berger R, Bluemke DA, Calkins H. Incidence and predictors of pulmonary vein stenosis following catheter ablation of atrial fibrillation using the anatomic pulmonary vein ablation approach: Results from paired magnetic resonance imaging. *J Cardiovasc Electrophysiol*. 2005;16:845-852

86. Sonmez B, Demirsoy E, Yagan N, Unal M, Arbatli H, Sener D, Baran T, Ilkova F. A fatal complication due to radiofrequency ablation for atrial fibrillation: Atrio-esophageal fistula. *The Annals of thoracic surgery*. 2003;76:281-283

87. Davies AG, Cowen AR, Kengyelics SM, Moore J, Pepper C, Cowan C, Sivanathan MU. X-ray dose reduction in fluoroscopically guided electrophysiology procedures. *Pacing and Clin Electrophysiol*. 2006;29:262-271

88. Rosenthal LS, Mahesh M, Beck TJ, Saul JP, Miller JM, Kay N, Klein LS, Huang S, Gillette P, Prystowsky E, Carlson M, Berger RD, Lawrence JH, Yong P, Calkins H. Predictors of fluoroscopy time and estimated radiation exposure during radiofrequency catheter ablation procedures. *Am J Cardiol*. 1998;82:451-458

89. Ruisi CP, Brysiewicz N, Asnes JD, Sugeng L, Marieb M, Clancy J, Akar JG. Use of intracardiac echocardiography during atrial fibrillation ablation. *Pacing Clin Electrophysiol*. 2013

90. Proulx TL, Tasker D, Bartlett-Roberto J. Advances in catheter-based ultrasound imaging intracardiac echocardiography and the acuson acunavtm ultrasound catheter. 2005;1:669-678

91. Natale A. *Intracardiac echocardiography in interventional electrophysiology*. Abingdon U.K.: Informa Healthcare; 2006.

92. Robinson MR, Hutchinson MD. Use of imaging techniques to guide catheter ablation procedures. *Curr Cardiol Rep*. 2010;12:374-381

93. Yamada T, McElderry HT, Epstein AE, Plumb VJ, Kay GN. One-puncture, double-transseptal catheterization manoeuvre in the catheter ablation of atrial fibrillation. *Europace*. 2007;9:487-489

94. Das MK, Yadav AV, Zipes DP. Atrial fibrillation: Future directions. *Atrial fibrillation*. Springer; 2008:429-443.

95. Fahey BJ, Nightingale KR, McAleavey SA, Palmeri ML, Wolf PD, Trahey GE. Acoustic radiation force impulse imaging of myocardial radiofrequency ablation: Initial in vivo results. *IEEE Trans Ultrason Ferroelectr Freq Control*. 2005;52:631-641

96. Hsu SJ, Fahey BJ, Dumont DM, Wolf PD, Trahey GE. Challenges and implementation of radiation-force imaging with an intracardiac ultrasound transducer. *IEEE Trans Ultrason Ferroelectr Freq Control*. 2007;54:996-1009

97. Gepstein L, Hayam G, Ben-Haim SA. A novel method for nonfluoroscopic catheter-based electroanatomical mapping of the heart. In vitro and in vivo accuracy results. *Circulation*. 1997;95:1611-1622

98. Kolandaivelu A, Zviman MM, Castro V, Lardo AC, Berger RD, Halperin HR. Noninvasive assessment of tissue heating during cardiac radiofrequency ablation using mri thermography. *Circ Arrhythm Electrophysiol*. 2010;3:521-529

99. Dickfeld T, Kato R, Zviman M, Lai S, Meininger G, Lardo AC, Roguin A, Blumke D, Berger R, Calkins H, Halperin H. Characterization of radiofrequency ablation lesions with gadolinium-enhanced cardiovascular magnetic resonance imaging. *J Am Coll Cardiol*. 2006;47:370-378

100. Nazarian S, Kolandaivelu A, Zviman MM, Meininger GR, Kato R, Susil RC, Roguin A, Dickfeld TL, Ashikaga H, Calkins H, Berger RD, Bluemke DA, Lardo AC, Halperin HR. Feasibility of real-time magnetic resonance imaging for catheter guidance in electrophysiology studies. *Circulation*. 2008;118:223-229

101. Wilkoff BL. Abstract plus session ab41: Advances in imaging and mapping for vt ablation. *Supplement to Heart Rhythm: 31st Annual Scientific Sessions of the Heart Rhythm Society*. 2010;7:S84 - S86

102. Reddy VY, Schmidt EJ, Holmvang G, Fung M. Arrhythmia recurrence after atrial fibrillation ablation: Can magnetic resonance imaging identify gaps in atrial ablation lines? *J Cardiovasc Electrophysiol*. 2008;19:434-437

103. Kolandaivelu A, Zviman MM, Castro V, Lardo AC, Berger RD, Halperin HR. Noninvasive assessment of tissue heating during cardiac radiofrequency ablation using mri thermography. *Circ Arrhythm Electrophysiol*. 2010;3:521-529

104. Vergara GR, Vijayakumar S, Kholmovski EG, Blauer JJE, Guttman MA, Gloschat C, Payne G, Vij K, Akoum NW, Daccarett M, McGann CJ, Macleod RS, Marrouche NF. Real-time magnetic resonance imaging-guided radiofrequency atrial ablation and visualization of lesion formation at 3 tesla. *Heart Rhythm*. 2011;8:295-303

105. Akoum N, Daccarett M, McGann C, Segerson N, Vergara G, Kuppahally S, Badger T, Burgon N, Haslam T, Kholmovski E, Macleod R, Marrouche N. Atrial fibrosis helps select the appropriate patient and strategy in catheter ablation of atrial fibrillation: A de-mri guided approach. *J Cardiovasc Electrophysiol*. 2011;22:16-22

106. McGann C, Kholmovski E, Blauer J, Vijayakumar S, Haslam T, Cates J, DiBella E, Burgon N, Wilson B, Alexander A, Prastawa M, Daccarett M, Vergara G, Akoum N, Parker D, MacLeod R, Marrouche N. Dark regions of no-reflow on late gadolinium enhancement magnetic resonance imaging result in scar formation after atrial fibrillation ablation. *J Am Coll Cardiol*. 2011;58:177-185

107. Mahnkopf C, Badger TJ, Burgon NS, Daccarett M, Haslam TS, Badger CT, McGann CJ, Akoum N, Kholmovski E, Macleod RS, Marrouche NF. Evaluation of the left atrial substrate in patients with lone atrial fibrillation using delayed-enhanced mri: Implications for disease progression and response to catheter ablation. *Heart Rhythm*. 2010;7:1475-1481

108. Hunter RJ, Jones DA, Boubertakh R, Malcolme-Lawes LC, Kanagaratnam P, Juli CF, Davies DW, Peters NS, Baker V, Earley MJ, Sporton S, Davies LC, Westwood M, Petersen SE, Schilling RJ. Diagnostic accuracy of cardiac magnetic resonance imaging in the detection and characterization of left atrial catheter ablation lesions: A multicenter experience. *J Cardiovasc Electrophysiol*. 2012

109. Torr GR. The acoustic radiation force. *American Journal of Physics*. 1984;52:402

110. Nightingale KR, Palmeri ML, Nightingale RW, Trahey GE. On the feasibility of remote palpation using acoustic radiation force. *J Acoust Soc Am*. 2001;110:625-634

111. Christensen D. Ultrasonic bioinstrumentation. 1988

112. Parker KJ. Ultrasonic attenuation and absorption in liver tissue. *Ultrasound Med Biol*. 1983;9:363-369

113. Baldwin SL, Marutyan KR, Yang M, Wallace KD, Holland MR, Miller JG. Measurements of the anisotropy of ultrasonic attenuation in freshly excised myocardium. *J Acoust Soc Am*. 2006;119:3130-3139

114. Palmeri ML, McAleavey SA, Fong KL, Trahey GE, Nightingale KR. Dynamic mechanical response of elastic spherical inclusions to impulsive acoustic radiation force excitation. *IEEE Trans Ultrason Ferroelectr Freq Control*. 2006;53:2065-2079

115. Palmeri ML, McAleavey SA, Trahey GE, Nightingale KR. Ultrasonic tracking of acoustic radiation force-induced displacements in homogeneous media. *IEEE Trans Ultrason Ferroelectr Freq Control*. 2006;53:1300-1313

116. Trahey GE, Palmeri ML, Bentley RC, Nightingale KR. Acoustic radiation force impulse imaging of the mechanical properties of arteries: In vivo and ex vivo results. *Ultrasound Med Biol*. 2004;30:1163-1171

117. Nightingale K. Acoustic radiation force impulse (arfi) imaging: A review. *Current medical imaging reviews*. 2011;7:328-339

118. Fahey BJ, Hsu SJ, Wolf PD, Nelson RC, Trahey GE. Liver ablation guidance with acoustic radiation force impulse imaging: Challenges and opportunities. *Phys Med Biol*. 2006;51:3785-3808

119. Fahey BJ, Nelson RC, Hsu SJ, Bradway DP, Dumont DM, Trahey GE. In vivo guidance and assessment of liver radio-frequency ablation with acoustic radiation force elastography. *Ultrasound Med Biol*. 2008;34:1590-1603

120. Nightingale K, Fahey B, Hsu S, Frinkley K, Dahl J, Palmeri M, Zhai L, Pinton G, Trahey G. On the potential for guidance of ablation therapy using acoustic radiation force impulse imaging. *I S Biomed Imaging*. 2007:1116-1119

121. Pareek G, Wilkinson ER, Bharat S, Varghese T, Laeseke PF, Lee FT, Warner TF, Zagzebski JA, Nakada SY. Elastographic measurements of in-vivo radiofrequency ablation lesions of the kidney. *J Endourol*. 2006;20:959-964

122. Fahey BJ, Nightingale KR, Stutz DL, Trahey GE. Acoustic radiation force impulse imaging of thermally- and chemically-induced lesions in soft tissues: Preliminary ex vivo results. *Ultrasound Med Biol*. 2004;30:321-328

123. Kasai C, Namekawa K, Koyano A, Omoto R. Real-time two-dimensional blood-flow imaging using an auto-correlation technique. *Ieee Transactions on Sonics and Ultrasonics*. 1985;32:458-464

124. Loupas T, Powers JT, Gill RW. An axial velocity estimator for ultrasound blood-flow imaging, based on a full evaluation of the doppler equation by means of a 2-dimensional autocorrelation approach. *IEEE Trans Ultrason Ferroelectr Freq Control*. 1995;42:672-688

125. Nightingale K, Palmeri M, Frinkley K, Sharma A, Zhai L, Trahey G. Ultrasonic imaging of the mechanical properties of tissues using localized, transient acoustic radiation force. *Int Conf Acoust Spee*. 2005:981-984

126. Nightingale K, Soo MS, Nightingale R, Bentley R, Stutz D, Palmeri M, Dahl J, Trahey G. Acoustic radiation force impulse imaging: Remote palpation of the mechanical properties of tissue. *2002 Ieee Ultrasonics Symposium Proceedings, Vols 1 and 2*. 2002:1821-1830

127. Palmeri ML, Nightingale KR. Acoustic radiation force-based elasticity imaging methods. *Interface Focus*. 2011;1:553-564

128. Yoshida N, Okamoto M, Fukuhara T. Left atrial wall motion velocity measured by the velocity profile method with tissue doppler echocardiography in normal subjects: Its relation to aging. *J Med Ultrasonics*. 2004;31:103-109

129. Yoshida N, Okamoto M, Makita Y, Nanba K. The responsibility of left atrial size and wall contraction velocity to left atrial active emptying in relation to the mitral flow velocity pattern. *Echocardiography*. 2010;27:847-853

130. Giannnantonio DM, Dumont, D.M., Trahey, G.E., Byram, B.C. Comparison of physiological motion filters for cardiac arfi. *Ultrason Imaging*. 2011;33:89-108

131. Fahey BJ, Hsu SJ, Trahey GE. A novel motion compensation algorithm for acoustic radiation force elastography. *IEEE Trans Ultrason Ferroelectr Freq Control*. 2008;55:1095-1111

132. Fahey BJ, Palmeri ML, Trahey GE. The impact of physiological motion on tissue tracking during radiation force imaging. *Ultrasound Med Biol*. 2007;33:1149-1166

133. Eyerly SA, Bahnson TD, Koontz JI, Bradway DP, Dumont DM, Trahey GE, Wolf PD. Intracardiac acoustic radiation force impulse imaging: A novel imaging method for intraprocedural evaluation of radiofrequency ablation lesions. *Heart Rhythm*. 2012;9:1855-1862

134. Council NR. Guide for the care and use of laboratory animals: Eighth edition. *The National Academies Press*. 2011

135. Dahl JJ, Pinton GF, Palmeri ML, Agrawal V, Nightingale KR, Trahey GE. A parallel tracking method for acoustic radiation force impulse imaging. *IEEE Trans Ultrason Ferroelectr Freq Control*. 2007;54:301-312

136. Giannantonio DM, Dumont DM, Trahey GE, Byram BC. Comparison of physiological motion filters for in vivo cardiac arfi. *Ultrason Imaging*. 2011;33:89-108

137. Hsu SJ, Bouchard RR, Dumont DM, Wolf PD, Trahey GE. In vivo assessment of myocardial stiffness with acoustic radiation force impulse imaging. *Ultrasound Med Biol*. 2007;33:1706-1719

138. Kundu PK. Ekman veering observed near the ocean bottom. *Journal of Physical Oceanography*. 1976;6:238-242

139. Nightingale K, Palmeri M, Trahey G. Analysis of contrast in images generated with transient acoustic radiation force. *Ultrasound Med Biol*. 2006;32:61-72

140. Nakagawa H, Yamanashi WS, Pitha JV, Arruda M, Wang X, Ohtomo K, Beckman KJ, McClelland JH, Lazzara R, Jackman WM. Comparison of in vivo tissue temperature profile and lesion geometry for radiofrequency ablation with a saline-irrigated electrode versus temperature control in a canine thigh muscle preparation. *Circulation*. 1995;91:2264-2273

141. Cao H, Vorperian VR, Tungjitkusolmun S, Tsai JZ, Haemmerich D, Choy YB, Webster JG. Flow effect on lesion formation in rf cardiac catheter ablation. *IEEE Trans Biomed Eng*. 2001;48:425-433

142. Cao H, Vorperian VR, Tsai JZ, Tungjitkusolmun S, Woo EJ, Webster JG. Temperature measurement within myocardium during in vitro rf catheter ablation. *IEEE Trans Biomed Eng*. 2000;47:1518-1524

143. Whittaker P, Zheng S, Patterson MJ, Kloner RA, Daly KE, Hartman RA. Histologic signatures of thermal injury: Applications in transmyocardial laser revascularization and radiofrequency ablation. *Lasers Surg Med*. 2000;27:305-318

144. Turek JW, Dibernardo LR, Lodge AJ, Lin SS, Davis RD, Milano CA, Simsir SA. Histopathology and transmurality of acute microwave lesions on the beating human atrium. *Interactive cardiovascular and thoracic surgery*. 2006;5:202-206

145. Nath S, DiMarco JP, Haines DE. Basic aspects of radiofrequency catheter ablation. *J Cardiovasc Electrophysiol*. 1994;5:863-876

146. Kitakaze M, Weisman HF, Marban E. Contractile dysfunction and atp depletion after transient calcium overload in perfused ferret hearts. *Circulation*. 1988;77:685-695

147. Todd GL, Baroldi G, Pieper GM, Clayton FC, Eliot RS. Experimental catecholamine-induced myocardial necrosis. Ii. Temporal development of isoproterenol-induced contraction band lesions correlated with ecg, hemodynamic and biochemical changes. *Journal of molecular and cellular cardiology*. 1985;17:647-656

148. Azuma J, Hamaguchi T, Ohta H, Takihara K, Awata N, Sawamura A, Harada H, Tanaka Y, Kishimoto S. Calcium overload-induced myocardial damage caused by isoproterenol and by adriamycin: Possible role of taurine in its prevention. *Advances in experimental medicine and biology*. 1987;217:167-179

149. Baroldi G, Mittleman RE, Parolini M, Silver MD, Fineschi V. Myocardial contraction bands. Definition, quantification and significance in forensic pathology. *International journal of legal medicine*. 2001;115:142-151

150. Nelson TR, Fowlkes JB, Abramowicz JS, Church CC. Ultrasound biosafety considerations for the practicing sonographer and sonologist. *J Ultrasound Med*. 2009;28:139-150

151. Bouchard RR, Hsu SJ, Wolf PD, Trahey GE. In vivo cardiac, acoustic-radiation-force-driven, shear wave velocimetry. *Ultrason Imaging*. 2009;31:201-213

152. Yokokawa M, Bhandari AK, Tada H, Suzuki A, Kawamura M, Ho I, Cannom DS. Comparison of the point-by-point versus catheter dragging technique for curative radiofrequency ablation of atrial fibrillation. *Pacing Clin Electrophysiol*. 2011;34:15-22

153. Rouze NC, Wang MH, Palmeri ML, Nightingale KR. Parameters affecting the resolution and accuracy of 2-d quantitative shear wave images. *IEEE Trans Ultrason Ferroelectr Freq Control*. 2012;59:1729-1740

154. Nightingale KR, Rouze NC, Wang MH, Zhai L, Palmeri ML. Comparison of qualitative and quantitative acoustic radiation force based elasticity imaging methods. *2011 8th Ieee International Symposium on Biomedical Imaging: From Nano to Macro*. 2011:1606-1609

155. Hsu SJ. Acoustic radiation force impulse imaging of myocardial stiffness. *Duke University, Biomedical Engineering PhD Dissertation*. 2009

156. Bouchard RR, Dahl JJ, Hsu SJ, Palmeri ML, Trahey GE. Image quality, tissue heating, and frame rate trade-offs in acoustic radiation force impulse imaging. *IEEE Trans Ultrason Ferroelectr Freq Control*. 2009;56:63-76

157. Dahl JJ, Dumont DM, Allen JD, Miller EM, Trahey GE. Acoustic radiation force impulse imaging for noninvasive characterization of carotid artery atherosclerotic plaques: A feasibility study. *Ultrasound Med Biol*. 2009;35:707-716

158. Nightingale K, Palmeri M, Trahey G. Analysis of contrast in images generated with transient acoustic radiation force. *Ultrasound Med Biol*. 2006;32:61-72

159. Palmeri ML, McAleavey SA, Fong KL, Trahey GE, Nightingale KR. Dynamic mechanical response of elastic spherical inclusions to impulsive acoustic radiation force excitation. *IEEE Trans Ultrason Ferroelectr Freq Control*. 2006;53:2065-2079

160. Posner KL, Sampson PD, Caplan RA, Ward RJ, Cheney FW. Measuring interrater reliability among multiple raters: An example of methods for nominal data. *Statistics in medicine*. 1990;9:1103-1115

161. Kim DT, Lai AC, Hwang C, Fan LT, Karagueuzian HS, Chen PS, Fishbein MC. The ligament of marshall: A structural analysis in human hearts with implications for atrial arrhythmias. *J Am Coll Cardiol*. 2000;36:1324-1327

162. Hwang C, Chen PS. Ligament of marshall: Why it is important for atrial fibrillation ablation. *Heart Rhythm*. 2009;6:S35-40

163. Neumann T, Vogt J, Schumacher B, Dorszewski A, Kuniss M, Neuser H, Kurzidim K, Berkowitsch A, Koller M, Heintze J, Scholz U, Wetzel U, Schneider MAE, Horstkotte D, Hamm CW, Pitschner H-F. Circumferential pulmonary vein isolation with the cryoballoon techniqueresults from a prospective 3-center study. *J Am Coll Cardiol*. 2008;52:273-278

164. Packer DL, Kowal RC, Wheelan KR, Irwin JM, Champagne J, Guerra PG, Dubuc M, Reddy V, Nelson L, Holcomb RG, Lehmann JW, Ruskin JN. Cryoballoon ablation of pulmonary veins for paroxysmal atrial fibrillationfirst results of the north american arctic front (stop af) pivotal trial. *J Am Coll Cardiol*. 2013;61:1713-1723

165. Lustgarten DL, Keane D, Ruskin J. Cryothermal ablation: Mechanism of tissue injury and current experience in the treatment of tachyarrhythmias. *Prog Cardiovasc Dis*. 1999;41:481-498

166. Dumont DM PB, Eyerly SA, Wolf PD. Feasibility of cryoablation lesion assessment using acoustic radiation force impulse imaging. *Heart Rhythm Supplement*. 2012:S353

167. Kuck KH, Reddy VY, Schmidt B, Natale A, Neuzil P, Saoudi N, Kautzner J, Herrera C, Hindricks G, Jais P, Nakagawa H, Lambert H, Shah DC. A novel

radiofrequency ablation catheter using contact force sensing: Toccata study. *Heart Rhythm*. 2012;9:18-23

168. Yokoyama K, Nakagawa H, Shah DC, Lambert H, Leo G, Aeby N, Ikeda A, Pitha JV, Sharma T, Lazzara R, Jackman WM. Novel contact force sensor incorporated in irrigated radiofrequency ablation catheter predicts lesion size and incidence of steam pop and thrombus. *Circ Arrhythm Electrophysiol*. 2008;1:354-362

169. Sy RW, Thiagalingam A, Stiles MK. Modern electrophysiology mapping techniques. *Heart, Lung and Circulation*. 2012;21:364-375

170. Kimura M, Sasaki S, Owada S, Horiuchi D, Sasaki K, Itoh T, Ishida Y, Kinjo T, Okumura KEN. Validation of accuracy of three-dimensional left atrial cartosound™ and ct image integration: Influence of respiratory phase and cardiac cycle. *J Cardiovasc Electrophysiol*. 2013:n/a-n/a

171. Eitel C, Hindricks G, Dagres N, Sommer P, Piorkowski C. Ensite velocity cardiac mapping system: A new platform for 3d mapping of cardiac arrhythmias. *Expert review of medical devices*. 2010;7:185-192

172. Wittkampf FH, Wever EF, Derksen R, Wilde AA, Ramanna H, Hauer RN, Robles de Medina EO. Localisa: New technique for real-time 3-dimensional localization of regular intracardiac electrodes. *Circulation*. 1999;99:1312-1317

173. Metz CE. Receiver operating characteristic analysis: A tool for the quantitative evaluation of observer performance and imaging systems. *Journal of the American College of Radiology : JACR*. 2006;3:413-422

Biography

Stephanie Ann Eyerly was born in St. Paul, Minnesota on May 15th, 1985. She received a Bachelor of Science in Biological Engineering from the School of Agriculture and Life Sciences jointly with the School of Engineering at Cornell University in June 2007. Eyerly received a Master of Science in Biomedical Engineering from Duke University in May 2009, and remained at Duke to conduct the presented PhD research.

Peer Reviewed Publications:

Eyerly SA, Hsu SJ, Agashe SH, Trahey GE, Li Y, Wolf PD. An in vitro assessment of acoustic radiation force impulse imaging for visualizing cardiac radiofrequency ablation lesions. *J Cardiovasc Electrophysiol*. 2010; 21:557-563

Eyerly SA, Bahnson TD, Koontz JI, Bradway DP, Dumont DM, Trahey GE, Wolf PD. Intracardiac acoustic radiation force impulse imaging: A novel imaging method for intraprocedural evaluation of radiofrequency ablation lesions. *Heart Rhythm*. 2012; 9:1855-1862

Eyerly SA, Dumont DM, Trahey GE, Wolf PD. In vitro monitoring of the dynamic elasticity changes during radiofrequency ablation with acoustic radiation force impulse imaging. *J Cardiovasc Electrophysiol*. 2013; 24:472-473